Advanced Motion Control for Electric Vehicles Using Lateral Tire Force Sensors

by

Kanghyun Nam

A dissertation submitted to the Department of Electrical Engineering
for the degree of
Doctor of Philosophy
in Electrical Engineering
at
The University of Tokyo

Supervisor:
Professor Yoichi Hori
Professor Hiroshi Fujimoto

DEPARTMENT OF ELECTRICAL ENGINEERING
THE UNIVERSITY OF TOKYO
JUNE 2012

Advanced Motion Control for Electric Vehicles Using Lateral Tire Force Sensors

For my family and friends

ACKNOWLEDGEMENTS

I would like to express my deepest gratitude to my supervisor, Professor Yoichi Hori, for his invaluable support, supervision, and suggestions throughout my Ph.D. course. His practical insights in the motion control as well as his profound knowledge on control theory have provided me continuous motivation to successfully complete my dissertation. Among many things that I have learned from him, I have recognized that intimate personal relationships and collaboration with teammates are indispensable to be a good researcher or professor. I would also like to express my gratitude to Professor Hiroshi Fujimoto for helping and supporting my research through invaluable comments.

I would like to sincerely thank Professor Hiroyuki Ohsaki, Professor Katsushi Ikeuchi, Professor Takafumi Koseki, and Professor Takashi Kubota for their careful reading and suggestions on improving the dissertation.

I am also truly thankful to my Master's supervisor, Professor Seibum B. Choi. For two years with him in KAIST, I have learned vehicle dynamics and his insightful advice and deep knowledge on vehicle control have continuously stimulated my interests in vehicle control engineering.

I appreciate all the members of Hori/Fujimoto laboratory: Dr. Imura, Dr. Alexander, Engineer Uchida, Yafei, Kato, Zhu, Miyajima, Huang, Binh Minh, Aoki, Amada, Marcus, Ochi, Koh, Paopao, Sonokawa, Tsuboka, Tokuyama, Koji, Maeda, Ishibashi, Kanematsu, Takei, Tanikawa, Harada, Higashino, Yone, Watanabe, Ohnishi, Kobayashi, Takahashi, Nakamura, Miura, and all of you reading this dissertation. I would also like to special thank Dr. Sehoon, Yunha, and Kayoung for their inspiring discussions and warm-hearted friendship.

Also, I cannot forget my friends in Automotive Control Laboratory, KAIST. I would especially like to thank Kwanghyun, Jinsung, Hyomin for their warm friendship. I am truly thankful to my friends in Korea as well.

Lastly, I would like to thank my parents, Byungkyu Nam and Hwaja Shin, my sister, Jungim Nam, and my trustworthy brother, Chulhyun Nam, for their unlimited dedication and support.

TABLE OF CONTENTS

LIST OF FIGURES

Figure

LIST OF TABLES

Table

LIST OF ABBREVIATIONS

2-DOF two degree-of-freedom

CG center of gravity

DOB disturbance observer

EKF extended Kalman filter

EPS electric power steering

IWM-EV in-wheel-motor-driven electric vehicles

KF Kalman filter

LTFC lateral tire force control

MSHub multi-sensing hub

RLS recursive least square

SbW steer-by-wire

ABSTRACT

Advanced Motion Control for Electric Vehicles Using Lateral Tire Force Sensors

by

Kanghyun Nam

Supervisor: Prof. Yoichi Hori and Prof. Hiroshi Fujimoto

The principal concern in motion control of electric vehicles is providing drivers with more enhanced safety by preventing risky driving situations. A close examination of accident data reveals that loss of the vehicle control is the main reason for most vehicle accidents. To help to prevent such accidents, vehicle motion control systems should be used, which require important information on vehicle state and tire-road conditions. Unfortunately, some critical parameters in vehicle motion control such as vehicle sideslip angle, roll angle, and tire-road friction coefficient are difficult to measure in a vehicle, due to both technical and economic reasons. Recently, automotive companies have looked at utilizing tire forces which are directly measured by lateral tire force sensors, e.g., MSHub unit invented by NSK Ltd. Since the vehicle motion is governed by tire forces generated by tire-road interaction, this tire force information can provide promising solutions for accurate state estimation and advanced motion control. In this thesis, several advanced methods for robustly estimating the vehicle state and controlling the vehicle motion are proposed based on lateral tire force sensors. These advanced methods include 1) novel algorithms for vehicle sideslip angle and roll angle estimation, 2) real-time algorithm to estimate tire-road condition, 3) advanced motion control algorithm based on vehicle sideslip angle estimation, 4) advanced motion control algorithm based on direct tire force control for vehicle safety enhancement.

Robust estimation of vehicle states such as vehicle sideslip angle and roll angle is a challenging issue in vehicle motion control applications like yaw stability control and roll stability control. In this thesis, novel methods for estimating vehicle sideslip angle and roll angle are proposed using lateral tire force sensors. For vehicle sideslip angle estimation, two estimation algorithms based on a recursive least square (RLS) approach and an extended Kalman filter (EKF) technique are designed, respectively. For roll angle estimation, KF is designed using available sensor measurements and physical roll dynamics model. The effectiveness of proposed estimation methods is verified through field tests on an experimental electric vehicle. Experimental results demonstrate that the proposed estimation methods can accurately estimate the vehicle sideslip angle and roll angle.

The robust design of motion controllers for vehicle stability enhancement is challenging due to nonlinear characteristics in vehicle and tire models, e.g., varying tire cornering stiffness with respect to road condition and tire force saturation. In this thesis, the two motion control algorithms are designed based on lateral tire force sensor application; 1) a motion control algorithm, based on vehicle sideslip angle estimation, is designed using two-degree-of-freedom (2-DOF) control methodology for yaw rate and vehicle sideslip tracking control and an adaptive feed-forward control technique is applied for improving control performances, 2) a novel motion control algorithm based on direct tire force control is designed. In this control algorithm, the real-time estimation of a critical vehicle state, i.e., a vehicle sideslip angle, is not required anymore. A robust control approach is applied in the design of the controllers for improved robustness to uncertainties in the vehicle and tire models. Moreover, a DOB is utilized to compensate for changes in the dynamic tire model as well as for mechanical disturbances in the actuators. Both control algorithms are implemented on an experimental electric vehicle with in-wheel motors and those control performances, e.g., yaw rate, vehicle sideslip angle tracking, and lateral tire force tracking ability, are verified through field tests. It is shown that proposed control algorithms based on lateral tire force sensors can contribute to improvement of the vehicle stability.

This thesis proposes novel vehicle state estimation and motion control methods using lateral tire force sensors, and has discussed the practical application of lateral tire force sensors to motion control systems for future electric vehicles. Moreover, this thesis investigates important

technologies for improving the motion control systems of electric vehicles not only based on theoretical approaches to vehicle, tire dynamics and estimation, and control design, but also implementation on experimental electric vehicles in real-time.

CHAPTER I

Introduction

1.1 Research Motivation

1.1.1 Vehicle Safety

World wide, an estimated 1.2 million people are killed in road crashes each year and as many as 50 million are injured. Over the past decades, active safety control systems have been developed to enhance handling and passenger safety.

"There are more than 1,700 fatalities and 840,000 injuries yearly due to vehicle crashes off public highways."

reported by U.S.A National Highway Traffic Safety Administration (NHTSA)

Both public agency and automotive manufacturers have shown sustained interests in active safety technologies which are unquestionably life saving technologies. A variety of active safety control systems including anti-lock braking system (ABS), traction control system (TCS), electronic stability control (ESC) system, and active front steering (AFS) system have already been commercialized and new safety control functions are added so as to substantially enhance vehicle safety, convenience, and driver comfort. The NHTSA mandated the installation of ESC as standard equipment for all new light vehicles in the US by 2012 (*Forkenbrock et al.*, 2005). Moreover, As part of a comprehensive plan for reducing the serious risk of rollover crashes and the risk of death and serious injury in various crashes shown in Figure 1.2, new Federal Motor Vehicle Safety Standard (FMVSS) No. 126 is established to require ESC systems on passenger cars,

Figure 1.1: Several types of vehicle crash during driving (http://www.car-accidents.com/)

multipurpose passenger vehicles, trucks, and buses with a gross vehicle weight rating of 4,536 Kg (10,000 pounds) or less. ESC systems use automatic computer-controlled braking of individual wheels to assist the driver in maintaining control in critical driving situations. NHTSA estimates ESC will reduce single-vehicle crashes of passenger cars by 34% and single vehicle crashes of sport utility vehicles (SUVs) by 59%, with a much greater reduction of rollover crashes. NHTSA estimates ESC would save 5,300 to 9,600 lives and prevent 156,000 to 238,000 injuries in all types of crashes annually once all light vehicles on the road are equipped with ESC which reported in *NHTSA* (2012).

Motivated by these necessities of active safety systems for engine vehicles as well as electric vehicles, many researcher have studied on new safety control systems for applications to electric vehicles (*Chan*, 1993; *Hori et al.*, 1998; *Sakai et al.*, 1999; *Abe et al.*, 2001; *Chan*, 2002; *Hori*, 2004; *Mutoh et al.*, 2007; *Yin et al.*, 2009; *Hu et al.*, 2012). In addition, for enhancing vehicle handling and increasing passenger safety, more accurate and robust methods for predicting vehicle states and controlling vehicle motion have been proposed (*Tahami et al.*, 2003; *Yih and Gerdes*, 2005;

Hsu et al., 2010; *Fujimoto and Yamauchi*, 2010; *Ando and Fujimoto*, 2010; *Nam et al.*, 2012a,b).

1.1.2 Electric Vehicles

As concerns over air pollution and global warming continue to mount, the electric vehicle market is predicted to expand at a significantly rapid rate. Pike Research anticipates that the annual market for electric vehicles will grow to 2.9 million vehicles by 2017 (*Pike-research*, 2010). Increasing fuel costs, government purchase incentives, increasing fuel economy standards, and increased vehicle availability will benefit several types of electric vehicles (e.g., hybrid electric vehicles, battery electric vehicle, etc.) to varying degrees. In reality, electric vehicles are considered as a promising technology for drastically reducing the environmental burden of road transport. More than a decade ago and also more recently, they were advocated by many governments and automotive manufacturers as an important element in reducing CO_2 emissions of particularly passenger cars and light commercial vehicles as well as emissions of pollutants and noise. Over the recent years, almost all of automotive manufacturers in the worlds have released electric vehicles, shown in Figure 1.2, for even great reductions in CO_2 emissions that contribute to global climate change. For examples,

- "Honda unveiled the 2013 Fit EV at the 2011 Los Angeles Auto Show and announced plans to begin leasing the 123 city-mile per charge (76 mile range combined adjusted city/highway)1 battery-electric commuter vehicle to its U.S. customers in the summer of 2012," (*HONDA*, 2012)

- "General Motors, maker of the Chevy Volt plug-in hybrid, will sell a small totally electric car beginning in 2013, and The Chevy Spark EV will be sold in limited markets in the U.S. and other countries," (*CNNMoney*, 2012)

- "Released in Japan in July 2009: the Mitsubishi i-MiEV, which stands for Mitsubishi innovative Electric Vehicle, is one of the world's first truly viable zero drive-time emission city commuters in volume production." (*NEXTCAR*, 2011)

Motivated by these technical trends of electric vehicles, a great deal of research on electric vehicles has been worked. In particular, research on driving motors, motion control, and battery

(a) i-MiEV: Mitsubishi Motors

(b) Leaf: Nissan

(c) Volt: General Motors

(d) COMS: Toyota AotoBody

Figure 1.2: Electric vehicles of automotive manufacturers.

has been intensively carried out in recent years (*Chan*, 1993; *Hori et al.*, 1998; *Chan*, 2002; *Hori*, 2004; *Fujimoto et al.*, 2005; *Mutoh et al.*, 2007; *Yin et al.*, 2009; *Wang et al.*, 2011; *Hu et al.*, 2012; *Wang and Wang*, 2012).

1.1.3 Development of Tire-Force Sensing Technology

As the vehicle motion is governed by the forces generated between the tire and the road, knowledge of individual tire forces in each direction, i.e., longitudinal, lateral, and vertical directions, is crucial when predicting and controlling vehicle motion. Moreover, these would also offer motion control systems with the most information for maximizing the vehicle's handling capability and enhancing vehicle stability in all driving situations. For example, a vehicle can turn because of the generated lateral tire forces. In fact, what happens is that when the front wheels are steered by a driver, a tire slip angle is created, which gives rise to lateral tire forces. This lateral tire force makes vehicle's lateral motion. Vehicle motion control systems currently avail-

Table 1.1: Tire force sensors.

RoaDyn® Wheel Force Transducer	**Multi-Axis Wheel Force Transducer**	**WFS (Wheel Force Sensor)**
	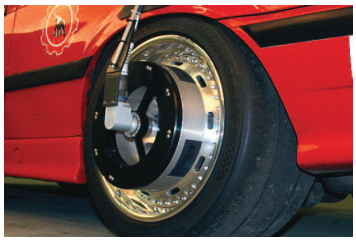	
Kistler (Swiss)	PCB Load & Torque, Inc. (USA)	A&D Company, Limited (JAPAN)
http://www.pcbloadtorque.com/	http://www.kistler.com	http://www.aandd.jp
over 40000$		

able on production vehicles rely on available inexpensive sensor measurements like accelerometer and gyro sensors. In reality, lateral tire force measurements using sensors is very difficult for economic reasons.

As shown in Table 1.1, tire force sensors cost over $40000. From this reason, several studies have been conducted regarding the estimation of lateral tire forces (*Dakhlallah et al.*, 2008; *Kim*, 2009; *Cho et al.*, 2010; *Doumiati et al.*, 2009, 2010, 2011). In recent literature *Doumiati et al.* (2011), two nonlinear observers, which are an EKF and unscented KF, were developed for estimating individual lateral tire forces and those effectiveness was demonstrated through a comparison with real experimental data. However, there still exist challenging problems with nonlinear observers, e.g., computational complexity, sensitivity against the road conditions, and time-varying parameters in nonlinear tire models.

To overcome technical difficulties in estimation, Japanese company, NSK Ltd., has developed lateral tire force sensors (called MSHub unit) based on novel sensing technologies. Figure 1.3 illustrates a MSHub unit. The sensing principle is as follows: the revolution speeds of rolling elements in a pair of rows are sensed by a pair of revolution speed sensors and difference of those sensed revolution speeds is used to calculate the radial or axial loads (*Koichiro Ono*, 2009). It is anticipated that vehicle motion control systems would greatly benefit from practical use of cost-effective lateral tire force sensors (i.e., MSHub unit). This motivates the development of

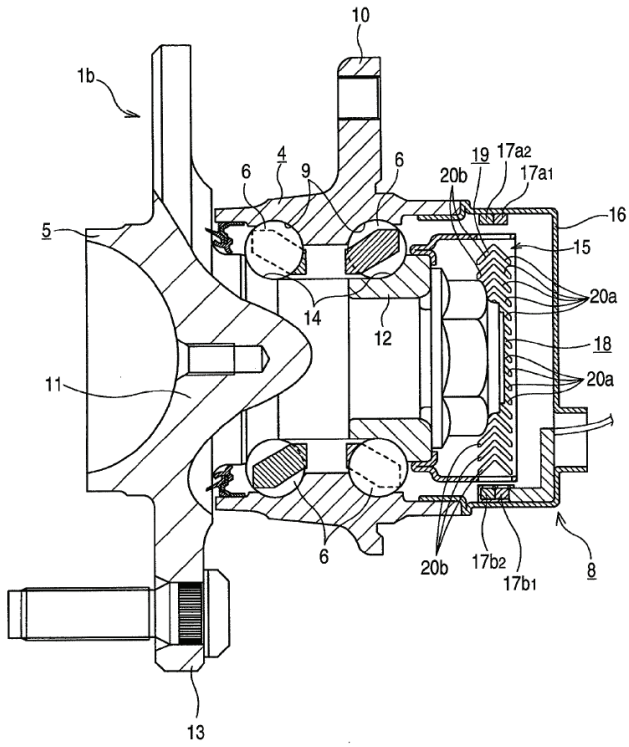

Figure 1.3: Sectional drawing of lateral tire force sensor of NSK Ltd. (MSHub unit (*Koichiro Ono*, 2009)).

robust real-time algorithms for estimating the vehicle states and controlling the vehicle motion.

1.2 Overview of Motion Control Systems of Electric Vehicles

Over the past few decades, various kinds of vehicle motion control systems have been developed to enhance vehicle handling and passenger safety. These systems are aimed at preventing unintended vehicle behavior through active vehicle control and assist drivers in maintaining control of the vehicles. Due to the increasing concerns about advanced motion control of electric vehicles with in-wheel motors, a great deal of research on dynamics control for electric vehicles has been carried out (*Hori*, 2004; *Mutoh et al.*, 2007; *Yin et al.*, 2009; *Wang et al.*, 2011). Advanced motion control systems for electric vehicles, slip prevention, spinout prevention, and excessive roll prevention, are referred to as yaw stability control and roll stability control, respectively. Compared with internal combustion engine vehicles, electric vehicles with in-wheel motors have several advantages in the viewpoint of motion control (*Hori*, 2004).

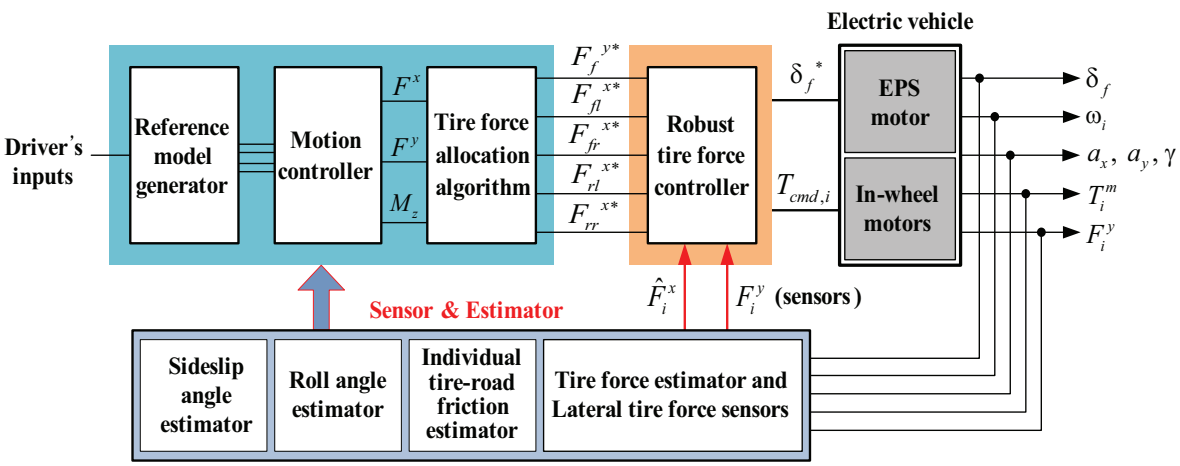

Figure 1.4: Overall vehicle motion control scheme of future personal electric vehicles.

1. The torque generation of driving motors is very fast and accurate.

2. The driving torque can be easily measured from motor current.

3. Each wheel with an in-wheel motor can be independently controlled.

As aforementioned, torque output of the motor can be easily measured from the motor current. This merit makes it easy to estimate driving force or braking forces between tire and road surface in real time, which contributes a great deal to application of new control strategies based on road condition estimation (*Yin et al.*, 2009).

Figure 1.4 illustrates overall vehicle motion control scheme for electric vehicles. This thesis presents new motion control scheme based on lateral tire force sensor applications. The motion control scheme in Figure 1.4 consists of following parts: 1) reference model generator; 2) upper-level controller, i.e., motion controller; 3) tire force allocation algorithm; 4) robust tire force controller; 5) sensor and estimation parts.

1.3 Thesis Outline

This thesis addresses new approaches to vehicle state estimation and motion control using lateral tire force sensors. Several estimation methods and motion control schemes are presented. Thesis outline shown in Fig. 1.5 is as follows.

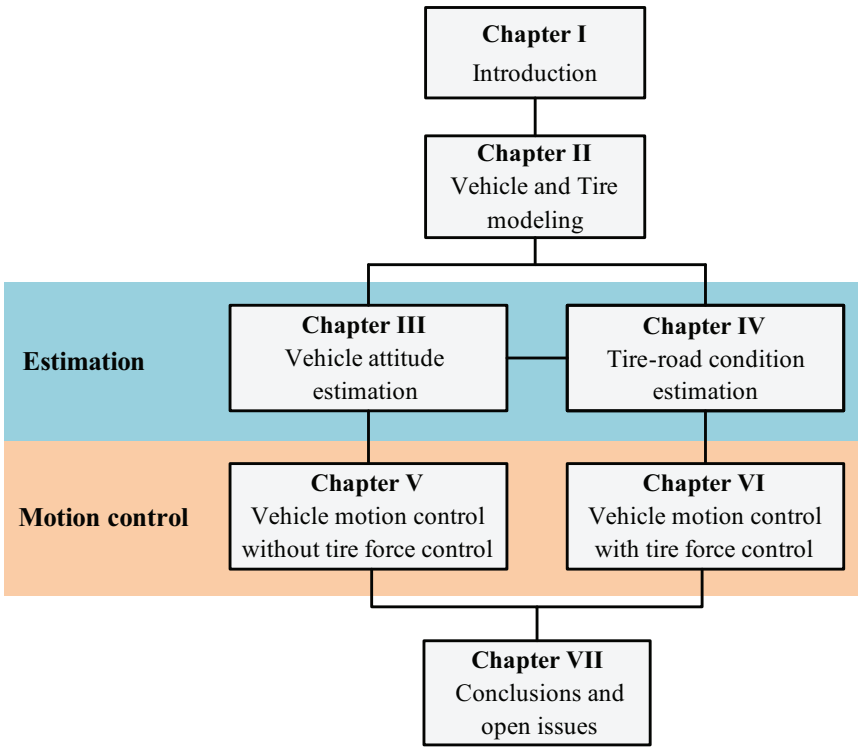

Figure 1.5: Thesis Outline.

[Chapter II: Vehicle and Tire Modeling]

Modeling of the target vehicle and tires is a primary step for the development of state observers and control design. Full vehicle and single track vehicle models, which are widely used in vehicle control design, are presented. Tires that generate forces and moments have significant effects on the vehicle dynamics properties. Thus, tire modeling describing the phenomenon of tire-road interaction is an important step in ground vehicle modeling. Several existing tire models are introduced and practical applications in this thesis are discussed.

[Chapter III: Vehicle Attitude Estimation Using Lateral Tire Force Sensors]

In this chapter, novel methods for estimating the vehicle sideslip and roll angles are presented. Performances of the existing estimation methods are challenged by nonlinearities in vehicle and tire parameters, e.g., tire cornering stiffness, vehicle speed, and weight transfer effects etc.. Lat-

eral tire force sensors which were recently invented by NSK Ltd. are used and feasibility of the practical applications to vehicle control systems is discussed. The proposed estimation algorithms including RLS algorithm and extended Kalman filter provide improved estimation accuracy.

[Chapter IV: Tire-Road Condition Estimation]

Real time information on vehicle states and tire-road conditions contributes to performance enhancement of vehicle control system. An estimation algorithm of instantaneous lateral tire force limit is developed based on vertical tire force estimation and lateral tire force measurements. The accurate and real time estimation of tire-road conditions is very useful to avoid tire force saturation during cornering operation. A RLS algorithm is used to identify the tire parameters and implemented on an experimental electric vehicle.

[Chapter V: Advanced Motion Control Based on Robust Sideslip Angle Estimation (without Tire Force Control)]

The objective of the vehicle motion control is to improve the vehicle steadiness and transient response properties, enhancing vehicle handling performance and maintaining stability in those cornering maneuvers, i.e., the yaw rate or sideslip angle of the vehicle should be close to desired vehicle responses. Advanced motion control scheme based on adaptive feed-forward control, which is realized through tire cornering stiffness estimation in real time, is presented. In conventional one degree-of-freedom controllers (e.g., PID controller), the only problem of the fixed robust controller is that the control performance of closed-loop system becomes too conservative when the parameter variation in the vehicle model is too large. For this reason, adaptive feed-forward controller is designed to improve the tracking performance. Computer simulation and field tests are performed to verify the effectiveness of proposed motion control system.

[Chapter VI: Advanced Motion Control Based on Lateral Tire Force Control]

In this chapter, a advanced motion control method based on robust lateral tire force control (LTFC) is proposed to improve vehicle stability or maneuverability. During cornering, vehicle motion is totally governed by lateral forces acting on tires. Thus, the real-time infor-

mation on tire forces provides advantages in vehicle motion control. Since the lateral tire force measurements are available by using MSHub units which were invented by NSK Ltd, the direct lateral tire force control is realizable via active front steering. In control design, a robust control method, e.g., 2-DOF with a DOB, is used for improving the reference tracking performance. Moreover, the stability of the proposed control system is discussed by using small gain theorem. The proposed motion controller is implemented on an experimental in-wheel-motor-driven electric vehicles (IWM-EV) and its performance and effectiveness are verified by field tests. Finally, practical applications of lateral tire force sensors to vehicle motion control systems are discussed.

[**Chapter VIII: Conclusions and Open Issues**]

Conclusions drawn from this work and the remaining open issues are discussed in this chapter.

[**Appendix: Robust Yaw Stability Control Based on Longitudinal Tire Force Control**]

Yaw stability control systems that prevent vehicles from spinning and drifting out have been developed and recently commercialized by automotive manufacturers. This chapter has presented robust yaw stability control method based on nonlinear motion control approach, i.e., sliding mode control. The proposed controller is implemented on IWM-EV for stability enhancement. The proposed control structure is composed of a reference generator, a feedback controller (e.g., sliding mode controller), and parameter adaptation laws. The sliding mode control method, that is capable of guaranteeing robust stability in the presence of model uncertainties and disturbances, is used to stabilize the vehicle yaw motion. Field tests using an experimental electric vehicle are carried out and its effectiveness is discussed.

CHAPTER II

Vehicle and Tire Modeling

2.1 Introduction

This chapter explains fundamental vehicle dynamics by introducing vehicle models and tire models, which have been widely adopted for vehicle motion control. This helps to get a basic idea of what parameters and states of a vehicle are important in vehicle motion control. In general, vehicle system modeling is divided in two areas: (1) vehicle chassis modeling and (2) tire modeling. Two vehicle models describing the planar motion of the vehicles are introduced and several tire models are described.

2.2 Vehicle Modeling

In order to model the motion of a vehicle, it is useful to use the body-fixed coordinate system with the origin at the vehicle center of gravity (CG) for a general rotating rigid body. The relationship between acceleration in body-fixed coordinates and acceleration in inertial coordinates can be used to obtain inertial acceleration along the lateral axis of a vehicle which has rotational yaw motion (*Rajamani*, 2011). Figure 2.1 described two coordinate systems: a coordinate system fixed in inertial space (**XYZ**) and a coordinate system fixed to the body (**xyz**).

Let consider a particle **P** with inertial coordinates $[\mathbf{X}\ \mathbf{Y}\ \mathbf{Z}]^T$ and body-fixed coordinates $[\mathbf{x}\ \mathbf{y}\ \mathbf{z}]^T$ located on the body. Let $\vec{\mathbf{r}}$ be the vector from the origin of the inertial coordinate system to the point **P**. The particle acceleration in inertial coordinates can be related to its

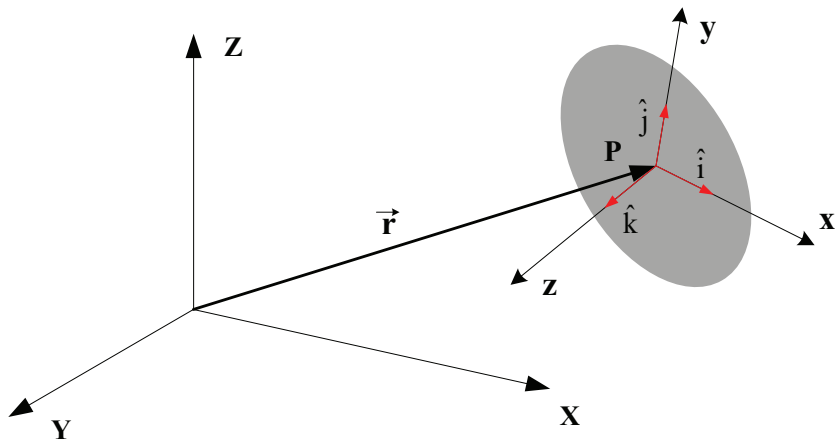

Figure 2.1: Inertial and body-fixed coordinate systems for particle **P**.

acceleration in body-fixed coordinates as follows (*Rajamani*, 2011)

$$\frac{d^2}{dt^2}\begin{Bmatrix} \mathbf{X} \\ \mathbf{Y} \\ \mathbf{Z} \end{Bmatrix} = \frac{d^2}{dt^2}\begin{Bmatrix} \mathbf{x} \\ \mathbf{y} \\ \mathbf{z} \end{Bmatrix} + \vec{\mathbf{\Omega}} \times (\vec{\mathbf{\Omega}} \times \vec{\mathbf{r}}) + \dot{\vec{\mathbf{\Omega}}} \times \vec{\mathbf{r}} + 2\vec{\mathbf{\Omega}} \times \dot{\vec{\mathbf{r}}} \tag{2.1}$$

All the vectors on the right-hand side of the above equation are expressed in body-fixed coordinates. By applying (2.1) to the case of lateral vehicle system shown in Figure 2.2, we can have following relationship,

$$\vec{\mathbf{\Omega}} = \dot{\mathbf{\Psi}}\hat{k} \tag{2.2}$$

$$\vec{\mathbf{r}} = -\mathbf{R}\hat{j} \tag{2.3}$$

where $\vec{\mathbf{\Omega}}$ is the angular speed of body, $\mathbf{\Psi}$ is the yaw angle of a vehicle in global axes, $\mathbf{R}$ is the turn radius of a vehicle or radius of road, and $\hat{i}$, $\hat{j}$, and $\hat{k}$ are unit vectors in the direction of the $\mathbf{x}$, $\mathbf{y}$, $\mathbf{z}$ axes.

From (2.1), the inertial acceleration is obtained as

$$\vec{a}_{\text{inertial}} = \vec{\mathbf{\Omega}} \times (\vec{\mathbf{\Omega}} \times \vec{\mathbf{r}}) + \dot{\vec{\mathbf{\Omega}}} \times \vec{\mathbf{r}} + 2\vec{\mathbf{\Omega}} \times \dot{\vec{\mathbf{r}}} + \vec{a}_{\text{body-fixed}} \tag{2.4}$$

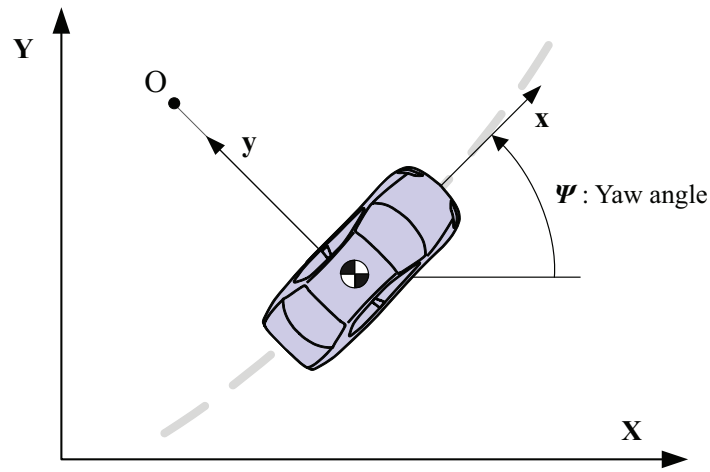

Figure 2.2: Rotating coordinate for lateral vehicle motion.

or

$$\overrightarrow{a}_{\text{inertial}} = \dot{\mathbf{\Psi}}\hat{k}\mathbf{x}(\dot{\mathbf{\Psi}}\hat{k}\mathbf{x} - \mathbf{R}\hat{j}) + \ddot{\mathbf{\Psi}}\hat{k}\mathbf{x} - \mathbf{R}\hat{j} + 2\dot{\mathbf{\Psi}}\hat{k}\mathbf{x} - \dot{\mathbf{R}}\hat{j} + \ddot{\mathbf{x}}\hat{i} + \ddot{\mathbf{y}}\hat{j} \tag{2.5}$$

$$= \dot{\mathbf{\Psi}}^2\mathbf{R}\hat{j} + (\mathbf{R}\ddot{\mathbf{\Psi}} + 2\dot{\mathbf{\Psi}}\dot{\mathbf{R}})\hat{i} + \ddot{\mathbf{x}}\hat{i} + \ddot{\mathbf{y}}\hat{j} \tag{2.6}$$

$$= (\ddot{\mathbf{x}} + \mathbf{R}\ddot{\mathbf{\Psi}} + 2\dot{\mathbf{\Psi}}\dot{\mathbf{R}})\hat{i} + (\ddot{\mathbf{y}} + \dot{\mathbf{\Psi}}^2\mathbf{R})\hat{j} \tag{2.7}$$

Hence the inertial acceleration along the y axis is

$$a_x = \ddot{\mathbf{x}} + \mathbf{R}\ddot{\mathbf{\Psi}} + 2\dot{\mathbf{\Psi}}\dot{\mathbf{R}} \tag{2.8}$$

$$a_y = \ddot{\mathbf{y}} + \dot{\mathbf{\Psi}}^2\mathbf{R} = \ddot{\mathbf{y}} + \dot{\mathbf{\Psi}}v_x = \dot{v}_y + \gamma v_x \tag{2.9}$$

In addition, according to Figure 2.3, the kinematic relationships among the vehicle velocity, yaw rate, and acceleration can also be expressed as follows:

$$a_x = \dot{v}_x - \gamma v_y \tag{2.10}$$

$$a_y = \dot{v}_y + \gamma v_x \tag{2.11}$$

where a_x and a_y are the longitudinal and lateral accelerations of the vehicle CG, v_x and v_y are the longitudinal and lateral vehicle velocities, and γ is the yaw rate.

Figure 2.3 shows a schematic diagram of three DOF vehicle model for describing longitudinal

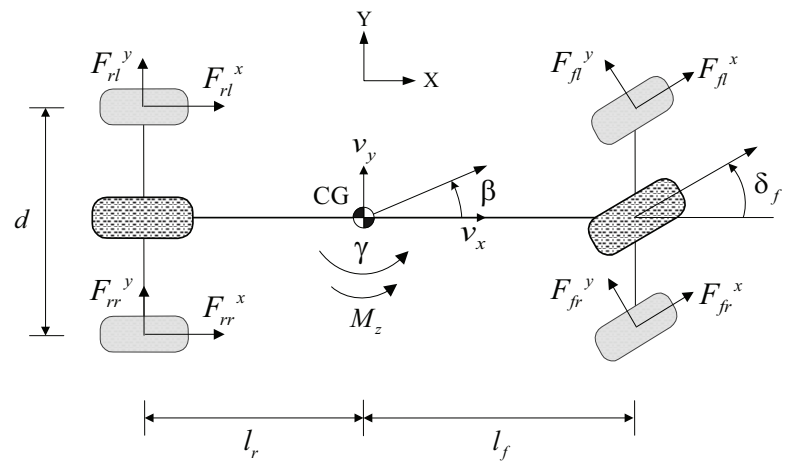

Figure 2.3: Schematic diagram of three DOF vehicle model.

motion, lateral motion motion, and yaw motion. A body-fixed coordinate system with the origin at CG is used to build the vehicle model. The equations of motions governing longitudinal, lateral dynamics, and yaw dynamics are given by

$$ma_x = m(\dot{v}_x - \gamma v_y) = \sum F^x = (F_{fl}^x + F_{fr}^x)\cos\delta_f + F_{rl}^x + F_{rr}^x - (F_{fl}^y + F_{fr}^y)\sin\delta_f \tag{2.12}$$

$$ma_y = m(\dot{v}_y + \gamma v_x) = \sum F^y = (F_{fl}^x + F_{fr}^x)\sin\delta_f + (F_{fl}^y + F_{fr}^y)\cos\delta_f + (F_{rl}^y + F_{rr}^y) \tag{2.13}$$

$$I_z\dot{\gamma} = l_f(F_{fl}^x + F_{fr}^x)\sin\delta_f + l_f(F_{fl}^y + F_{fr}^y)\cos\delta_f - l_r(F_{rl}^y + F_{rr}^y) + M_z \tag{2.14}$$

where m denotes the total mass of the vehicle, l_f and l_r are the distances from the vehicle CG to the front and rear axles, I_z is the yaw moment of inertia, δ_f is the front steering angle. F_i^x and F_i^y are the longitudinal and lateral tire forces of the ith wheel, i is fl, fr, rl, and rr, and represents the front left, front right, rear left, and rear right wheels, respectively. M_z is the yaw moment and is expressed as

$$M_z = \frac{d}{2}(F_{rr}^x - F_{rl}^x) + \frac{d}{2}(F_{fr}^x - F_{fl}^x)\cos\delta_f. \tag{2.15}$$

where d is the track width, the main difference with commonly used vehicle dynamics model is that the yaw moment M_z can be an additional input variable, which is generated by motor torque difference between each wheel (*Nam et al.*, 2012a).

Longitudinal and lateral tire slips are the results of the tire-road interaction. The vehicle

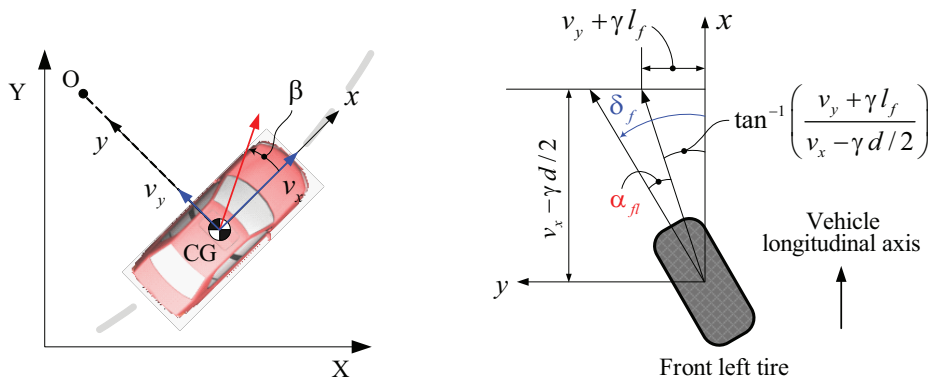

(a) Vehicle sideslip angle.

(b) Calculation of the front left tire slip angle.

Figure 2.4: Vehicle sideslip angle and tire slip angle.

sideslip angle β, shown in Figure 2.4(a), is defined as the angle between the longitudinal axis of the vehicle and the orientation of vehicle velocity vector,

$$\beta = \tan^{-1}\left(\frac{v_y}{v_x}\right) \tag{2.16}$$

The individual tire slip angles are calculated based on geometric derivation using wheel velocity vectors. If the velocities at wheel ground contact points are known, the tire slip angles can be easily derived geometrically and are given by

$$\alpha_{fl} = -\delta_f + \tan^{-1}\left(\frac{v_y + \gamma l_f}{v_x - \gamma d/2}\right) \tag{2.17a}$$

$$\alpha_{fr} = -\delta_f + \tan^{-1}\left(\frac{v_y + \gamma l_f}{v_x + \gamma d/2}\right) \tag{2.17b}$$

$$\alpha_{rl} = \tan^{-1}\left(\frac{v_y - \gamma l_r}{v_x - \gamma d/2}\right) \tag{2.17c}$$

$$\alpha_{rr} = \tan^{-1}\left(\frac{v_y - \gamma l_r}{v_x + \gamma d/2}\right) \tag{2.17d}$$

where α_i is the tire slip angle at individual tires. Figure 2.4(b) illustrates the calculation of the tire slip angle for front left tire.

Longitudinal wheel slip λ_i for individual tires is defined as

$$\lambda_i = 1 - \frac{r_\omega \omega_i}{v_{x,i}}, \qquad \text{if } v_{x,i} > r_\omega \omega_i \qquad \text{:Deceleration} \tag{2.18}$$

$$\lambda_i \;=\; -1 + \frac{v_{x,i}}{r_\omega \omega_i}, \qquad \text{if} \;\; v_{x,i} < r_\omega \omega_i \qquad \text{:Acceleration} \tag{2.19}$$

where r_ω is the wheel radius, ω_i is the angular velocity of each wheel, and $v_{x,i}$ is the velocity of the wheel ground contact point and is given by

$$v_{x,fl} \;=\; \left(v_x - \frac{\gamma d}{2}\right)\cos\delta_f + (v_y + \gamma l_f)\sin\delta_f \tag{2.20a}$$

$$v_{x,fr} \;=\; \left(v_x + \frac{\gamma d}{2}\right)\cos\delta_f + (v_y + \gamma l_f)\sin\delta_f \tag{2.20b}$$

$$v_{x,rl} \;=\; \left(v_x - \frac{\gamma d}{2}\right)\cos\delta_r + (v_y - \gamma l_r)\sin\delta_r \tag{2.20c}$$

$$v_{x,rr} \;=\; \left(v_x + \frac{\gamma d}{2}\right)\cos\delta_r + (v_y - \gamma l_r)\sin\delta_r \tag{2.20d}$$

where a vehicle with front wheel steering is considered, thus, it is assumed $\delta_r = 0$.

Based on wheel rotational motion illustrated in Figure 2.5, the rotational wheel dynamics is described by

$$I_\omega \dot{\omega}_i \;=\; T_i^m - T_i^b - r_\omega F_i^x \tag{2.21}$$

where I_ω is the spin inertia of the wheel, T^m and T^b are the motor torque and brake torque acting on individual wheels, respectively. It is noted that torques of in-wheel motors and each wheel's angular velocity are directly obtained from motor currents and resolvers. On the other hand, the brake torque applying on each wheel is estimated from the measured brake pressure.

For the sake of simplicity, the singe track vehicle model, illustrated in Figure 2.6, is widely

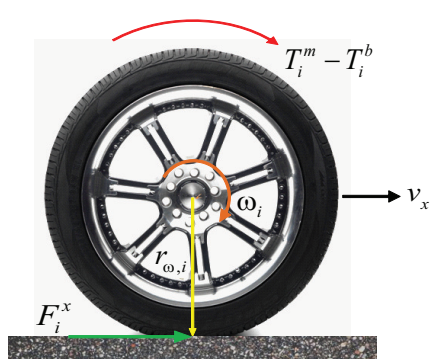

Figure 2.5: Wheel rotational motion.

used. It is also known as the bicycle model, which is obtained by approximating the front and rear pairs of wheels as single wheels and linearizing the equation. From the single track vehicle model, shown in Figure 2.6, (2.13)–(2.14) are simplified as

$$ma_x = m(\dot{v}_x - \gamma v_y) = F_f^x \cos\delta_f + F_r^x - F_f^y \sin\delta_f \tag{2.22}$$

$$ma_y = mv_x(\dot{\beta} + \gamma) = F_f^x \sin\delta_f + F_r^y + F_f^y \cos\delta_f \tag{2.23}$$

$$I_z\dot{\gamma} = l_f F_f^x \sin\delta_f + l_f F_f^y \cos\delta_f - l_r F_r^y + M_z \tag{2.24}$$

where the front longitudinal tire force F_f^x is the sum of the front left and right longitudinal tire forces (i.e., $F_f^x = F_{fl}^x + F_{fr}^x$), rear longitudinal tire force F_r^x is the sum of the rear left and right longitudinal tire forces (i.e., $F_r^x = F_{rl}^x + F_{rr}^x$), front lateral tire force F_f^y is the sum of the front left and right lateral tire forces (i.e., $F_f^y = F_{fl}^y + F_{fr}^y$), and the rear lateral tire force F_r^y is the sum of the rear left and right lateral tire forces (i.e., $F_r^y = F_{rl}^y + F_{rr}^y$).

The definition of the front and rear tire slip angles α_f and α_r, which are illustrated in Figure 2.6, can be taken from Figure 2.7.

$$\alpha_f = \beta + \frac{\gamma l_f}{v_x} - \delta_f \tag{2.25}$$

$$\alpha_r = \beta - \frac{\gamma l_r}{v_x} \tag{2.26}$$

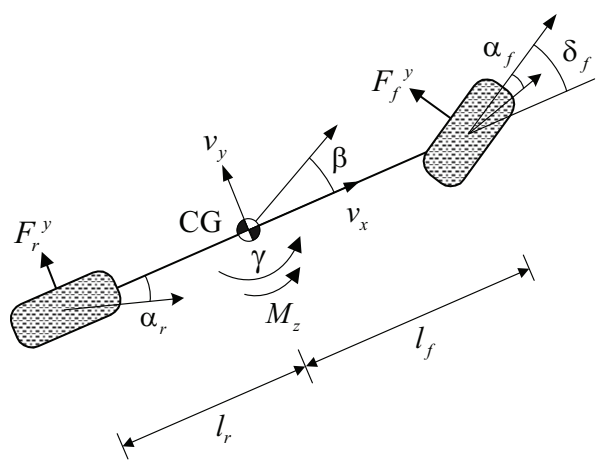

Figure 2.6: Single track vehicle model (i.e., Bicycle model).

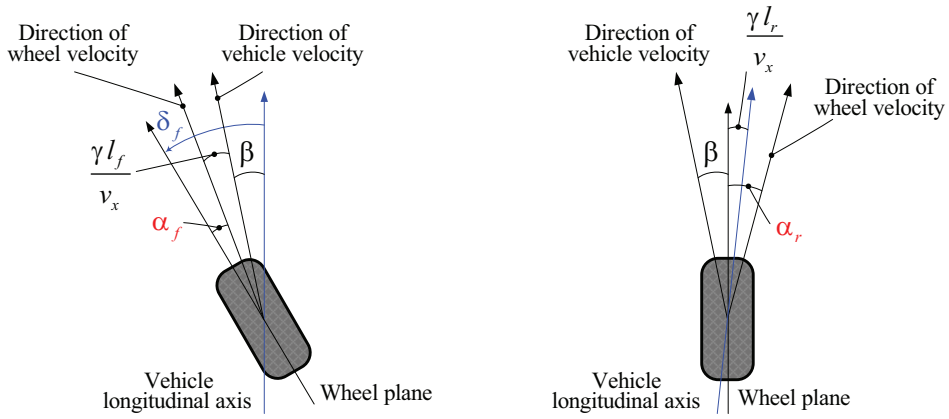

(a) Front wheel.

(b) Rear wheel.

Figure 2.7: Tire slip angle calculation for the single track vehicle model.

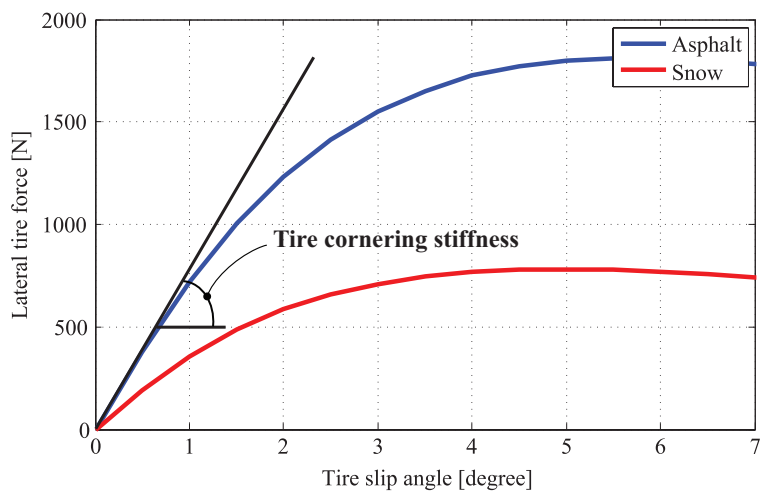

Figure 2.8: Front lateral tire force F_f^y over front tire slip angle α_f.

For small tire slip angles, the lateral tire forces, i.e., F_f^y and F_r^y in (2.22)–(2.24), are approximated to be proportional to the tire slip angles as shown in Figure 2.8 and can be represented as

$$F_f^y = -2C_f\alpha_f = -2C_f\left(\beta + \frac{\gamma l_f}{v_x} - \delta_f\right) \tag{2.27}$$

$$F_r^y = -2C_r\alpha_r = -2C_r\left(\beta - \frac{\gamma l_r}{v_x}\right) \tag{2.28}$$

where C_f and C_r are the tire cornering stiffnesses for front and rear tires, and are defined as follows:

$$C_f = \left.\frac{\partial F_f^y}{\partial \alpha_f}\right|_{\alpha_f=0} \quad \text{:Front tire cornering stiffness} \tag{2.29}$$

$$C_r = \left.\frac{\partial F_r^y}{\partial \alpha_r}\right|_{\alpha_r=0} \quad \text{:Rear tire cornering stiffness.} \tag{2.30}$$

Tire model is further discussed in following section.

From (2.23)–(2.28) with the small angle approximation (i.e., $\sin\delta_f \approx 0$ and $\cos\delta_f \approx 1$), the single track vehicle model becomes linear and time invariant system if it is assumed that the longitudinal vehicle velocity v_x is constant.This results in a 2-DOF model, with vehicle sideslip angle β and yaw rate γ as state variables. The inputs to the systems are front steering angle δ_f and yaw moment M_z. The state space equation is represented as follows:

$$\begin{aligned} \dot{x}(t) &= Ax(t) + Bu(t) \\ y(t) &= Cx(t) \end{aligned} \tag{2.31}$$

where $x = [\beta,\ \gamma]^T$, $u = [\delta_f,\ M_z]^T$, $y = \gamma$, and

$$A = \begin{bmatrix} \dfrac{-2(C_f + C_r)}{mv_x} & \dfrac{-2(l_f C_f - l_r C_r)}{mv_x^2} - 1 \\ \dfrac{-2(l_f C_f - l_r C_r)}{I_z} & \dfrac{-2(l_f^2 C_f + l_r^2 C_r)}{I_z v_x} \end{bmatrix}$$

$$B = \begin{bmatrix} \dfrac{2C_f}{mv_x} & 0 \\ \dfrac{2l_f C_f}{I_z} & \dfrac{1}{I_z} \end{bmatrix}, \quad C = \begin{bmatrix} 0 & 1 \end{bmatrix}.$$

Here, we can see that there are two states to be controlled and two controllable inputs. Moreover, it is found that that the variations of vehicle longitudinal velocity v_x cause noticeable changes in vehicle dynamic responses. That is, a damping coefficient and natural frequency of the vehicle dynamics model dominantly depend on vehicle longitudinal velocity. Thus proper gain scheduling strategies based on vehicle longitudinal velocity are required in control system design. It is

customary to design controllers for several velocity values and to use a gain scheduling controller (*Guvenc et al.*, 2009).

To further analyze the dynamics characteristics of vehicle motion, the relationship between controllable inputs and measurable or observable outputs is obtained. According to (2.31), the relationship between inputs and outputs is represented as follows:

$$\begin{bmatrix} \beta \\ \gamma \end{bmatrix} = \begin{bmatrix} G_{11}(s) & G_{12}(s) \\ G_{21}(s) & G_{22}(s) \end{bmatrix} \begin{bmatrix} \delta_f \\ M_z \end{bmatrix} = \Delta(s) \begin{bmatrix} G_{11}(0)(1+T_{11}s) & G_{12}(0)(1+T_{12}s) \\ G_{21}(0)(1+T_{21}s) & G_{22}(0)(1+T_{22}s) \end{bmatrix} \begin{bmatrix} \delta_f \\ M_z \end{bmatrix}$$

where $\Delta(s)$ is expressed as a second order filter having damping coefficient ζ and natural frequency ω_n:

$$\Delta(s) = \frac{\omega_n^2}{s^2 + 2\zeta\omega_n s + \omega_n^2} \tag{2.32}$$

Here,

$$\zeta = \frac{m(l_f^2 C_f + l_r^2 C_r) + I_z(C_f + C_r)}{2l\sqrt{mI_z C_f C_r(1 + K_s v_x^2)}}, \quad \omega_n = \frac{2l}{v_x}\sqrt{\frac{C_f C_r(1 + K_s v_x^2)}{mI_z}}$$
$$K_s = \frac{m(l_r C_r - l_f C_f)}{2l^2 C_f C_r}$$

where the K_s is the vehicle stability factor, which explains the steering characteristics of the

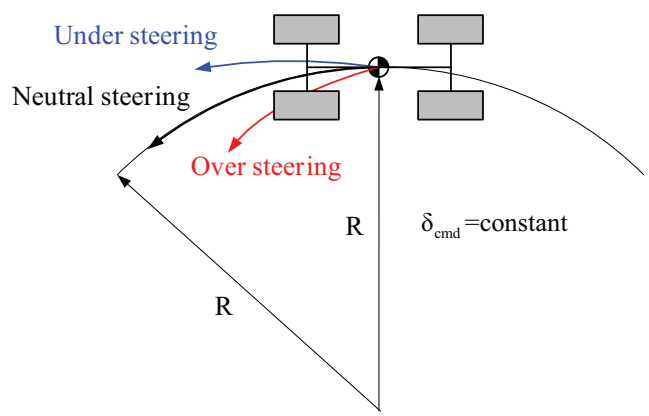

Figure 2.9: Steering characteristic of vehicle.

vehicles. The sign of $l_rC_r - l_fC_f$ in K_s represents vehicle motion behavior by steering action and the steering characteristics, illustrated in Figure 2.9, are classified as follow:

$$l_rC_r - l_fC_f \ > \ 0 \qquad : \text{under steering} \tag{2.33a}$$

$$l_rC_r - l_fC_f \ = \ 0 \qquad : \text{neutral steering} \tag{2.33b}$$

$$l_rC_r - l_fC_f \ < \ 0 \qquad : \text{over steering.} \tag{2.33c}$$

DC gains and derivative gains in aforementioned transfer functions are obtained as below:

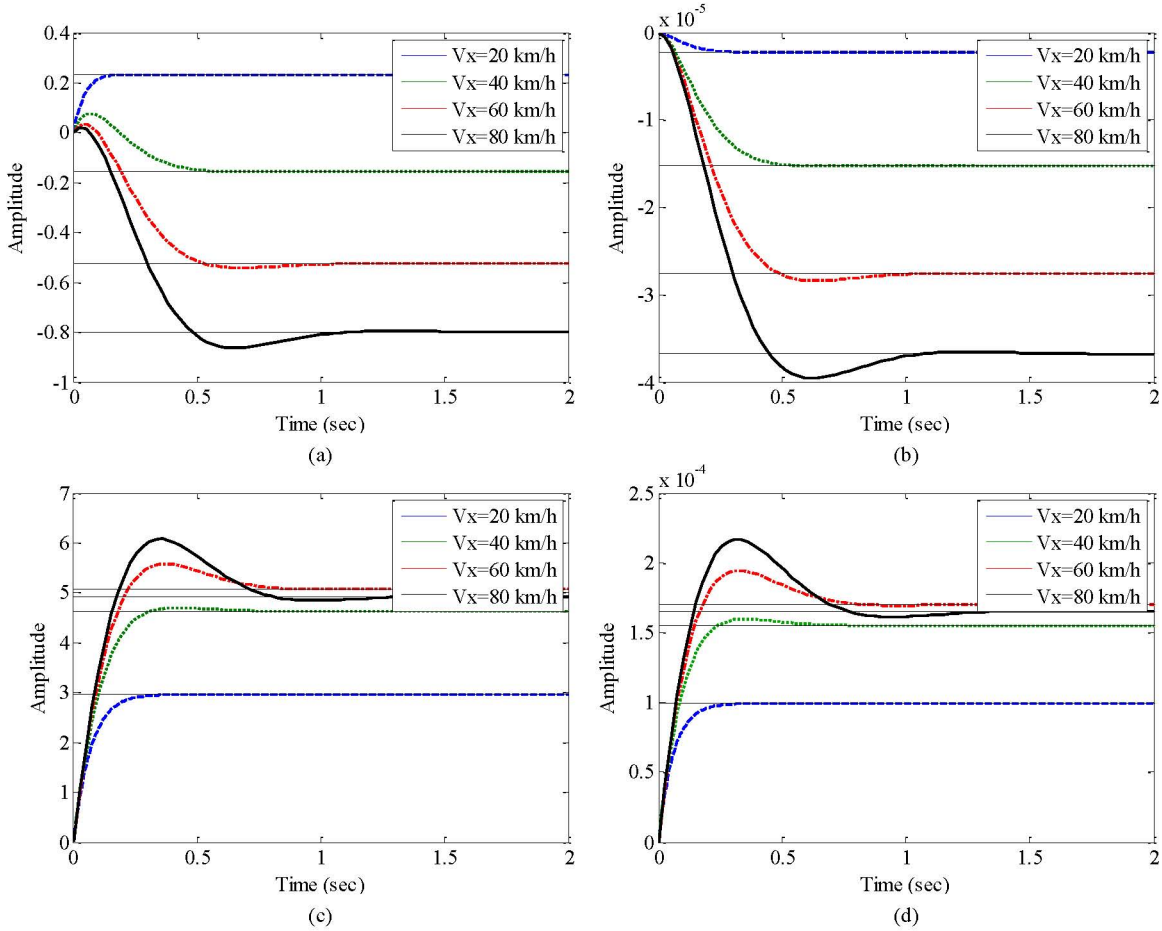

Figure 2.10: Step response of each transfer function. (a) Response of $G_{11}(s)$. (b) Response of $G_{12}(s)$. (c) Response of $G_{21}(s)$. (d) Response of $G_{22}(s)$.

$$G_{11}(0) = \frac{l_r\left(1-\frac{ml_f v_x^2}{2ll_rC_r}\right)}{l(1+K_s v_x^2)}, \qquad T_{11} = \frac{I_z v_x}{2ll_rC_r\left(1-\frac{ml_f v_x^2}{2ll_rC_r}\right)} \tag{2.34a}$$

$$G_{12}(0) = \frac{2(l_rC_r - l_fC_f) - mv_x^2}{4l^2C_fC_r(1+K_s v_x^2)}, \qquad T_{12} = 0 \tag{2.34b}$$

$$G_{21}(0) = \frac{v_x}{l(1+K_s v_x^2)}, \qquad T_{21} = \frac{ml_f v_x}{2lC_r} \tag{2.34c}$$

$$G_{22}(0) = \frac{(C_f+C_r)v_x}{2l^2C_fC_r(1+K_s v_x^2)}, \qquad T_{22} = \frac{mv_x}{2(C_f+C_r)}. \tag{2.34d}$$

Figure 2.10 shows the individual responses for the step input on dry asphalt (i.e., $\mu \simeq 0.9$). It is confirmed that vehicle responses vary with respect to longitudinal vehicle velocity v_x.

2.3 Tire Modeling

Forces and moments working on a tire hight influence the dynamics of the vehicle and thereby it is significantly important to use mathematical tire models to approximate the complicated tire behaviors for the purpose of state observers and controller design. This section focuses on mathematical tire models for describing the relationship between tire parameters, tire forces, and moments.

2.3.1 Tire Fundamental

Vehicle motion is dominantly governed by tire forces which are developed at contact patch of the tires. Thus, it is necessary to have full understanding of the relationship between the tire contact patch and the road surface. In general, tires serve three fundamental functions:

- A tire supports the weight of the vehicle and reduced the impact or shocks from the road.
- A tire develops the longitudinal forces for acceleration and deceleration.
- A tire develops the lateral forces for cornering.

For the modeling and theoretical analysis of tire behavior, the reference system and notation should be defined. Figure 2.11 shows the sign convention according to the SAE standard, with the longitudinal **X** axis alignrd with the wheel heading, the lateral **Y** axis perpendicular to the

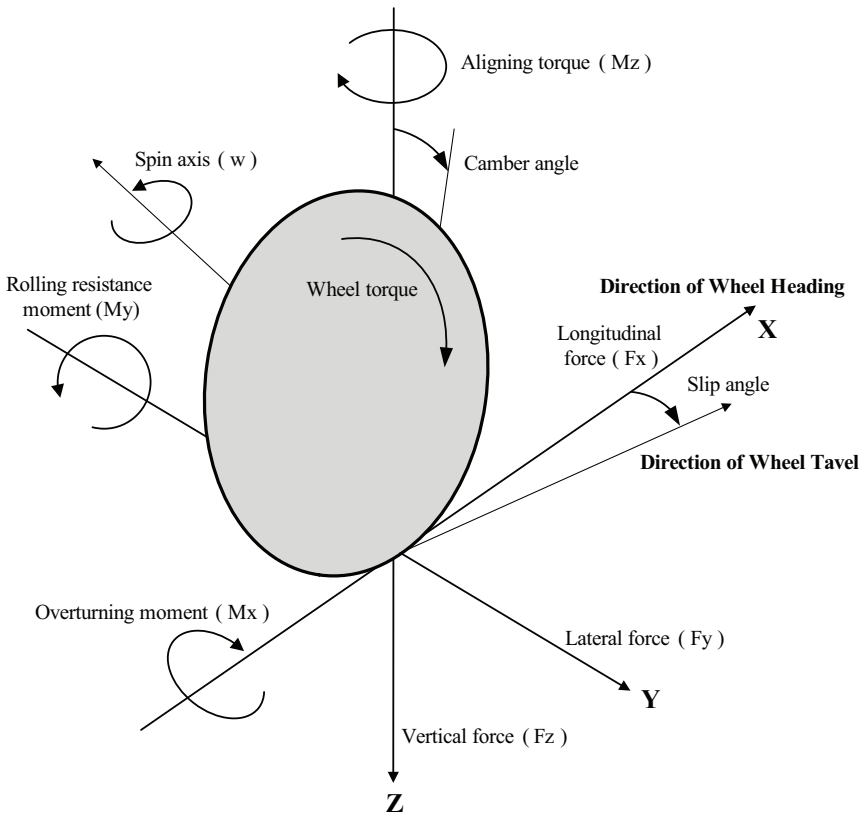

Figure 2.11: Forces and moments acting on a tire (SAE standard).

wheel, and the vertical **Z** axis pointing downwards. In this thesis, the choice of reference system follows the ISO standard which prescribes the direction of the **Z** axis to be upward, hence, the direction of both the **X** and **Y** axis differ from the reference systems of SAE standard (*Gillespie*, 1992).

The forces primarily concerned with vehicle handling and control purposes are the planar lateral and longitudinal forces, and the self-aligning moments. The longitudinal tire force F^x is generated during acceleration and deceleration. The lateral tire force F^y is generated when cornering. The self-aligning moment results from the fact that the planar forces have a point of action which is not positioned exactly under the wheel center. In addition, there are the rolling resistance force, which is related to the energy dissipation for a rolling tire, and the overturning moment which is the torque necessary to camber the wheel.

Over the past decades, a great deal of research has been dedicated to the development of tire models (*Gillespie*, 1992; *Pacejka*, 2006; *Svendenius et al.*, 2009; *Rajamani*, 2011). As a result,

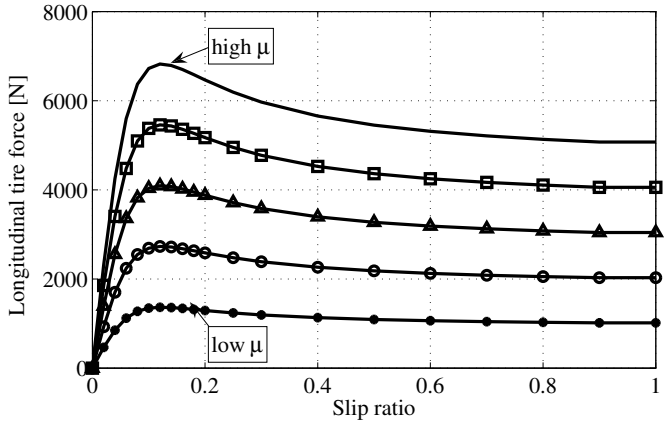

(a) Relationship between longitudinal tire force F^x and slip ratio λ under various road surfaces.

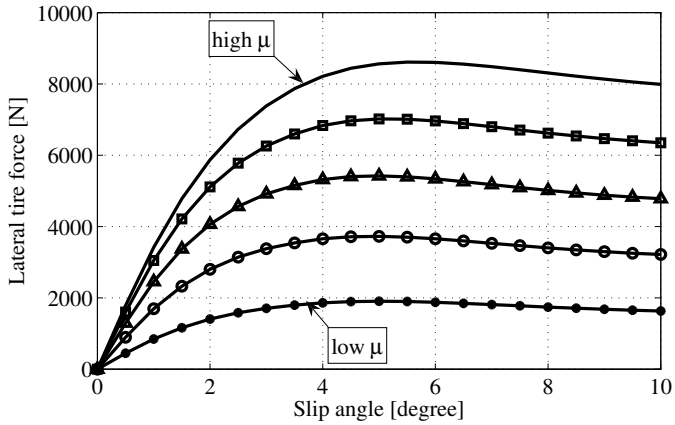

(b) Relationship between lateral tire force F^y and slip angle α under various road surfaces.

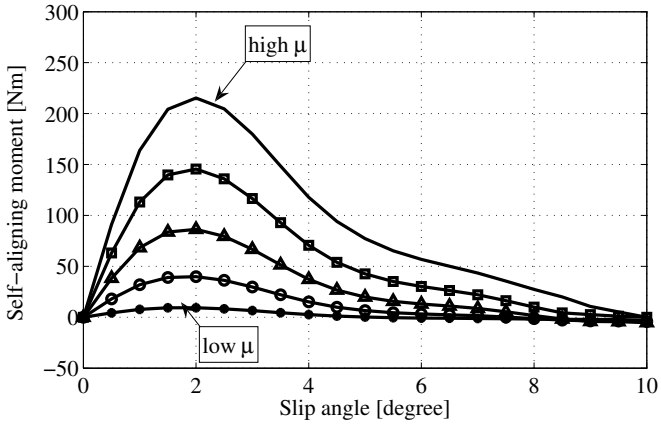

(c) Relationship between self-aligning moment and slip angle under various road surfaces.

Figure 2.12: Characteristics of tire forces and moment acting on a tire.

a variety of tire models, e.g., Magic Formula, Dugoff's model, and Brush model (*Pacejka*, 2006) etc., have been proposed and used in observer ans controller design. For example, a linear tire model has been widely used for the vehicle bicycle model because it provides a relatively good representation of tire behavior when the tire slip angle α is small. However, the linear tire model does not reflect the nonlinear effects due to the variations of the road friction. To treat these nonlinear effects, several nonlinear tire models have been presented.

2.3.2 Review on Existing Tire Models

A widely used empirical tire model is the Magic Formula which can be used to fit experimental tire data for characterizing the relationships between the longitudinal tire force and slip ratio, lateral tire force and slip angle, and self-aligning moment and slip angle. It is expressed as follows (*Bakker et al.*, 1987, 1989; *Pacejka and Besselink*, 1997; *Pacejka*, 2006):

$$y(x) = \mathrm{D}\sin\{\mathrm{C}\arctan[\mathrm{B}x - \mathrm{E}(\mathrm{B}x - \arctan \mathrm{B}x)]\} \tag{2.35}$$

$$Y(X) = y(x) + \mathrm{S}_v \tag{2.36}$$

$$x = X + \mathrm{S}_h \tag{2.37}$$

where $Y(X)$ represents the output variables: longitudinal tire force, lateral tire force, or self-aligning moment, and X denotes slip angle α or slip ratio λ. Coefficient B is called stiffness factor, C shape factor, D peak factor, and E curvature factor. S_h and S_v are the horizontal shift and vertical shift, respectively.

(2.35) produces a curve that passes through the origin, $x = y = 0$, and reaches a maximum at $x = x_m$, as shown in Figure 2.13. For given values of the coefficients, the curve shows an anti-symmetric shape with respect to the origin, $x = y = 0$. Figure 2.13 illustrates the physical meaning of some of the coefficients in (2.35). For example, if Figure 2.13 represents the relationship between the lateral tire force and slip angle, then coefficients D represents the peak value with respect to x, y coordinates and BCD corresponds to the slope of the curve at the origin, representing the tore cornering stiffness, as defined by (2.29) and (2.30).

It is noted that some of the coefficients in (2.35) and (2.37) are functions of the vertical tire

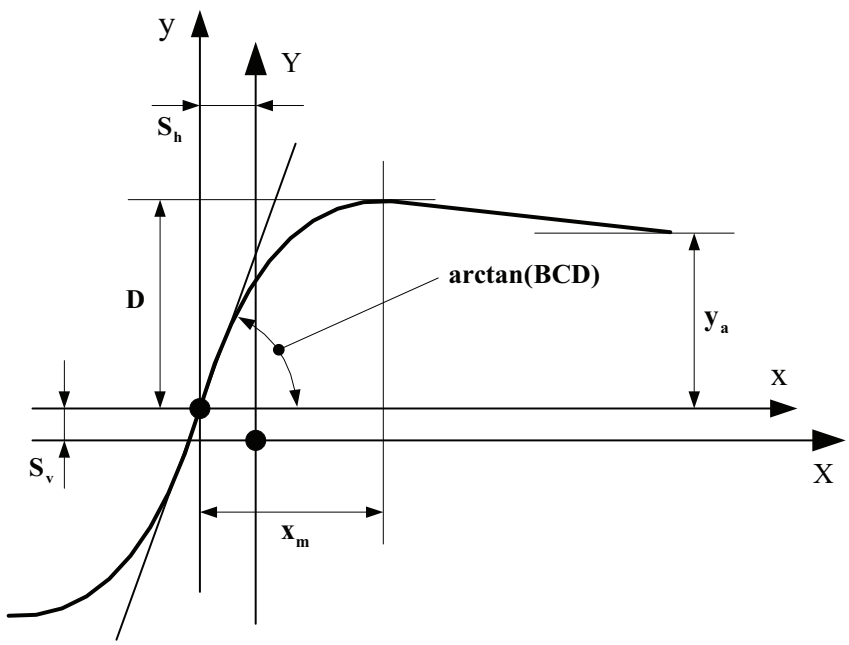

Figure 2.13: Characteristics of the Magic Formula (*Pacejka*, 2006).

force F^z and/or tire camber angle (*Bakker et al.*, 1987). The coefficients B, C, D, and E can be expressed as functions of the vertical tire force F^z and road friction coefficient μ as follows (*Pacejka and Bakker*, 1992):

$$\mathrm{D} \;=\; a_1(F^z)^2 + a_2F^z \tag{2.38}$$

where a_1 and a_2 are empirical coefficients.

For tire cornering stiffness (i.e., the initial slope of the lateral tire force–slip angle curve):

$$\mathrm{BCD} \;=\; a_3 \sin[a_4 \arctan(a_5F^z)] \tag{2.39}$$

For aligning stiffness (i.e., the initial slope of the self-aligning moment–slip angle curve) or longitudinal stiffness (i.e., the initial slope of the longitudinal tire force–slip ratio):

$$\mathrm{BCD} \;=\; \frac{a_3(F^z)^2 + a_4F^z}{e^{a_5F^z}} \tag{2.40}$$

The stiffness factor B and the curvature factor E are given by

$$\mathrm{B} = \frac{\mathrm{BCD}}{\mathrm{CD}} \tag{2.41}$$

$$\mathrm{E} = a_6(F^z)^2 + a_7F^z + a_8 \tag{2.42}$$

where a_1, a_2, $\cdots$, a_8 are empirical coefficients.

Another commonly used tire model is the Dugoff tire model. Dugoff tire model is an alternative to the elastic foundation analytical tire model developed by Fiala (1954) for lateral tire force generation and by Pacejka and Sharp for combined lateral and longitudinal tire force generation (*Pacejka and Sharp*, 1991). Dugoff tire model allows for independent values of tire stiffness in the longitudinal and lateral directions. Compared to the Magic Formula tire model, Dugoff tire model fas the advantage of being an analytically derived model developed from force balance calculations. Furthermore, the longitudinal and lateral tire forces are directly related to the tire-road friction coefficient in more transparent equations (*Rajamani*, 2011).

The longitudinal and lateral tire forces are defined as follows:

$$F_i^x = C_\lambda \frac{\lambda_i}{1+\lambda_i} f(s_i) \tag{2.43}$$

$$F_i^y = C_\alpha \frac{\tan(\alpha_i)}{1+\lambda_i} f(s_i) \tag{2.44}$$

where C_λ and C_α are the longitudinal and cornering stiffness of the tire. The tire slip λ_i is defined in (2.18) and (2.19). The variable s_i and the function$f(s_i)$ are given by

$$s_i = \frac{\mu F_i^z(1+\lambda_i)}{2\sqrt{(C_\lambda\lambda_i)^2 + (C_\alpha \tan(\alpha_i))^2}}$$

$$f(s_i) = \begin{cases} 1, & \text{if} \quad s_i \geq 1 \\ (2-s_i)s_i, & \text{if} \quad s_i < 1 \end{cases}$$

where μ is the tire-road friction coefficient and F_i^z is the vertical tire force for each wheel.

2.3.3 Dynamic Lateral Tire Force Model

The tires, which generate longitudinal, lateral forces and moments, have a significant effect on the dynamic characteristics of vehicles. These tire forces are explained by complex relation between tire-road friction, vertical force on the tire, variable tire slip angles, and elastic tire properties (*Pacejka*, 2006). In order to model the tire force generation, several tire models have been developed. A widely used empirical tire model (e.g., magic formula tire model) is dominantly based on empirical formulations deriving from tire test data and a large number of tire parameters. Hence, it is not suitable for real-time application to vehicle control systems. To avoid complex calculation and using tire test data, in this paper, we use linearized tire force models, i.e., (2.27) and (2.28). To account for transient behavior of tires, a typical dynamic model, which is the first order dynamics, is used and expressed as follows (*Abe and Manning*, 2009; *Rajamani*, 2011):

$$\tau_{\mathrm{lag},i}\dot{F}_i^y + F_i^y \quad = \bar{F}_i^y \tag{2.45}$$

where $\tau_{\mathrm{lag},i}$ is the relaxation time constant and calculated from the longitudinal vehicle velocity and tire relaxation length, which is the approximate distance needed to build up tire forces, and $\bar{F}_i^y$ is the lateral tire force from a linear tire model described in (2.27) and (2.28). From these points, the dynamic lateral tire force models for front and rear tires are obtained as

$$\dot{F}_f^y = -\frac{1}{\tau_{\mathrm{lag},f}}F_f^y - \frac{2C_f}{\tau_{\mathrm{lag},f}}\beta - \frac{2l_fC_f}{\tau_{\mathrm{lag},f}v_x}\gamma + \frac{2C_f}{\tau_{\mathrm{lag},f}}\delta_f \tag{2.46}$$

$$\dot{F}_r^y = -\frac{1}{\tau_{\mathrm{lag},r}}F_r^y - \frac{2C_r}{\tau_{\mathrm{lag},r}}\beta + \frac{2l_rC_r}{\tau_{\mathrm{lag},r}v_x}\gamma \tag{2.47}$$

where $\tau_{\mathrm{lag},f}$ and $\tau_{\mathrm{lag},r}$ are the relaxation time constants for front and rear tires, respectively.

Figure 2.14 shows the comparison result obtained from dynamics lateral tire force model and sensor measurement of lateral tire forces, respectively. Each result in Figure 2.14 is explained as: a result (1) illustrated in Figure 2.14 is obtained from a linear tire model (2.27) and measured tire slip angle (i.e., thick gray line), (2) is a low-pass filtered data of (1) (i.e., dotted red line),

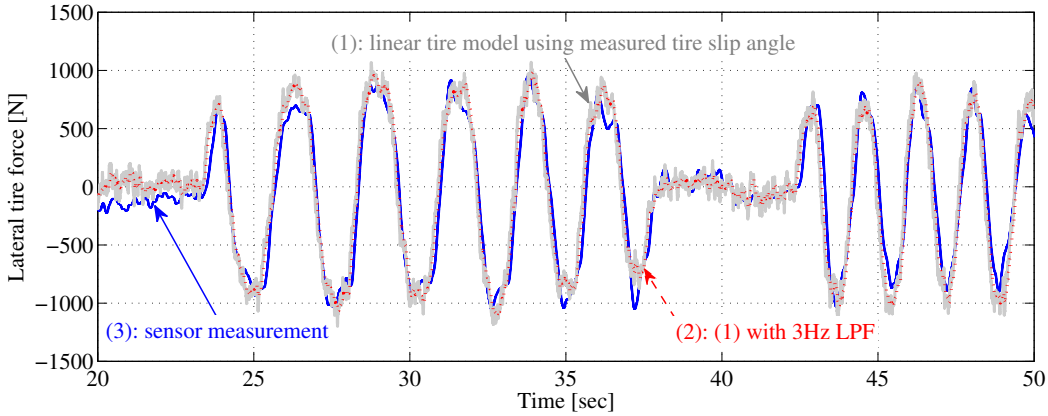

Figure 2.14: Dynamic lateral tire force model with time lag.

and (3) is a result of the directly measured front lateral tire force from MSHub units (i.e., thick blue line).

2.4 Experimental Electric Vehicle

The experimental electric vehicle, used for performance verification of observers and controllers, is presented in this section.

2.4.1 In-Wheel-Motor-Driven Electric Vehicle

The experimental electric vehicle named "FPEV–II Kanon", shown in Figure 2.16, was used for field tests. The "FPEV–II Kanon" was developed by the Hori/Fujimoto EV research team

(a) Hori/Fujimoto EV team. (b) Dr. Thomas D. Gillespie visit.

Figure 2.15: Research activities in Hori/Fujimoto EV research team.

Figure 2.16: Experimental in-wheel-motor-driven electric vehicle: Kanon.

Table 2.1: Specifications of FPEV–II Kanon.

In-wheel motor	
Type	Direct drive outer rotor type
Maximum Torque	500Nm(Front*)/340Nm(Rear*)
Maximum Power	20.0kW(Front*)/10.7kW(Rear*)
Weight	32kg(Front*)/26kg(Rear*)
Battery	
Type	Lithium-ion type
Capacity	5kWh
Numbers	10 modules (1module=4cell)
Control system	
Controller	AutoBox-DS1103
Sampling Time	0.001sec
Sensors	Gyro sensor, Wheel speed sensor, Steering angle sensor, Multi-sensing hub unit

Front*: one front wheel motor, Rear*: one rear wheel motor

(see Figure 2.15) and it has following special features.

1. In-wheel motors (i.e., Permanent magnet motors) are mounted in each wheel as shown in Figure 2.17. Therefore, we can control each wheel torque completely and independently for vehicle motion control. Regenerative braking is also available. The specifications of "FPEV–II Kanon" are listed in Table 2.1.

2. MSHub units for measuring lateral tire forces in real-time are installed in each wheel. Figure 2.19 shows the MSHub unit invented by NSK Ltd. (*Koichiro Ono*, 2009).

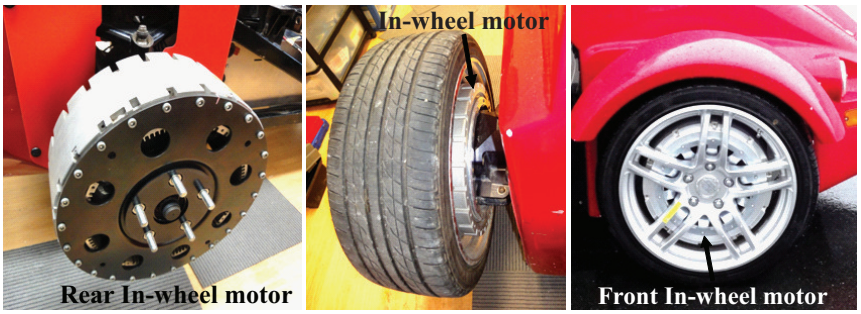

Figure 2.17: Real view of in-wheel-motor.

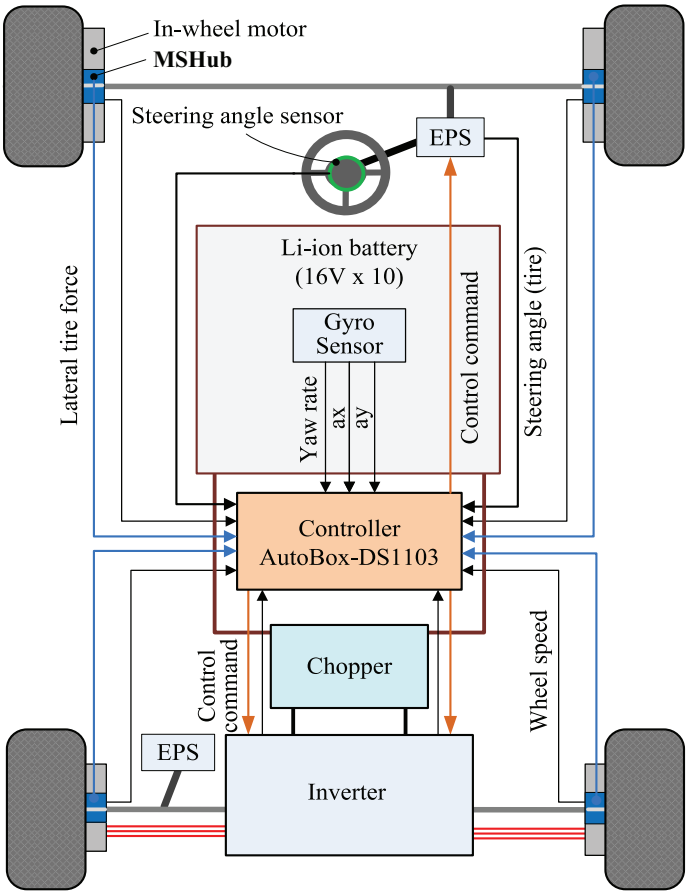

Figure 2.18: Schematic of electrical system of an experimental electric vehicle.

3. 4 wheel steering control is possible through front and rear EPS systems.

An experimental IWM-EV is also equipped with a gyro and acceleration sensors that measure yaw rate, longitudinal, and lateral acceleration. In addition, a non-contact optical sensor,

Correvit (Corrsys–Datron), is used for accurate measurements of side slip angle, lateral vehicle velocity and longitudinal vehicle velocity, and its outputs are connected to AutoBox. The Correvit sensor uses optical means to capture planar road texture and evaluate the motion of the vehicle by measuring the direction and magnitude of change with respect to the road texture. The dSPACE AutoBox (DS1103), which consists of a power PC 750GX controller board running at 933 MHz and 16 channel A/D converter and 8 channel D/A converter, was used for real-time data acquisition and control.

2.4.2 Lateral Tire Force Sensor: MSHub unit

In authors' previous literature *Nam et al.* (2011), cost-effective lateral tire force sensors, called MSHub units shown in Figure 2.19, are introduced and used for vehicle state estimation. In many conventional vehicles, wheel hub units with built-in active ABS sensors (i.e., wheel velocity sensor) were equipped. Comparing MSHub units with wheel hub units which are currently used in vehicles, MSHub units have almost the same mechanical structure except for rolling elements in a pair of rows and is capable of being constructed at a low cost. The measurement principle is as follows: the revolution speeds of rolling elements in a pair of rows are sensed by a pair of revolution speed sensors and difference of sensed revolution speeds is used to calculate the radial or axial loads (*Koichiro Ono*, 2009). As shown in Figure 2.19, a MSHub unit is installed on rotational axis of the wheel. Through novel load measuring techniques invented by NSK. Ltd., the accurate lateral tire force measurements using MSHub units can be realized without much additional cost and, due to cost-effective aspects, MSHub units are recently considered practically-applicable to vehicle control systems by several automotive manufacturers.

In literatures *Nam et al.* (2011, 2012a), lateral tire force estimation methods, using nonlinear tire models, lateral vehicle dynamics, and available sensors used in conventional vehicle systems, were presented and evaluated from field tests. Even though they can provide relatively accurate estimates without additional expensive sensors, there still exist limitations in actual application to vehicle control systems. Because these methods can not cope with the variation of parameters in nonlinear tire model and vehicle models and calculation complexity caused by large dimension of observer models is very challenging issue in practical application. Although, by using lateral

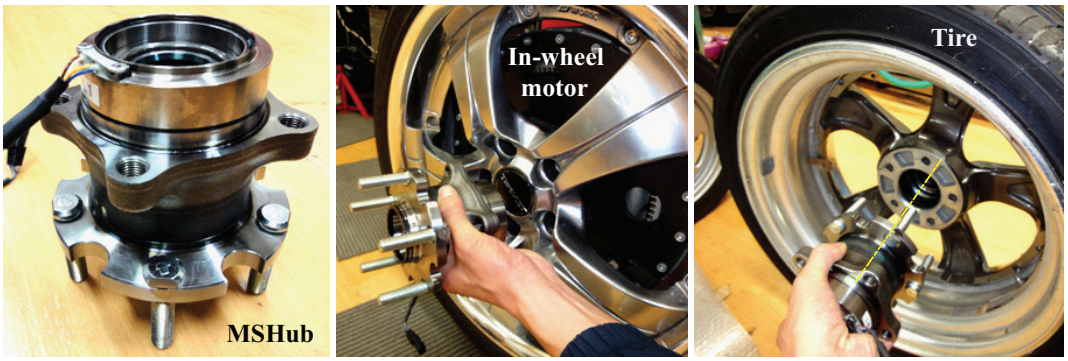

Figure 2.19: Real view of lateral tire force sensor, i.e., MSHub unit.

tire force sensors, a slight increase in sensor price is expected, this kind of cost-effective sensors can provide novel solutions in problems with vehicle state estimation and motion control.

2.5 Chapter Summary

Vehicle dynamics models and tire model, which are widely used in motion control systems, have been introduced in this chapter. Dynamic characteristics of a vehicle motion has been discussed by introducing transfer functions between controllable inputs and measurable or observable outs. Finally, an experimental IWM-EV, used for performance verification of proposed observers and controller, is presented and its special features are explained.

CHAPTER III

Vehicle Attitude Estimation Using Lateral Tire Force Sensors

3.1 Introduction

Vehicle motion control systems, such as yaw stability control, traction control, and roll stability control systems have developed to help drivers maintain stability, maneuverability, and customize the handling characteristics (*Tseng et al.*, 1999; *Abe and Manning*, 2009). However, these systems usually depend on real-time information on vehicle states and parameters, e.g., vehicle velocity, vehicle sideslip angle, roll angle, and tire parameters. Generally, the yaw rate is easily measured by cheap gyro sensors, but the vehicle velocity, sideslip angle, and roll angle cannot be measured directly due to the sensor cost and reliability issues. As a consequence, these states and parameters should be estimated. In particular, accurate vehicle sideslip angle estimation is necessarily required so as to enhance the vehicle safety. In previous literature *Aoki et al.* (2005); *Bevly et al.* (2006); *Piyabongkarn et al.* (2009); *You et al.* (2009); *Baffet et al.* (2009); *Doumiati et al.* (2009, 2010), several techniques for estimating the sideslip angle have been developed. Two conventional techniques are integrating an gyro sensor and lateral accelerometer directly (this method is called a sensor kinematics-based method) and using a physical vehicle models for state observer design (*Piyabongkarn et al.*, 2009; *You et al.*, 2009).

This chapter presents several methods for estimating vehicle sideslip angle, roll angle ,and tire cornering stiffness using lateral tire force sensors called MSHub units. Moreover, proposed estimation algorithms are implemented on experimental IWM-EV and experimental results, which are obtained from actual field tests under various driving and road conditions, are presented and discussed.

3.2 Literature Review on Vehicle Sideslip Angle Estimation

The conventional estimation methods of sideslip angle were proposed based on model-based observer design and direct sensor integration (*Phanomchoeng et al.*, 2011). The model-based estimation method has the advantages of high accuracy in linear tire region and robustness against sensor bias. However, the estimation accuracy is dominantly dependent on vehicle parameters, tire parameters, and driving conditions. Since it is difficult to correctly identify the vehicle parameters (e.g., mass) and tire parameters (e.g., tire cornering stiffness) in real-time, a model-based estimation method can not provide reliable estimation over all driving conditions.

3.2.1 Vehicle Model-Based Approach

The conventional estimation methods of side slip angle were proposed based on model-based observer design and direct sensor integration (*Rajamani et al.*, 2011a). The model-based estimation method has the advantages of high accuracy in linear tire region and robustness against sensor bias. However, the estimation accuracy is dominantly dependent on vehicle parameters, tire parameter, and driving conditions. Since it is difficult to correctly identify the vehicle parameters (e.g., mass) and tire parameter (e.g., cornering stiffness) in real-time, a model-based estimation method can not provide reliable estimation over all driving conditions.

In the model-based estimation method, a linear bicycle model is used for estimator design. Based on a linear bicycle model and a linear tire model, state observers and Kalman filter were mainly used for sideslip angle estimation (*Ray*, 1995; *Wenzel et al.*, 2006; *Doumiati et al.*, 2009; *Antonov et al.*, 2011). Based on state space equations (2.31), a state observer is designed as follows:

$$\begin{aligned} \dot{\hat{x}} &= A_b\hat{x} + B_b u + L(y - \hat{y}) \\ \hat{y} &= C_b\hat{x} \end{aligned} \tag{3.1}$$

where $\hat{x} = [\hat{\beta}_{\text{mod}} \;\; \hat{\gamma}]^T$, $u = [\delta_f \;\; M_z]^T$, and $y = \gamma$

$$A_b = \begin{bmatrix} \dfrac{-2(C_f + C_r)}{mv_x} & \dfrac{-2(l_f C_f - l_r C_r)}{mv_x^2} - 1 \\ \dfrac{-2l_f C_f + 2l_r C_r}{I_z} & \dfrac{-2l_f^2 C_f - 2l_r^2 C_r}{I_z v_x} \end{bmatrix}$$

$$B_b = \begin{bmatrix} \dfrac{2C_f}{mv_x} & 0 \\ \dfrac{2l_f C_f}{I_z} & \dfrac{1}{I_z} \end{bmatrix}, \quad C_b = \begin{bmatrix} 0 & 1 \end{bmatrix}.$$

From the above state observer, the model-based sideslip angle estimate, $\hat{\beta}_{\text{mod}}$, is obtained. The critical aspect of this approach is that estimation performance dominantly relies on the tire model and variations in vehicle parameters. In order to minimize the effects of model mismatch, several researchers have proposed estimation methods for cornering stiffness, which is dependent on tire-road friction coefficients. In *Geng et al.* (2009), a novel linear observer that uses a lateral acceleration sensor and yaw rate sensor as sensor measurements was proposed, and a fuzzy rule-based observer was also designed in order to cope with nonlinearities in vehicle models.

3.2.2 Sensor Kinematics-Based Approach

The sensor kinematics-based estimation method is based on the kinematic relationship among sensor measurements (*Piyabongkarn et al.*, 2009). The equation of sensor kinematics is expressed as

$$\dot{\hat{\beta}}_{\text{kin}} = \frac{a_{ym} - g\phi}{v_x} - \gamma. \tag{3.2}$$

In order to obtain sideslip angle from (3.2), a direct numerical integration of (3.2) is required, but this causes a signal drift problem due to sensor bias. Moreover, since the lateral acceleration measurement contains a gravity effect caused by roll motion, the gravity effect should be compensated for accurate estimation (e.g., over-estimation is avoided by compensating the gravity effect). In practice, the numerical integration with a suitable forgetting factor is carried out to avoid severe signal drift.

In *Piyabongkarn et al.* (2009); *You et al.* (2009), the combined method of model-based estimation and kinematics-based estimation was proposed to make use of advantages of the two estimation methods. The model-based estimate is used at low frequencies (i.e., with low pass filter) while the kinematics-based estimate is used at higher frequencies (i.e., with high pass filter). The estimated sideslip angle from the combined estimation method was expressed as

(*Piyabongkarn et al.*, 2009)

$$\hat{\beta}_{\text{com}} = \frac{1}{1+\tau s}\hat{\beta}_{\text{mod}} + \frac{\tau}{1+\tau s}\dot{\hat{\beta}}_{\text{kin}} = \frac{1}{1+\tau s}\hat{\beta}_{\text{mod}} + \frac{\tau s}{1+\tau s}\hat{\beta}_{\text{kin}}. \tag{3.3}$$

Here, the parameter, τ, is utilized for the filter setting.

3.2.3 Nonlinear Approach

The state observer design based on physical vehicle models has challenged by system-model mismatch, e.g., unmodeled dynamics, parameter variations, etc., and the presence of unknown and unmeasurable disturbances. To make the estimator robust against these nonlinear factors, nonlinear estimation techniques such as KF, EKF, sliding mode observer, and new nonlinear observers have been proposed in many literature (*Baffet et al.*, 2007a,b; *Doumiati et al.*, 2011; *Zhao et al.*, 2011; *Phanomchoeng et al.*, 2011). The sliding mode observer is a well-known nonlinear estimation method characterized by its robustness against parameter variations. However, this method suffers from the "chattering" problem. The KF and EKF have been widely used in vehicle control systems due to its advantages to be a stochastic filter simply formulated. However, in practical applications, several challenging problems are addressed, which is the calculation complexity of the Jacobian matrices causing implementation difficulties. To overcome these drawbacks, unscented KF is introduced to improve EKF, especially for strongly nonlinear systems (*Doumiati et al.*, 2011). Since the unscented KF acts directly on the nonlinear model and approximates the states by using a set of sigma points, complex linearization procedures can be avoided.

3.3 Proposed Estimation Method I: Kinematics-Based Approach

3.3.1 Estimation Algorithm

A novel method to estimate vehicle sideslip angle is proposed based on lateral vehicle velocity estimation. The proposed method uses the lateral tire forces which can be measured from MSHub units. Note that if the vehicle longitudinal and lateral velocities are obtained, the vehicle sideslip angle can be easily calculated. The lateral vehicle velocity is estimated using a RLS algorithm

and its estimate is used to finally calculate the vehicle sideslip angle.

In order to design a lateral vehicle velocity estimator, a simplified lateral tire force model from the Dugoff's tire model shown in (2.44) (i.e., the effects of longitudinal tire force are neglected, see *Rajamani* (2011)) is used.

$$F_i^y = -C_i \tan(\alpha_i). \tag{3.4}$$

The above simplified lateral tire force model is applied to front left and right tires, respectively. For purposes of lateral vehicle velocity estimation, lateral tire force models for front tires are utilized based on following assumptions.

1. The left and right tires have pure tire slip conditions with negligible longitudinal slip and the peak lateral tire force occurs at the same tire slip angle. Tire slip angles, where the peak lateral tire forces occur at, are affected by weight transfer of vehicles. In contrast to engine vehicles, in-wheel-motor-driven electric vehicles, having battery packs under the floor and driving motors attached in wheels, can lower a CG of the vehicle. This provides the less weight transfer and thereby improves the driving stability. From these features, variations in front left and right tire forces due to weight transfer are not considered.

2. Front left and right tire cornering stiffnesses are the same (i.e., $C_{fl} = C_{fr} \approx C_f$). Considering that front tires are on the same road surface and effects of weight transfer are not critical, effects of weight transfer in tire cornering stiffnesses of left and right tires are not considered.

3. From the small angle approximation, $\tan(\alpha_i) \approx \alpha_i$.

From aforementioned assumptions, front left and right lateral tire forces can be expressed as follows:

$$F_{fl}^y = -C_{fl}\alpha_{fl} \approx -C_f \left(\frac{v_y + \gamma l_f}{v_x - \gamma d/2} - \delta_f \right) \tag{3.5}$$

$$F_{fr}^y = -C_{fr}\alpha_{fr} \approx -C_f \left(\frac{v_y + \gamma l_f}{v_x + \gamma d/2} - \delta_f \right). \tag{3.6}$$

By dividing (3.5) by (3.6), the lateral vehicle velocity v_y is derived as

$$v_y = \gamma l_f - \frac{\delta_f (F_{fl}^y - F_{fr}^y)}{\dfrac{F_{fl}^y}{v_x + \gamma d/2} - \dfrac{F_{fr}^y}{v_x - \gamma d/2}} \tag{3.7}$$

where the estimated lateral vehicle velocity is defined as a pseudo-measurement and expressed as $\tilde{v}_y$. As described in (3.7), the proposed estimation method makes use of the ratio of front left and right lateral tire forces and is based on linearized tire models of front left and right tires by above assumptions. Even though we use linearized tire models in estimator design, the proposed estimator shows better estimation results with relatively small errors compared with results of conventionally used methods, even when lateral tire forces reach a peak value [e.g., up to 5 m/s^2 of lateral acceleration, see Figure 3.2(b)]. We can confirm that a proposed estimator is robust against road conditions without using complicated nonlinear tire models only if front tires are on the same road surface. In a following section, this pseudo-measurement $\tilde{v}_y$ is used as a sensor measurement in the roll angle estimator using a KF.

Considering that all output data and input data are determined at sample instant, v_y described in (3.7) can thus be formulated by the RLS algorithm.

$$y(t) = \varphi^T(t)\theta(t) \tag{3.8}$$

where the estimated parameter $\theta(t)$, input regression $\varphi^T(t)$, and measured output $y(t)$ are given as

$$\theta(t) = \tilde{v}_y \tag{3.9a}$$

$$\varphi^T(t) = \left(\frac{F_{fl}^y}{v_x + \gamma d/2} - \frac{F_{fr}^y}{v_x - \gamma d/2} \right) \tag{3.9b}$$

$$y(t) = \gamma l_f \left(\frac{F_{fl}^y}{v_x + \gamma d/2} - \frac{F_{fr}^y}{v_x - \gamma d/2} \right) - \delta_f (F_{fl}^y - F_{fr}^y). \tag{3.9c}$$

The ultimate goal of the RLS algorithm is to provide parameter estimates that minimize the

following weighted least squares criterion (*Ljung*, 1999):

$$\hat{\theta}(t) \;=\; \arg\min_{\theta}\left\{\sum_{k=1}^{t}\Gamma(t,k)\cdot\rho[\varepsilon(k|\theta)]\right\} \tag{3.10}$$

Here, $\Gamma(t,k)$ is the weight on the prediction errors at time k, and $\rho(\varepsilon)$ is the cost function which is defined as $\rho(\varepsilon) = 1/2\varepsilon^2$. If the prediction errors can be assumed to be Gaussian with zero mean values, the defined cost function is reasonable.

The recursive process of the RLS algorithm, in a KF interpretation, is described as

$$\begin{aligned}
\hat{\theta}(t) &= \hat{\theta}(t-1) + K(t)\cdot\varepsilon\Big(t|\hat{\theta}(t-1)\Big) \\
\varepsilon\Big(t|\hat{\theta}(t-1)\Big) &= y(t) - \hat{y}\Big(t|\hat{\theta}(t-1)\Big) = y(t) - \varphi^T(t)\cdot\hat{\theta}(t-1) \\
K(t) &= P(t-1)\varphi(t)[\lambda I + \varphi^T(t)P(t-1)\varphi(t)]^{-1} \\
P(t) &= \frac{1}{\lambda}[I - K(t)\varphi^T(t)]P(t-1)
\end{aligned} \tag{3.11}$$

where I is the identity matrix, $\varepsilon(t)$ is the prediction error, and $K(t)$ and $P(t)$ are the Kalman gain and covariance matrices.

In order to cope with time-varying properties in a vehicle system, the weighted least squares criterion (3.10) is handled by putting less weight on older measurements. Therefore, the weighting function is set to (*Ljung*, 1999)

$$\Gamma(t,k) = \lambda^{t-k}; \quad \text{i.e., } \lambda(t) \equiv \lambda \tag{3.12}$$

where the choice of forgetting profile $\Gamma(t,k)$ shown in (3.10) is conceptually simple. It is common to select it so that the least square criterion (3.10) essentially contains those measurements that are relevant for the current properties of the system (*Ljung*, 1999). For a system which changes gradually and in a "stationary manner," the most common choice is to take a constant forgetting factor such as (3.12). The forgetting factor λ is always chosen to be a positive constant slightly smaller than 1 so that $\Gamma(t,k) = e^{(t-k)\log\lambda} \approx e^{-(t-k)(1-\lambda)}$. This means that measurements which are older than $T_0 = 1/(1-\lambda)$ samples are included in the criterion with a weight that is $e^{-1} \approx 36\%$

of that of the most recent measurements. It is called a "memory time constant" of the criterion and is represented as

$$T_0 = (1 - \lambda)^{-1} \tag{3.13}$$

If the system remains approximately constant over T_0 samples, a suitable choice of λ can then be made from (3.13). Since the sampling interval typically reflects the natural time constants of the system dynamics, thus, we can choose λ so that $(1-\lambda)^{-1}$ reflects the ratio between the time constants of variations in the dynamics and those of the dynamics itself. Typical choices of λ are in the range between 0.95 and 0.999. The smaller λ is, the less weight is assigned to the older data; that is, the past data are forgotten faster. In this paper, λ around 0.995 was selected to make reasonable trade-off between tracking ability and noise sensitivity.

From the RLS algorithm (3.11), the lateral vehicle velocity is estimated and used to calculate the vehicle sideslip angle. The sideslip angle is easily calculated with vehicle velocity and pseudo-measurement $\tilde{v}_y$. The average value of the non-driven wheel velocities is used as a vehicle velocity. Considering that an electric vehicle used in field tests was a rear-wheel drive vehicle, it is reasonable to use non-driven wheel's velocity as a vehicle velocity. In case that the wheel slip occurs in non-driven wheels due to sudden braking, we cannot use non-driven wheel's velocity for calculating the vehicle velocity. However, rear-wheel drive electric vehicles have Anti-lock Braking System (ABS), which contributes to keeping a vehicle steerable and stable during heavy braking moments by preventing wheel lock, for efficient braking of non-driven wheels and thereby severe wheel slip in non-driven wheels can be avoided.

Compared with the aforementioned conventional estimation methods, the main advantages of the proposed estimation method, utilizing lateral tire force sensors, are summarized in three points. First, it is robust against variations in vehicle parameters and tire-road conditions. Second, the proposed method can be easily realized without using additional sensors. Finally, the proposed recursive algorithm is very simple and can be easily implemented in real-time. Moreover, the estimated sideslip angle can be used to identify cornering stiffness in (3.5) and (3.6). The real-time information on cornering stiffness will contribute to improving the control performance of advanced motion control systems.

3.3.2 Estimation Algorithm Considering the Effects of Weight Transfer

An estimation algorithm, presented in Section 3.3.1, is developed with an assumption that tire cornering stiffness is constant with respect to weight transfer. To further consider the effect of weigh transfer on tire cornering stiffness (see Figure 3.1), we use the simplified tire cornering stiffness equation which is represented by a first-order polynomial with respect to the vertical tire force, as shown as follows:

$$C_{fl} = \frac{2F_{fl}^z}{F_{fl}^z + F_{fr}^z} \cdot C_f = \kappa_1 \cdot C_f \quad \text{:Cornering stiffness for the front left tire} \tag{3.14}$$

$$C_{fr} = \frac{2F_{fr}^z}{F_{fl}^z + F_{fr}^z} \cdot C_f = \kappa_2 \cdot C_f \quad \text{:Cornering stiffness for the front right tire} \tag{3.15}$$

From aforementioned equations, lateral tire force equations, i.e., (3.5) and (3.6), can be represented as

$$F_{fl}^y = -C_{fl}\alpha_{fl} \approx -\kappa_1 C_f \left(\frac{v_y + \gamma l_f}{v_x - \gamma d/2} - \delta_f \right) \tag{3.16}$$

$$F_{fr}^y = -C_{fr}\alpha_{fr} \approx -\kappa_2 C_f \left(\frac{v_y + \gamma l_f}{v_x + \gamma d/2} - \delta_f \right). \tag{3.17}$$

The estimated parameter $\theta(t)$, input regression $\varphi^T(t)$, and measured output $y(t)$ can be given

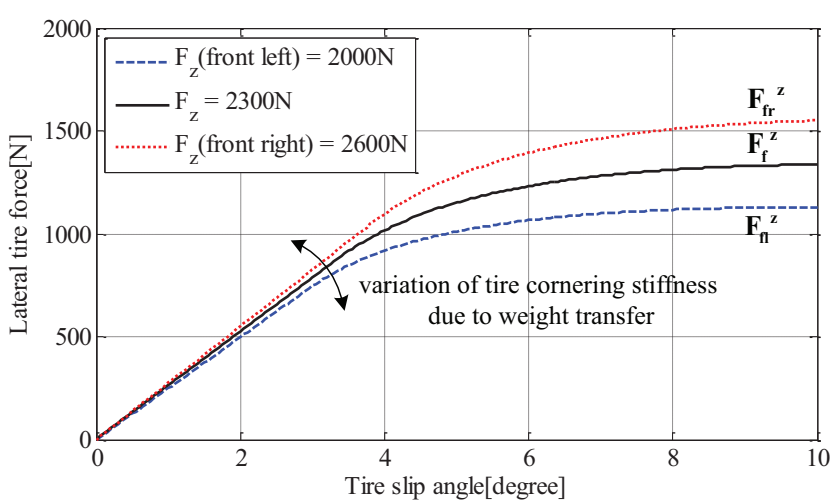

Figure 3.1: Effect of the weight transfer on lateral tire force–tire slip angle curve.

as

$$\theta(t) = \tilde{v}_y \tag{3.18a}$$

$$\varphi^T(t) = \left(\frac{{\kappa_1}^{-1} F_{fl}^y}{v_x + \gamma d/2} - \frac{{\kappa_2}^{-1} F_{fr}^y}{v_x - \gamma d/2} \right) \tag{3.18b}$$

$$y(t) = \gamma l_f \left(\frac{{\kappa_1}^{-1} F_{fl}^y}{v_x + \gamma d/2} - \frac{{\kappa_2}^{-1} F_{fr}^y}{v_x - \gamma d/2} \right) - \delta_f ({\kappa_1}^{-1} F_{fl}^y - {\kappa_2}^{-1} F_{fr}^y), \tag{3.18c}$$

where, κ_1 and κ_2 are calculated by using estimated vertical tire forces (see Chapter 4.2.3) in real time, and a RLS algorithm (3.11) is also used to estimate the lateral vehicle velocity.

In reality, effects of weight transfer on the performance of a proposed estimation method, presented in previous Section, are neglected when a vehicle is under normal driving conditions such as smooth cornering. However, when a vehicle is on sudden cornering situation, relatively large weight transfer occurs and thereby we should compensate for the effects due to weight transfer so as to provide more accurate state estimation.

3.3.3 Experimental Verification

The proposed estimation algorithms were implemented on the experimental electric vehicle shown in Figure 2.16. Moreover, to verify the effectiveness of the proposed method through comparison study, conventional estimation methods were also implemented and those results are evaluated by comparing the results of a proposed method.

In this thesis, a variety of field tests were performed with following driving conditions:

- constant vehicle speed,
- various steering commands, e.g., pulse steering, sine steering, and random steering, and these steering actions are accurately achieved via a steer-by-wire (SbW) actuator,
- without activation of vehicle motion controllers such as anti-slip control or yaw stability control (this means that the same current commands are applied to rear left and right in-wheel motors, i.e., control input M_z is equal to zero),

- rear-wheel driving mode, i.e., torque command from a driver is only transmitted to rear left and right in-wheel motors, and
- different road surfaces, e.g., dry asphalt ($\mu \simeq 0.9$), wet asphalt ($\mu \simeq 0.7$), or a slippery road ($\mu \simeq 0.3$).

Experimental results obtained from a random steering test at $v_x = 40$ km/h are shown in Figure 3.2(a). Even though estimated sideslip angles obtained from model-based estimation method and combined method follow the measured sideslip angle, there still exist estimation errors due to model uncertainties in the observer model and numerical integration errors. On the other hand, the proposed estimation method shows more accurate estimation. In this result, the sensor measurement (i.e., thick gray line) is the actual value which is directly measured from the non-contact optical sensor. Figure 3.2(b) and (c) show the results obtained from a pulse steering test and slalom test at $v_x = 50$ km/h on wet asphalt, respectively. The estimation results for two conventional methods contain errors with phase lag. The proposed estimation method provides very accurate estimation without any noticeable phase lag. To verify the robustness of the proposed estimation method, field tests on a slippery road (i.e., $\mu \simeq 0.3$) were also carried out.

Even though the results show larger estimation errors compared with the results on dry and wet asphalt, the estimation error was significantly decreased by applying the proposed method.

For quantitative evaluation of the proposed estimation method, the RMS values of estimation errors for different field tests were compared.

$$\text{RMS error} \quad = \quad \sqrt{\frac{1}{N}\sum_{j=1}^{N}(\hat{\beta}_j - \beta_{\text{sensor},j})^2} \tag{3.19}$$

where N is the number of samples. $\hat{\beta}_j$ and $\beta_{\text{sensor},j}$ represent the estimated and measured sideslip angles at the jth sample. (a)–(c), seen in Figure 3.3, correspond to the test results, shown in Figure 3.2(a)–(c). As shown in Figure 3.3, the proposed estimation method shows much smaller RMS values.

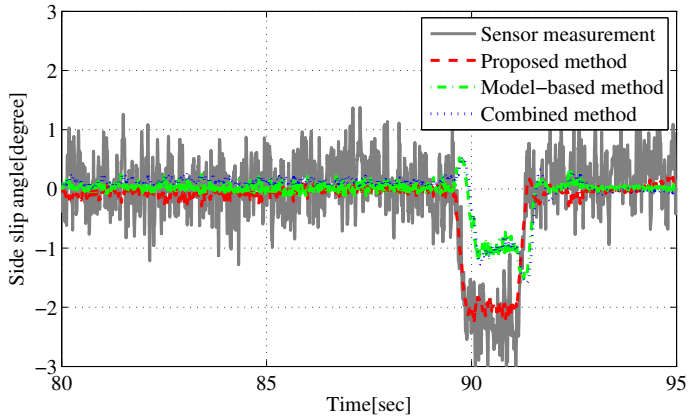

(a)

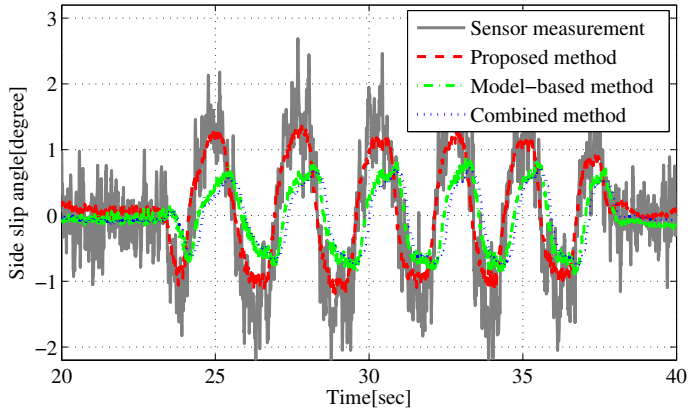

(b)

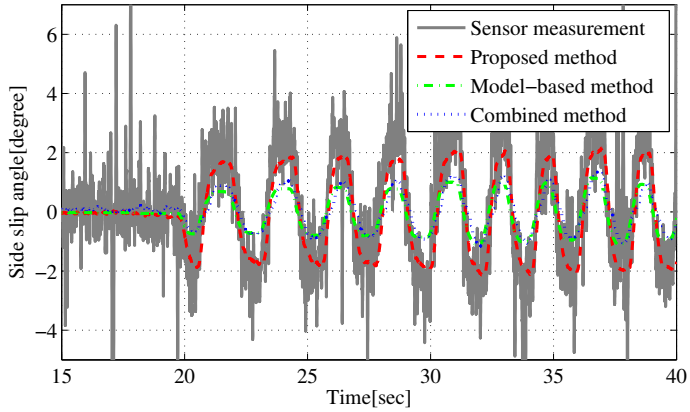

(c)

Figure 3.2: Experimental results for the sideslip angle estimation. (a) Random steering test on dry asphalt (i.e., $\mu \simeq 0.9$) with maximum lateral acceleration 5 m/s^2. (b) Pulse steering test on wet asphalt (i.e., $\mu \simeq 0.7$) with maximum lateral acceleration 6 m/s^2. (c) Slalom test on wet asphalt (i.e., $\mu \simeq 0.7$) with maximum lateral acceleration 4 m/s^2.

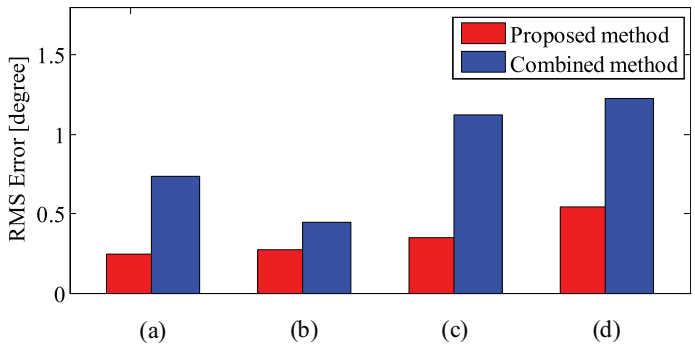

Figure 3.3: Calculated RMS errors for estimation.

3.4 Proposed Estimation Method II: Nonlinear Filtering Approach

The observation system based on vehicle dynamics models is highly nonlinear and presents unmodeled dynamics. For example, nonlinear phenomenon, shown in tire-road interaction, is that tire slip angle continues to grow, the tire forces begin to saturate and reach a peak value. Tire cornering stiffness, i.e., C_f and C_r, varies with respect to road condition change. To overcome these nonlinear characteristics, an EKF is designed for accurately and robustly estimating vehicle sideslip angle. A proposed EKF algorithm is implemented on an experimental IWM-EV and its performance is evaluated.

3.4.1 Tire Cornering Stiffness Estimation

In this section, a real-time algorithm for estimating tire cornering stiffness is presented. A single track vehicle model (i.e., bicycle model) is used for state estimation and stability control. This vehicle model includes the so called tire cornering stiffness which describes the tire-road condition and is a time-varying parameter. In general, there is a significant difference in the value of tire cornering stiffness depending on road conditions (e.g., whether the road is dry asphalt or a slippery road.) and the value is higher on dry asphalt than on a wet and slippery road. In *Sierra et al.* (2006), several methods for cornering stiffness estimation were developed and evaluated using experimental data. In *Nguyen et al.* (2011), the novel method for cornering stiffness estimation using lateral tire force sensors is proposed. In this paper, using a method proposed by *Nguyen et al.* (2011), linear tire models, and measured lateral tire forces, we obtains a linear regression model (i.e., the parameter to be identified is C_f/C_r) for tire cornering stiffness

estimation. Furthermore, using the following front left and right lateral tire force models (3.20), (3.21), we can have a regression model (i.e., a parameter to be identified is C_f).

$$F_{fl}^{y} = -C_{fl}\left(\frac{v_y + \gamma l_f}{v_x - \gamma d/2} - \delta_f\right) \tag{3.20}$$

$$F_{fr}^{y} = -C_{fr}\left(\frac{v_y + \gamma l_f}{v_x + \gamma d/2} - \delta_f\right) \tag{3.21}$$

where it is assumed that the tire cornering stiffnesses of left and right tires are the same (i.e., $C_{fl} = C_{fr} \approx C_f$). In general, tire cornering stiffness is affected by weight transfer of vehicles. In contrast to engine vehicles, IWM-EV, having battery packs under the floor and driving motors attached in wheels, can lower a CG of the vehicle. This provides a less weight transfer and thereby improves the driving stability. From these features, variations in front left and right tire cornering stiffnesses due to weight transfer are not considered. Using lateral vehicle dynamics (2.23), (2.24), and aforementioned lateral tire force equations for front left and right tires (3.20),(3.21), the regression model with respect to tire cornering stiffness can be obtained.

The tire cornering stiffness is identified using the following regression model.

$$y(t) \;=\; \varphi^T(t)\theta(t) \tag{3.22}$$

where the parameter to be identified $\theta(t)$, input regression $\varphi^T(t)$, and measured output $y(t)$ are given as (*Nguyen et al.*, 2011)

$$y(t) = \begin{bmatrix} F_f^y \\ F_{fr}^y\left(v_x + \frac{d\gamma}{2}\right) - F_{fl}^y\left(v_x - \frac{d\gamma}{2}\right) \end{bmatrix}$$

$$\varphi^T(t) = \begin{bmatrix} 2\delta_f - \frac{2\gamma l}{v_x} & F_r^y \\ d\gamma\delta_f & 0 \end{bmatrix}$$

$$\theta(t) = \begin{bmatrix} C_f \\ \frac{C_f}{C_r} \end{bmatrix}.$$

Tire cornering stiffness in aforementioned equations is estimated by making use of the RLS

algorithm as follows:

$$
\begin{aligned}
\hat{\theta}[t] &= \hat{\theta}[t-1] + \mathrm{Proj}_{\hat{\theta}}\{K[t](y[t] - \varphi[t]^T \cdot \hat{\theta}[t-1])\} \\
K[t] &= \frac{P[t-1]\varphi[t]}{\lambda I + \varphi^T[t]P[t-1]\varphi[t]} \\
P[t] &= \frac{1}{\lambda}(I - K[t]\varphi^T[t])P[t-1] \\
\mathrm{Proj}_{\hat{\theta}}(\bullet_j) &= \begin{cases} 0, \text{ if } \hat{\theta}_j \geq \theta_{j,\max} \text{ and } \bullet_j > 0 \\ 0, \text{ if } \hat{\theta}_j \leq \theta_{j,\min} \text{ and } \bullet_j < 0 \\ \bullet_j, \text{ otherwise} \end{cases}
\end{aligned}
\tag{3.23}
$$

where I is the identity matrix, $K[t]$ and $P[t]$ are the Kalman gain matrix and covariance matrix, respectively.

In reality, tire cornering stiffness is constrained depending on road conditions. This constraint can be enforced by projecting the estimates back into defined values [i.e., $C_f \in (C_{f,\min}, C_{f,\max})$, $C_r \in (C_{r,\min}, C_{r,\max})$]. Therefore, the RLS algorithm with discontinuous projection is used (*Fujimoto and Yao*, 2005). The projection, shown in (3.23), is activated when the estimate moves out of the defined parameter extend. Moreover, additional conditions for parameter update are applied. In general, the accurate parameter estimation depends on the qualities of the estimator input signal. For example, if the steering angle, yaw rate, and lateral tire forces are very small (e.g., this is a situation of straight driving), the experimental data obtained is then around the zero, where the estimates will be stochastically uncertain. Therefore, in order to ensure good estimator performance, the parameters (i.e., tire cornering stiffness) is not updated when the absolute values of steering angle and yaw rate are less than certain small values.

The extend of tire cornering stiffness is defined from relationship between sensor measurements (i.e., lateral tire force sensors and sideslip angle sensor) and given by

$$
C_f \in (5000, 12500), \; C_r \in (15000, 28500). \tag{3.24}
$$

Field tests with the same driving conditions on dry asphalt and a slippery road were carried

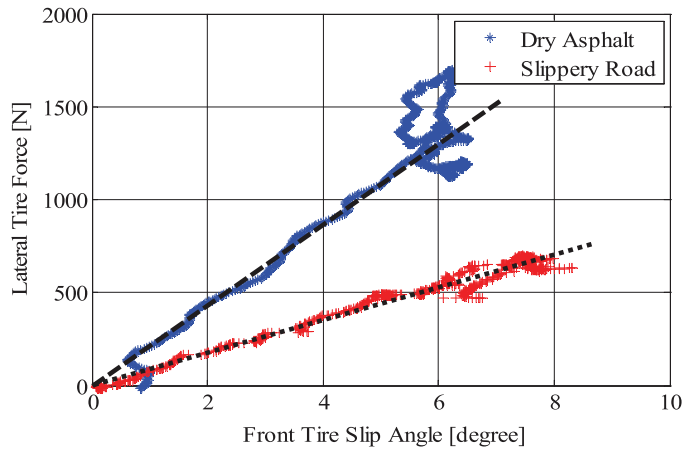

Figure 3.4: Lateral tire force measurement–tire slip angle measurement curve.

out and those results are shown in Figure 3.4. In order to acquire lateral tire forces range from small to large values, the step steering command with a slow angle rate was applied to the IWM-EV on dry asphalt and a slippery road at a constant vehicle speed. Sensor data obtained from lateral tire force sensors and sideslip angle sensors is plotted. The linear behavior between measured lateral tire force and tire slip angle shows that the lateral tire force is proportional to tire slip angle in the linear region.

3.4.2 Design of Extended Kalman Filter

In this section, a sideslip angle estimation method, which is based on the use of lateral tire force sensors, is proposed and evaluated through experimental results.

A single track vehicle model and dynamic lateral tire force model are used for observer design. The special feature in a proposed observer is that we use the estimated tire cornering stiffness as a measurable state variable. In this study, the effects of road-bank angle, vehicle roll motion, and suspension deflection are not considered. The nonlinear state space equation including random walk models for tire cornering stiffness (i.e., $\dot{C}_f = \dot{C}_r = 0$), is expressed as follows:

$$\begin{aligned} \dot{x}(t) &= f\left(x(t), u(t)\right) + \rho(t) \\ y(t) &= h(x(t)) + \sigma(t). \end{aligned} \tag{3.25}$$

The state vector x is composed of the vehicle sideslip angle, yaw rate, front lateral tire force, rear

lateral tire force, estimated front cornering stiffness, and rear cornering stiffness from (3.22)

$$x \;=\; [\beta\ \gamma\ F_f^y\ F_r^y\ C_f\ C_r]^T = [x_1\ x_2\ x_3\ x_4\ x_5\ x_6]^T, \tag{3.26}$$

The measurement vector y is composed of the yaw rate, front and rear lateral tire forces, estimated front and rear cornering stiffnesses

$$y \;=\; [\gamma\ F_f^y\ F_r^y\ C_f\ C_r]^T = [y_1\ y_2\ y_3\ y_4\ y_5]^T, \tag{3.27}$$

The input vector u is composed of the front steering angle, rear left and right driving forces

$$u \;=\; [\delta_f\ F_{rl}^x\ F_{rr}^x]^T = [u_1\ u_2\ u_3]^T, \tag{3.28}$$

where rear wheels' driving forces are obtained from driving force observers shown in Figure 4.2. It is noted that an electric vehicle, used in field tests, is a rear wheel-driving vehicle, rear wheels' driving forces are used as observer inputs.

The process and measurement noise vectors, $\rho(t)$ and $\sigma(t)$ in (3.25), are assumed to be zero mean, white, and uncorrelated. The nonlinear state evolution function $f(x(t), u(t))$ and observation function $h(x(t))$ are expressed as

$$\begin{cases} f_1(x,u) = -x_2 + \dfrac{\cos u_1}{mv_x}x_3 + \dfrac{x_4}{mv_x} \\ f_2(x,u) = \dfrac{l_f \cos u_1 x_3}{I_z} - \dfrac{l_r x_4}{I_z} - \dfrac{du_2}{2I_z} + \dfrac{du_3}{2I_z} \\ f_3(x,u) = -\dfrac{x_3}{\tau_{\mathrm{lag},f}} - \dfrac{2x_1x_5}{\tau_{\mathrm{lag},f}} - \dfrac{2l_f x_2 x_5}{\tau_{\mathrm{lag},f} v_x} + \dfrac{2x_5u_1}{\tau_{\mathrm{lag},f}} \\ f_4(x,u) = -\dfrac{x_4}{\tau_{\mathrm{lag},r}} - \dfrac{2x_1x_6}{\tau_{\mathrm{lag},r}} + \dfrac{2l_r x_2 x_6}{\tau_{\mathrm{lag},r} v_x} \\ f_5(x,u) = f_6(x,u) = 0 \end{cases} \tag{3.29}$$

$$\begin{cases} h_1(x) = x_2,\ h_2(x) = x_3,\ h_3(x) = x_4 \\ h_4(x) = x_5,\ h_5(x) = x_6. \end{cases} \tag{3.30}$$

Based on above nonlinear dynamics, the EKF is designed for sideslip angle estimation. For computer implementation, (3.25) is discretized by a Euler approximation method and has a following form

$$\begin{aligned} x_k &= f(x_{k-1}, u_k) + \rho(t) \\ y_k &= h(x_k) + \sigma(t). \end{aligned} \tag{3.31}$$

The recursive algorithm of first order EKF is summarized as follows:

3.4.2.1 Initialization

The initial estimation $\hat{x}_0$ before measurement and initial covariance P_0 are determined by

$$\hat{x}_0 = E[x_0],\ P_0 = E[(x_0 - \hat{x}_0)(x_0 - \hat{x}_0)^T] \tag{3.32}$$

3.4.2.2 Time update

In this step, the prediction of the state is carried out based on the state estimate and its covariance from previous time step, i.e.,

$$\begin{aligned} \hat{x}_{k|k-1} &= f(\hat{x}_{k-1|k-1}, u_k) \\ P_{k|k-1} &= A_k P_{k-1|k-1} A_k^T + Q_\rho \end{aligned} \tag{3.33}$$

where A_k is the process Jacobian, which is partial derivative matrix of $f(x_{k-1}, u_k)$ with respect to estimated states, and is given by

$$A_k = \frac{\partial f(\hat{x}_{k-1|k-1}, u_k)}{\partial x} \tag{3.34}$$

3.4.2.3 Measurement update

In this step, the observation vector y_k is used to correct the state estimation and the covariance estimation.

The state estimation, Kalman filter gain, and estimated covariance are given by

$$\begin{aligned} \hat{x}_{k|k} &= \hat{x}_{k|k-1} + K_k[y_k - h(\hat{x}_{k|k-1})] \\ K_k &= P_{k|k-1}H_k^T[H_kP_{k|k-1}H_k^T + R_\sigma]^{-1} \\ P_{k|k} &= [I - K_kH_k]P_{k|k-1} \end{aligned} \tag{3.35}$$

where H_k is the measurement Jacobian at kth step of nonlinear equation with respect to estimated states, and is given by

$$H_k = \frac{\partial h(\hat{x}_{k|k-1})}{\partial x}. \tag{3.36}$$

In selection of noise covariance matrices (i.e., Q_ρ and R_σ), a diagonal matrix (i.e., individual noise components are not cross-correlated) is chosen and the covariance matrices of process noise and measurement noise are given as follows:

$$Q_\rho = \text{diag}[Q_\beta, Q_\gamma, Q_{F_f^y}, Q_{F_r^y}, Q_{C_f}, Q_{C_r}] \tag{3.37}$$

$$R_\sigma = \text{diag}[R_\gamma, R_{F_f^y}, R_{F_r^y}, R_{C_f}, R_{C_r}]. \tag{3.38}$$

In covariance matrix setting, it should be noted that the less noise in sensor measurements compared to the uncertainty in dynamics model, the more the states will be adapted to follow sensor measurements. The states (e.g., sideslip angle and yaw rate) are modeled using reliable vehicle dynamics. Therefore, the process noises are relatively small. The suitable process noise variances for lateral tire force models are selected based on comparison to the corresponding measurement noise variances. In case of tire cornering stiffness, new values are much more accurate than the prior states and thereby we put the relatively high process uncertainty on it.

3.4.3 Experimental Verification

The proposed sideslip angle observer was evaluated through field tests. The experimental tests have been done on dry asphalt and wet asphalt which show normally a high-μ value and a low-μ value, respectively. A pulse steering command is applied to obtain large lateral acceleration (i.e., up to 6 m/s^2). It means that the IWM-EV was put in a critical driving condition. Figure

3.5 shows results of a field test carried out on wet asphalt at $v_x = 50$ km/h. Figure 3.5(a) shows driving conditions including steering angle command, lateral acceleration, and yaw rate. According to Figure 3.5(b), the proposed observer shows better estimation performance compared with results of a kinematics-based method (The kinematics-based method was proposed by authors and for further details, see Appendix B and *Nam et al.* (2012b)) and a fixed KF method. From Figure 3.5(c), we can see that tire cornering stiffness on wet asphalt is much smaller than that on dry asphalt. Therefore, an experimental result of the fixed KF (i.e., this method uses fixed tire cornering stiffness for a value on dry asphalt), shown in Figure 3.5(b), shows a relatively large estimation error. Figure 3.6 represents results of a field test on dry asphalt at $v_x = 55$ km/h. According to Figure 3.6(b), the proposed observer is relatively good with respect to sensor measurements. Even though there is a small estimation error, this method provides more accurate estimation compared to existing methods. Figure 3.5(c) and Figure 3.6(c) represent the estimation results of tire cornering stiffness obtained from field tests on wet asphalt and dry asphalt, respectively. It can be seen that estimates converge rapidly to final values which are considered as true tire cornering stiffnesses on each road.

In addition, in order to verify the estimation ability of the proposed observer under more severe driving conditions, we have performed the experiments in a critical driving situation. As shown in Figure 3.7(a), the large vehicle lateral acceleration (i.e., absolute value is up to 7 m/s^2) is obtained. This indicates that the tires begin to saturate and reach a peak value; This area is commonly called the nonlinear tire region. The measurements of the yaw rate and steering angle are also shown in Figure 3.7(a). Figure 3.7(b) represents the results of the proposed observer and other methods. If we compare the two observers, i.e., KF with fixed C_f and C_r and EKF, we can confirm that the proposed EKF is more efficient and robust against tire-road conditions. Estimation error shown in the result of KF with fixed C_f and C_r is mainly due to the model mismatch caused by varying tire cornering stiffness. On the other hand, the proposed EKF shows the significantly small estimation error by using estimated tire cornering stiffness. Tire cornering stiffness estimated from a RLS algorithm is shown in Figure 3.7(c). Since this experiment was performed on wet asphalt, the results of Figure 3.7(c) is very similar to the results of Figure 3.5(c).

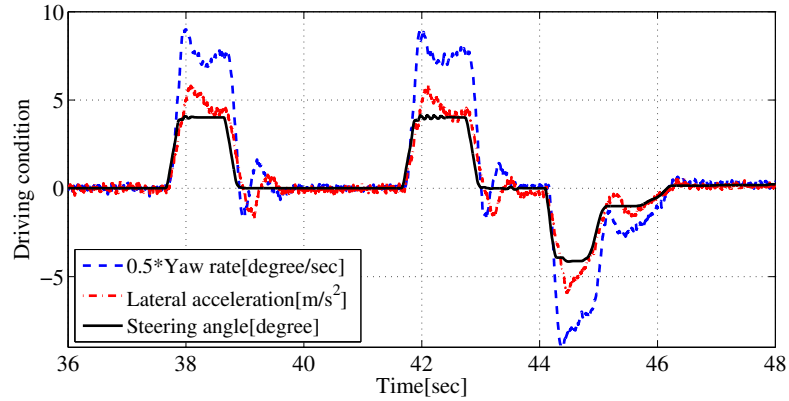

(a)

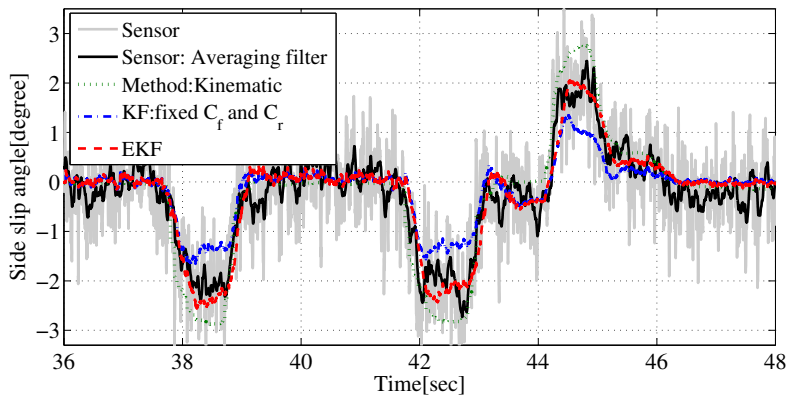

(b)

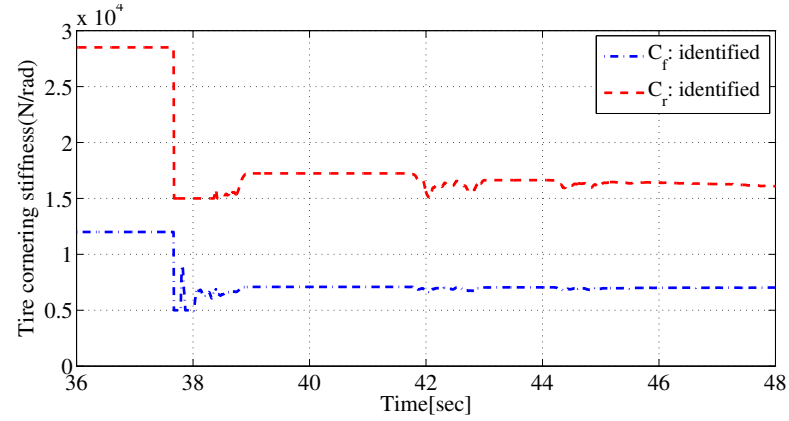

(c)

Figure 3.5: Estimation result on wet asphalt at $v_x = 50$ km/h. (a) Driving condition. (b) Sideslip angle. (c) Tire cornering stiffness.

The estimation error for each method is calculated, i.e., estimation error = sensor measurement − estimate, and its values for three methods are plotted as shown in Figure 3.8. Figure 3.8(a)–(c) are obtained from the results of Figure 3.5–3.7, respectively. It is shown that the

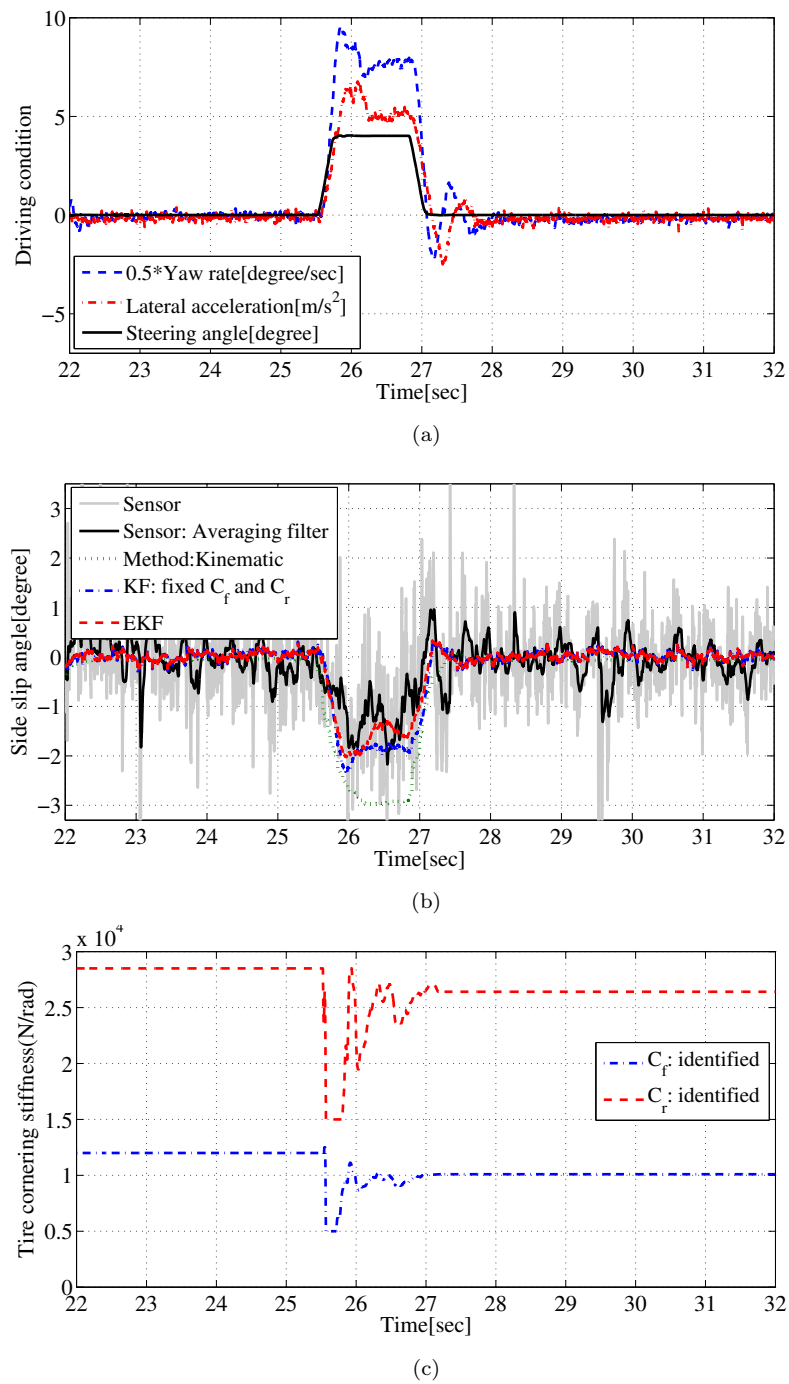

Figure 3.6: Estimation result on dry asphalt at $v_x = 55$ km/h. (a) Driving condition. (b) Sideslip angle. (c) Tire cornering stiffness.

estimation error for the proposed EKF is the smallest regardless of road conditions. Especially, if we see the Figure 3.8(c), we can confirm that the estimate from the proposed EKF well follows the real sideslip angle value even in the critical driving situation. By utilizing the lateral

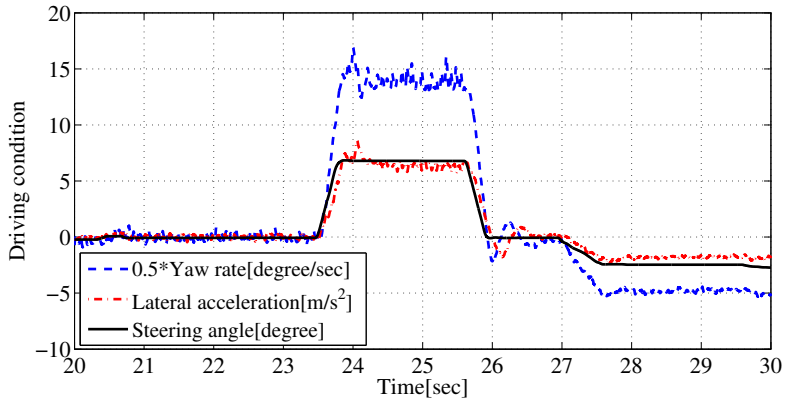

(a)

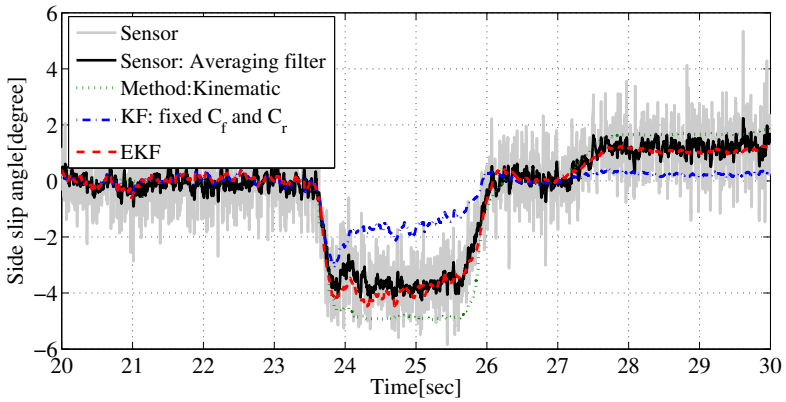

(b)

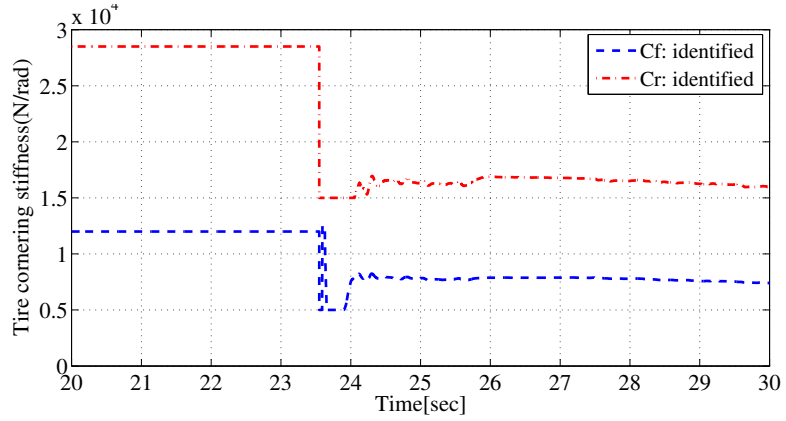

(c)

Figure 3.7: Estimation result of critical driving (e.g., $|a_y| \simeq 7$ m/s^2) on wet asphalt at $v_x = 60$ km/h. (a) Driving condition. (b) Sideslip angle. (c) Tire cornering stiffness.

tire force sensors, more accurate and reliable state estimation could be realized without using expensive sideslip angle sensors. Moreover, feasibility of practical application of the lateral tire force sensors to vehicle control systems is verified through experimental results. This is one of

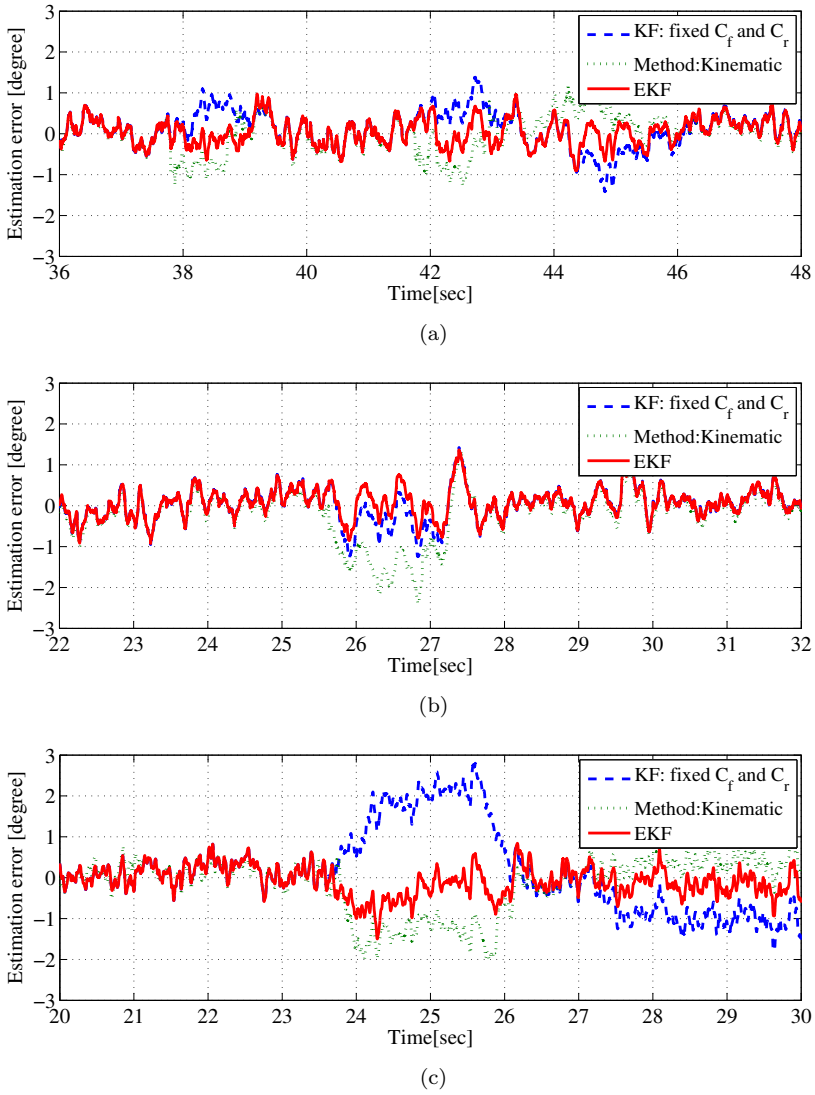

Figure 3.8: Estimation error (i.e., the estimation error is defined as a value of estimate–sensor measurement). (a) Result on wet asphalt. (b) Result on dry asphalt. (c) Result of critical driving on wet asphalt.

the important contributions of this study.

3.4.4 Discussion on Observer Robustness

Vehicle parameters, such as vehicle mass, yaw moment of inertia, and distance of CG, vary frequently according to driving conditions. For example, when comparing a vehicle occupied only by the driver with a vehicle occupied by a driver, passengers, and additional luggage, then the total vehicle weight could easily vary by several hundred kilograms. To study the robustness of a

Table 3.1: Estimation error with respect to varying vehicle mass.

	(A)	(B)	(C)	(D)	(E)	(F)	(G)
Vehicle mass	m-20%	m-10%	m-5%	m	m+5%	m+10%	m+20%
Estimation Error (°)	0.584	0.458	0.405	0.398	0.427	0.518	0.758
Estimation Error (%)	14.6	11.45	10.13	9.95	10.68	12.95	18.95

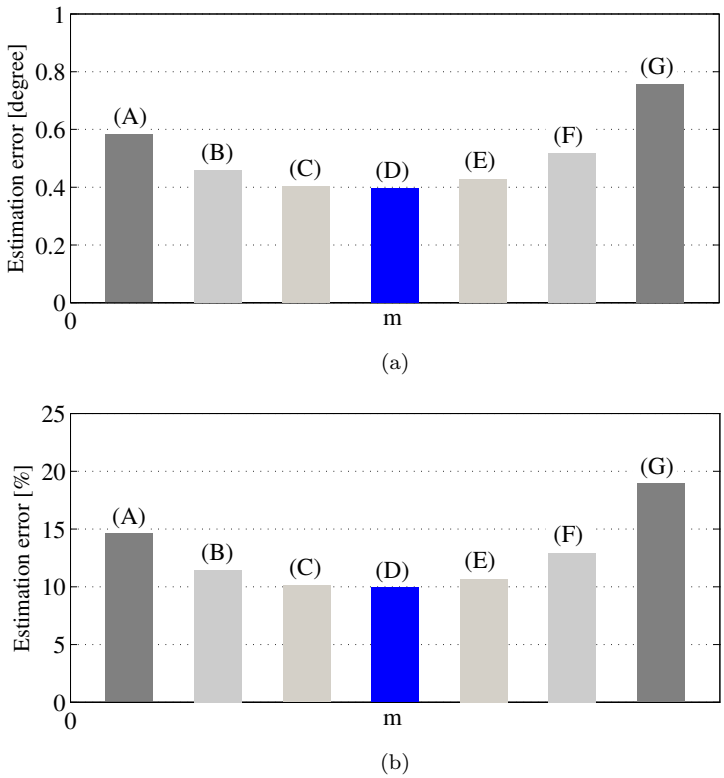

Figure 3.9: Observer performance via vehicle mass change (i.e., m: -20 %∼+20 %). (a) Absolute value of estimation error, i.e., $|\hat{\beta} - \beta_{\text{sensor}}|$. (b) Normalized estimation error $\tilde{\mathbf{e}}$.

proposed EKF with respect to the weight change, we vary the weight m between -20 % and +20 % around the nominal value, i.e., $m = 875$ kg. Table 3.1 shows that a proposed EKF is affected by the mass variations. It is confirmed that the normalized estimation errors, shown in Figure 3.9, increase when increasing the mass variations. Since the dynamic equations, which describe the vehicle motion, introduces directly the vehicle mass. Moreover, errors in the weight transfer by mass change induces significant errors in the vertical tire forces, which in turns affect considerably

the lateral tire force forces. Although the estimation error with respect to varying vehicle mass increases, a proposed EKF still provide more accurate estimation than other estimation methods.

The normalized estimation error $\tilde{\mathbf{e}}$ is calculated by

$$\tilde{\mathbf{e}} = \frac{|\hat{\beta} - \beta_{\text{sensor}}|}{|\hat{\beta}|} \times 100(\%) \qquad \text{Normalized estimation error} \tag{3.39}$$

3.5 Evaluation of Proposed Sideslip Angle Estimation Methods

Two real-time algorithms for estimating vehicle sideslip angle, using lateral tire force sensors, are presented in previous section: one is a kinematics-based algorithm (**proposed method I** in Table 3.2), the other is an EKF algorithm (**proposed method II** in Table 3.2).

Table 3.2 summarizes two proposed estimation methods. To overcome existing challenging problem with robust sideslip angle estimation, lateral tire force measurements from MSHub are utilized with novel approaches.

Table 3.2: Summary of proposed estimation methods.

	Proposed method I	**Proposed method II**
Features	▪ Vehicle model free ▪ Sensor kinematics ▪ Linear lateral tire model ▪ ESC sensors + MSHub ▪ Recursive least square algorithm	▪ Bicycle model ▪ Dynamic linear lateral tire model ▪ Update of tire-road condition ▪ ESC sensors + MSHub ▪ Extended Kalman filtering
Advantages	▪ Robust against tire-road conditions ▪ Simple estimation algorithm ▪ Easily implementable in real-time	▪ Robust against tire-road conditions ▪ Nonlinear tire force characteristics is partly handled by using MSHub ▪ Provide more accurate estimation even when tire forces are saturated
Limitation	▪ Estimation error increases when tires begin to saturate ▪ Sensitive to weight transfer	▪ Relatively complex estimation algorithm ▪ Estimation accuracy can be improved by using nonlinear tire model
Nonlinearities	▪ Tire-Road parameters are varying ····· Tire-Road condition adaptation ▪ Tire force saturation ····· Sensor measurement : MSHub ▪ Weight transfer effects to vehicle parameters ····· Weight transfer compensation	

(ESC sensors: Yaw rate, Lateral acceleration and Steering angle sensors)

3.6 Vehicle Roll Angle Estimation

In this section, a roll angle estimation method using lateral tire force sensors is presented and its effectiveness is verified by field tests with various test conditions.

3.6.1 Literature Review on Roll Angle Estimation

Vehicle roll motion generally occurs as a result of lateral motion by steering maneuvers or road disturbances. Over the last few years, several estimation methods were proposed to estimate roll states based on vehicle dynamics models without using additional sensors (e.g., roll rate sensor) (*Hac et al.*, 2004; *J.I Park and Yi*, 2008; *Yi et al.*, 2007; *Rajamani et al.*, 2011b). In *Hac et al.* (2004), several methods for roll angle estimation were discussed based on advantages and drawbacks of each method. Moreover, an approach using closed loop adaptive observer for roll angle and roll rate estimation was proposed and evaluated. In *J.I Park and Yi* (2008), a road-disturbance decoupled roll state estimator was designed, by combining the lateral model-based estimation method and vertical model-based estimation method, and evaluated by computer simulations. In other approaches (*Ryu and Gerdes*, 2004; *Bevly et al.*, 2006), GPS with two laterally placed GPS antennas was used to estimate roll angle. GPS-based estimation approaches require satellite visibility from any location. However, the satellite visibility may be lost periodically in urban and forested driving environments and it causes inaccurate estimation. Even though GPS provides relatively accurate roll angle estimates under limited driving environments, it has a difficulty in vehicle applications due to the additional sensor cost.

In contrast to conventional engine vehicles, IWM-EV have a low ratio of sprung mass over unsprung mass due to having in-wheel motors installed in each wheel. This implies that ride quality can be deteriorated. In order to avoid deterioration in ride quality, the suspension stiffness was selected as a smaller value. It indicates that the roll motion easily occurs. Thus, a roll stability control system is required and accurate roll angle estimation must be obtained before control design. In this section, a roll angle estimation method, which uses sensor kinematic relationships and a linear roll model, is introduced. In a proposed roll angle estimator, lateral tire forces which are measured by MSHub units are utilized to estimate roll angle for the first time.

3.6.2 Vehicle Roll Dynamic Model

This section introduces roll dynamics for KF design. Figure 3.10 shows the two-dimensional roll dynamics for electric vehicles with in-wheel motors. In order to model the roll dynamics, the following assumptions are made:

1. The location of the roll axis is constant with height h_{RC} and the lateral and vertical movements of RC due to the asymmetric suspension geometry are not considered.
2. Since roll angle is small, $\sin\phi \approx \phi$ and $\cos\phi \approx 1$.
3. Pitching and bouncing motion of sprung mass are neglected.
4. The effect of the road bank angle is not considered in this study.

The two-dimensional roll dynamic equation (*Ryu and Gerdes*, 2004; *Kawashima et al.*, 2010), the kinematic relationships of the lateral acceleration of CG, a_y, and sensor measurement, a_{ym}, are expressed as

$$\begin{aligned} I_x\ddot{\phi} + C_{\mathrm{roll}}\dot{\phi} + K_{\mathrm{roll}}\phi &= m_s(a_{ym})h_{\mathrm{roll}} \\ &= m_s(a_y + g\phi)h_{\mathrm{roll}} \qquad (3.40) \\ a_y &= \dot{v_y} + \gamma v_x \qquad (3.41) \\ a_{ym} &= \dot{v_y} + \gamma v_x + g\phi \qquad (3.42) \end{aligned}$$

In (3.40), a roll moment acting on the sprung mass, which is caused by lateral motion, can be explained by lateral inertial force and gravity force of the sprung mass. The lateral acceleration effect in roll moment generation can be equivalently explained by lateral tire forces applied on tires, and the equivalent equation using lateral tire forces can be derived from the roll moment balance equation with respect to point RC as seen in Figure 3.10.

$$\sum M_x = m_s(a_y + g\phi)h_{\mathrm{roll}} = F^y_{\mathrm{eq}}h_{\mathrm{RC}}. \qquad (3.43)$$

Here, F^y_{eq} is the equivalent lateral tire force causing roll motion, which corresponds to roll motion caused by lateral acceleration of sprung mass. In (3.43), F^y_{eq} is replaced by lateral tire forces

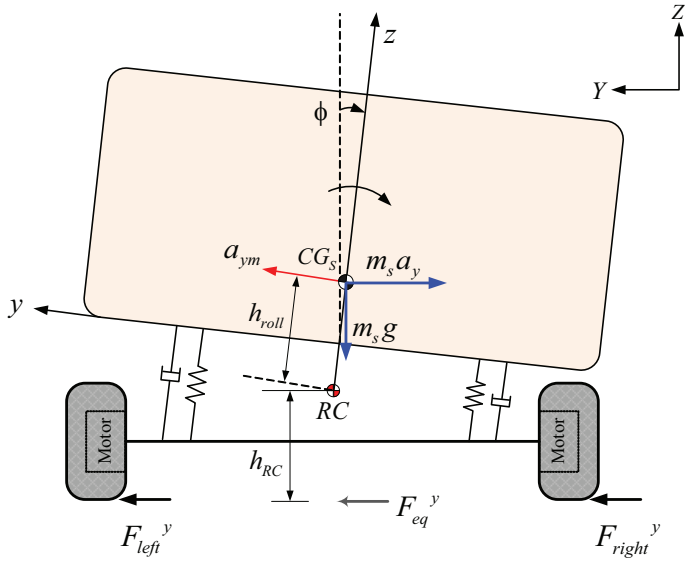

Figure 3.10: 2–dimensional roll dynamics for an electric vehicle.

measured from the MSHub units, installed in each wheel. Therefore, an external roll moment acting on the sprung mass can be represented by lateral tire forces.

$$F_{\text{eq}}^{y} h_{\text{RC}} \approx (F_{\text{left}}^{y} + F_{\text{right}}^{y}) h_{\text{RC}} = \sum_{i=1}^{4} (F_i^y) h_{\text{RC}}. \tag{3.44}$$

Combining (3.40) and (3.44), and using lateral tire forces as an external input, the following roll dynamics is obtained.

$$I_x \ddot{\phi} + C_{\text{roll}} \dot{\phi} + K_{\text{roll}} \phi = \sum_{i=1}^{4} (F_i^y) h_{\text{RC}}. \tag{3.45}$$

In contrast to conventional roll model-based estimation methods, the proposed roll angle estimation method uses lateral tire forces as inputs. Therefore, the effects of nonlinear tire characteristics (e.g., tire deflection by load transfer) can be considered in roll dynamics by directly using measured lateral tire forces. In this study, two KF are designed–one that uses lateral tire force measurements ("Fy-based method"), and one that uses lateral acceleration measurements ("Ay-based method"). Since the MSHub units are superior to the lateral acceleration sensor in response time, it is expected that estimations based on lateral tire force measurements will lead that of estimations based on lateral acceleration measurements. Since the main source of lateral

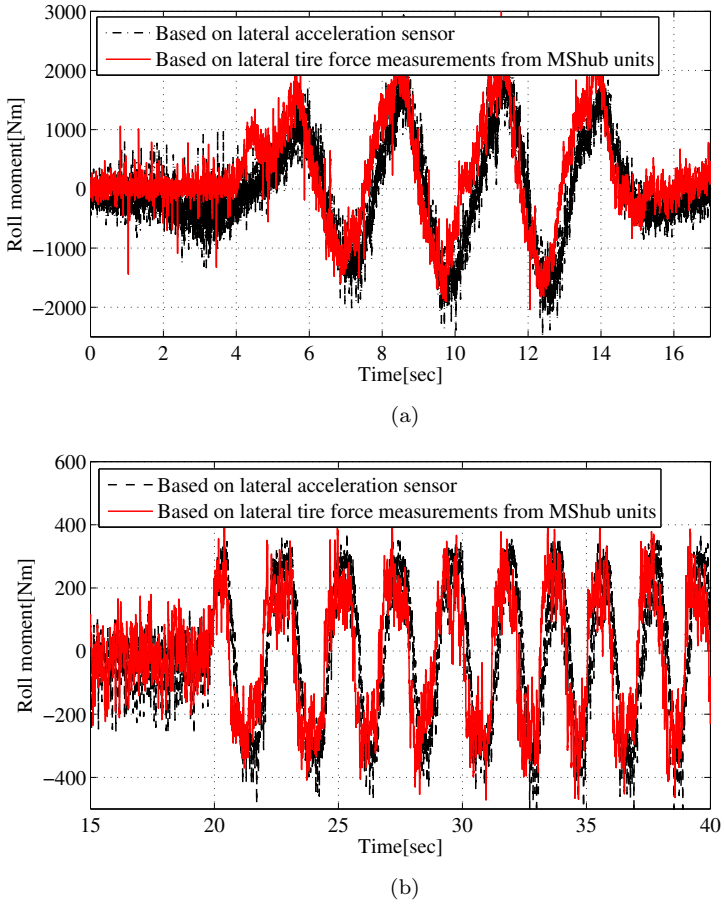

Figure 3.11: Roll moment induced by the lateral vehicle motion. (a) Driving on dry asphalt ($\mu \simeq 0.9$). (b) Driving on a slippery road ($\mu \simeq 0.3$).

dynamic motion is the lateral tire force induced by driver's steering actions, the measured lateral tire forces can provide accurate estimation of vehicle states.

In order to check the response characteristics of two sensors (i.e., a lateral acceleration sensor and a MSHub unit), the roll moments, described in (3.45), were calculated from experiment data obtained in field tests on dry asphalt and a slippery road, respectively. From field test data, it is founded that the response time difference between a MSHub unit and a lateral acceleration sensor ranges from 80 msec to 200 msec. Figure 3.11 shows the roll moments calculated from (3.45). As shown in Figure 3.11, the roll moment calculated from lateral acceleration measurements has phase lag compared with the calculated roll moment from lateral tire force measurements.

3.6.3 Roll Angle Estimation Algorithm

In this section, vehicle states are estimated using available sensor measurements and roll dynamics. The KF was applied to estimate unknown states (e.g., roll angle and roll rate) and to smoothen sensor measurement noise. An overall structure of the proposed state estimator is shown in Figure 3.12.

The process of roll angle estimation can be divided into two stages: first, the preliminary estimation of a lateral vehicle velocity is conducted using the sensor measurements; second, this preliminary estimate (i.e., pseudo-measurement) and available sensor measurements are used in KF design for roll angle estimation. The estimated v_y from (3.11) is considered as a measurement variable, called a pseudo-measurement $\tilde{v}_y$, and thereby (28) can be rewritten as follows:

$$\dot{\tilde{v}}_y = a_{ym} - \gamma v_x - g\phi \tag{3.46}$$

From (2.24), (3.45), and (3.46), the state space equations for KF design are obtained as

$$\begin{aligned} \dot{x} &= Ax + Bu + w \\ y &= Cx + v \end{aligned} \tag{3.47}$$

where state variables, inputs, and measurement outputs are defined as

$$x = [\ \tilde{v}_y \quad \gamma \quad \phi \quad \dot{\phi} \quad F_f^y \quad F_r^y\ ]^T, \quad u = [\ a_{ym} \quad M_z\ ]^T,\ y = [\ \tilde{v}_y \quad \gamma \quad F_f^y \quad F_r^y\ ]^T,$$

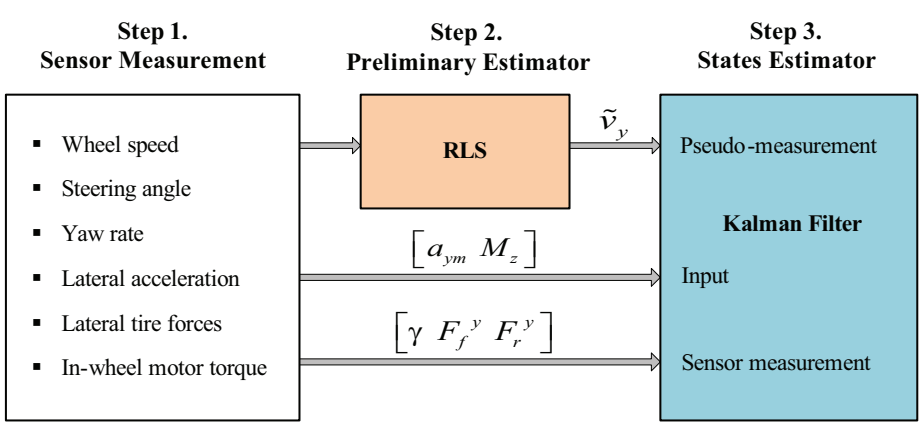

Figure 3.12: Schematic of the roll states estimator.

and A, B, and C are as follows:

$$A = \begin{bmatrix} 0 & -v_x & -g & 0 & 0 & 0 \\ 0 & 0 & 0 & 0 & \frac{l_f}{I_z} & \frac{-l_r}{I_z} \\ 0 & 0 & 0 & 1 & 0 & 0 \\ 0 & 0 & -\frac{K_{\text{roll}}}{I_x} & -\frac{C_{\text{roll}}}{I_x} & \frac{h_{\text{RC}}}{I_x} & \frac{h_{\text{RC}}}{I_x} \\ 0 & 0 & 0 & 0 & 0 & 0 \\ 0 & 0 & 0 & 0 & 0 & 0 \end{bmatrix}, \quad B = \begin{bmatrix} 1 & 0 \\ 0 & \frac{1}{I_z} \\ 0 & 0 \\ 0 & 0 \\ 0 & 0 \\ 0 & 0 \end{bmatrix},$$

and

$$C = \begin{bmatrix} 1 & 0 & 0 & 0 & 0 & 0 \\ 0 & 1 & 0 & 0 & 0 & 0 \\ 0 & 0 & 0 & 0 & 1 & 0 \\ 0 & 0 & 0 & 0 & 0 & 1 \end{bmatrix}.$$

Note that the system described by (3.47) could be completely observable by using $\tilde{v}_y$ in (3.46) as a sensor measurement. Observability, which is concerned with the problem of determining the states of a dynamics system from observations of the output and control vectors, is examined through a rank condition on the Kalman observability matrix. By using pseudo-measurement $\tilde{v}_y$, (A, C) is observable (which means that observability matrix has full rank).

For real-time implementation, (3.47) is discretized as follows:

$$\begin{aligned} x[k+1] &= G[k]x[k] + H[k]u[k] + w[k] \\ y[k] &= C[k]x[k] + v[k] \end{aligned} \tag{3.48}$$

where

$$\begin{aligned} G[k] &= e^{AT_s}, \quad H[k] = \int_0^{T_s} e^{A\tau} B d_\tau \\ C[k] &= C, \quad T_s : \text{Sampling time.} \end{aligned}$$

Here, $w[k]$ and $v[k]$ are the process noise and measurement noise, k is the time step. It is assumed

that the process and measurement noise are zero-mean Gaussian processes, and the covariance matrices are given as follows:

$$Q_w = E(w[k]w[k]^T) > 0 \tag{3.49}$$

$$R_v = E(v[k]v[k]^T) \gg 0 \tag{3.50}$$

$$E(w[k]v[k]^T) = 0. \tag{3.51}$$

The KF bandwidth and its susceptibility to sensor measurement noise totally depend on the process noise covariance matrix Q_w and the measurement noise covariance matrix R_v, which represent level of confidence placed in the accuracy of the observer model and sensor measurements. These matrices determine the filter characteristics including accuracy and response, and their matrix values were experimentally determined by using sensor measurements. The covariance matrices of process noise and measurement noise are given as follows:

$$Q_w = \text{diag}[Q_{\tilde{v}_y}, Q_\gamma, Q_\phi, Q_{\dot{\phi}}, Q_{F_f^y}, Q_{F_r^y}] \tag{3.52}$$

$$R_v = \text{diag}[R_{\tilde{v}_y}, R_\gamma, R_{F_f^y}, R_{F_r^y}]. \tag{3.53}$$

In principle, the covariance matrices are not necessarily diagonal. However, treating the noise covariance matrix as a diagonal matrix (i.e., individual noise components are not cross-correlated) is advantageous since it reduces computation time (*Gelb*, 1974). In selection of covariance matrices, it should be noted that the less noise in sensor measurements compared to the uncertainty in dynamics model, the more the states will be adapted to follow sensor measurements. Since the new measurements for lateral tire forces is much more accurate than the prior estimates, we put the high uncertainty on states (i.e., lateral tire forces). The states (e.g., roll angle and roll rate) are modeled using reliable vehicle roll dynamics. Therefore, the process noises are relatively small. The suitable process noise variances for other states (e.g., lateral vehicle velocity and yaw rate) are selected based on comparison to the corresponding measurement noise variances. The noise variances of three sensor measurements are determined from statistical data analysis (e.g., a statistical evaluation of the histogram) using Matlab software.

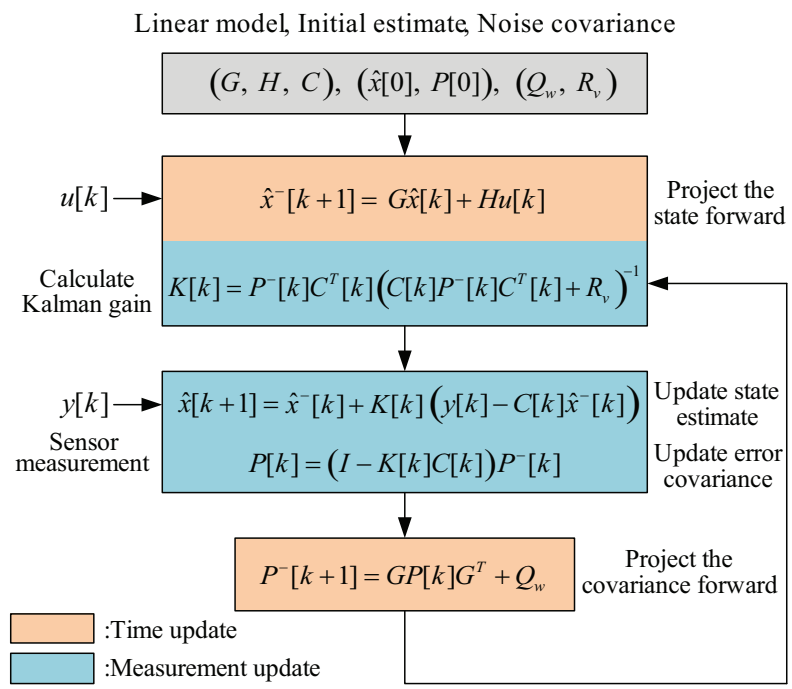

Figure 3.13: Recursive structure of the KF algorithm.

The KF, designed based on (3.47)–(3.53), performs filtering and prediction (*Gelb*, 1974). The basic steps of computational procedure for the KF are illustrated in Figure 3.13.

3.6.4 Experimental Verification

The proposed estimation method was implemented on the experimental electric vehicle shown in Figure 2.16. To evaluate estimation results of the KF, the vertical potentiometers and a roll rate sensor (i.e., gyro sensor) were used to accurately measure the roll angle and roll rate, respectively. The random steering test and pulse steering test on dry asphalt were conducted and field tests on wet asphalt and a slippery road were also carried out to verify the robustness against road conditions.

Experimental results obtained from field tests are presented to validate the estimator and to compare the Fy- and Ay-based method. Figure 3.14 shows experimental results for the random steering test on dry asphalt. Driving conditions including vehicle speed and steering angle (i.e., wheel angle) are illustrated in Figure 3.14. Figure 3.14(b) and (c) present estimates of roll angle and roll rate compared with sensor measurements. It is confirmed that the estimated roll

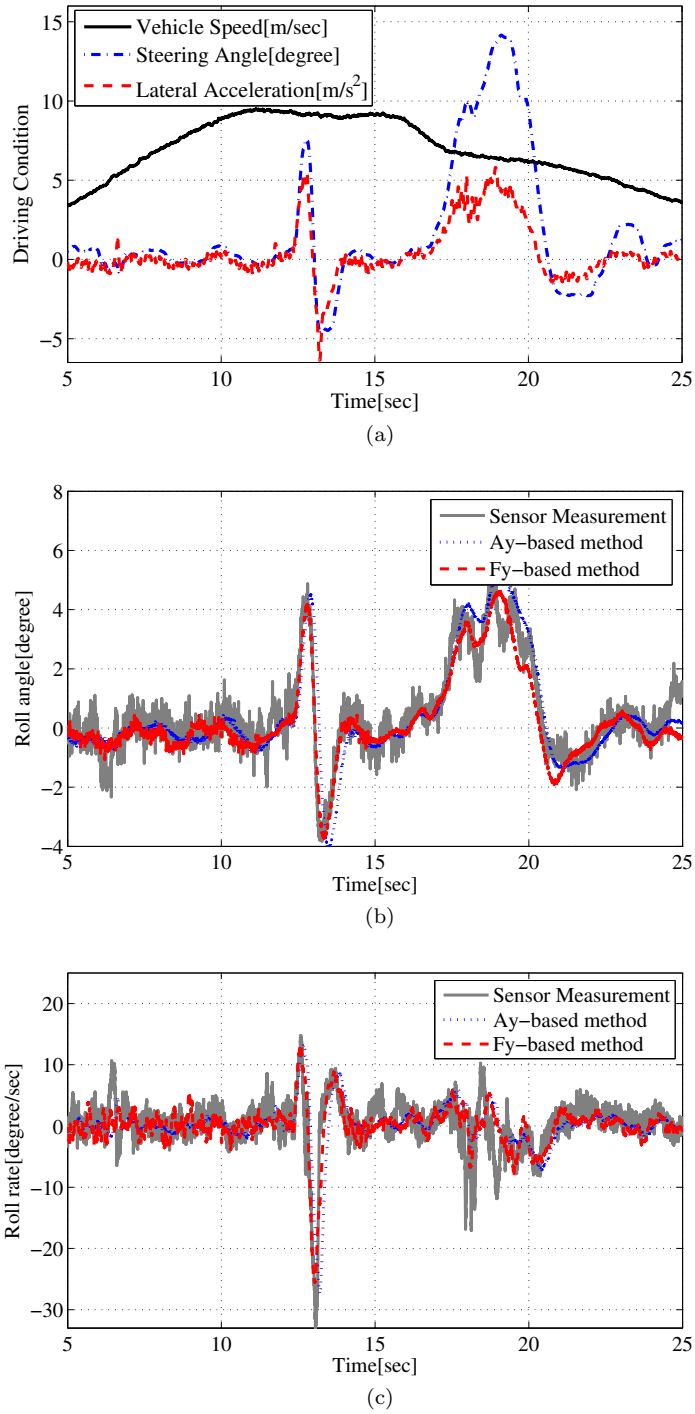

Figure 3.14: Experimental results for roll state estimation in a random steering test on dry asphalt (i.e., $\mu \simeq 0.9$). (a) Driving condition. (b) Roll angle. (c) Roll rate.

angle and roll rate track the sensor measurement values with small errors. Experimental results obtained from the Fy- and Ay-based methods are compared using Figure 3.14(b) and (c). We

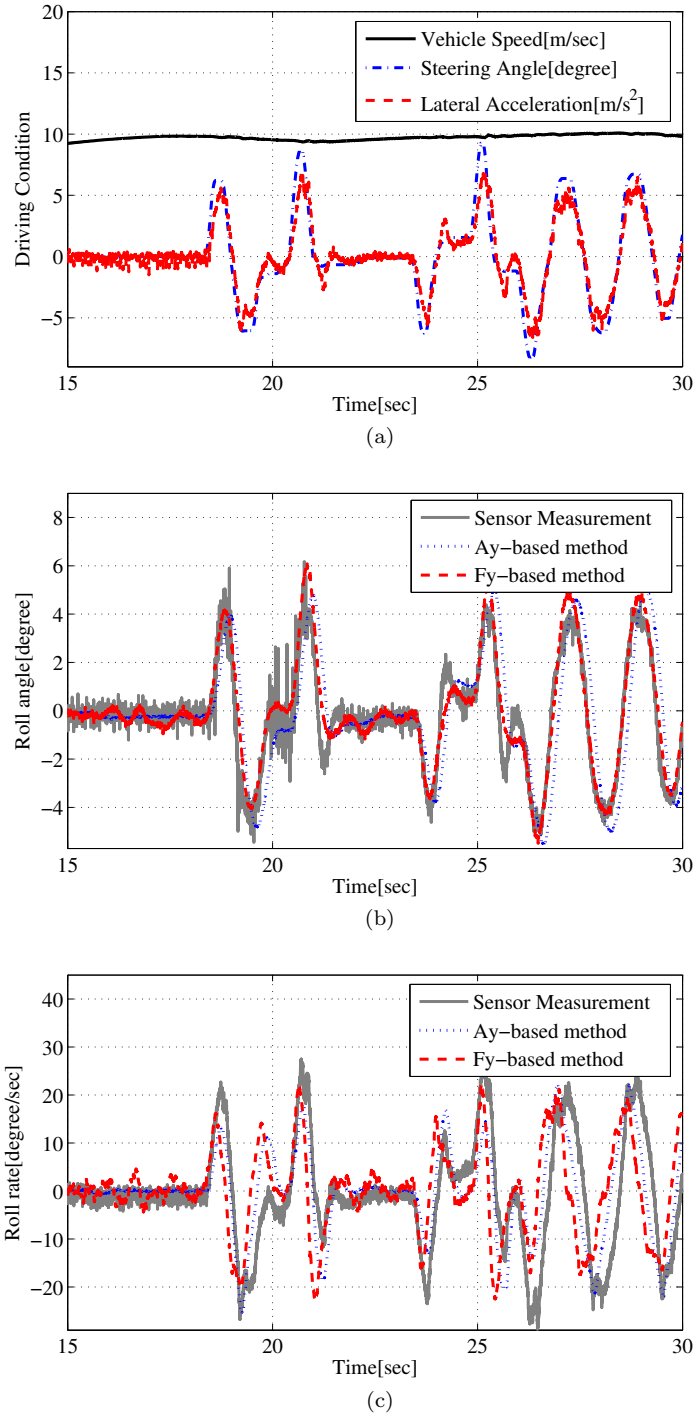

Figure 3.15: Experimental results for roll state estimation in a random steering test on wet asphalt (i.e., $\mu \simeq 0.7$). (a) Driving condition. (b) Roll angle. (c) Roll rate.

can confirm that the Fy-based method shows more accurate results without noticeable phase lag. This agrees with earlier discussion about response characteristics of roll moments, which

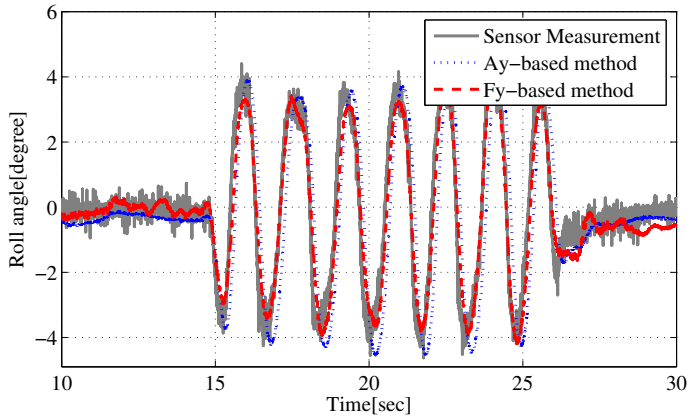

(a)

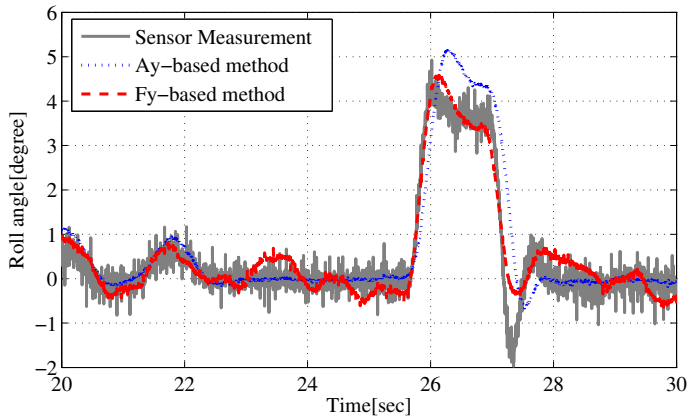

(b)

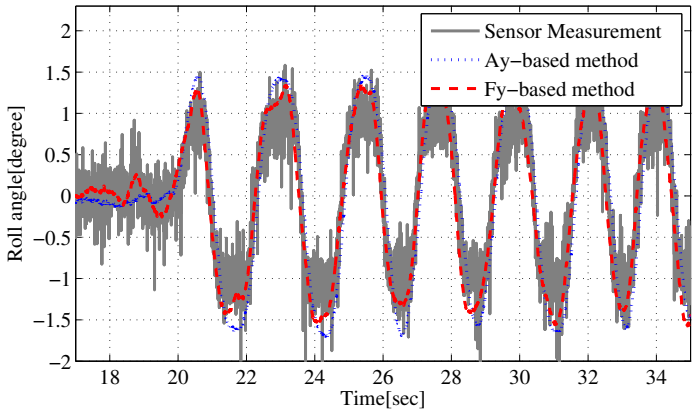

(c)

Figure 3.16: Experimental results for roll angle estimation. (a) Driving at $v_x = 50$ km/h on dry asphalt (i.e., $\mu \simeq 0.9$). (b) Driving at $v_x = 40$ km/h on wet asphalt (i.e., $\mu \simeq 0.7$). (c) Driving at $v_x = 30$ km/h on a slippery road (i.e., $\mu \simeq 0.3$).

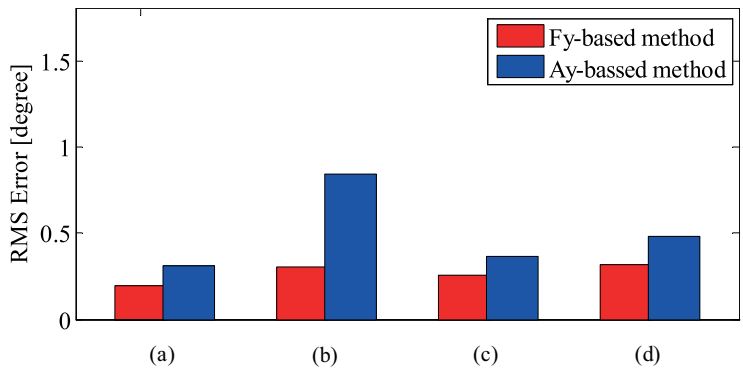

Figure 3.17: Calculated RMS errors for estimation.

are calculated from lateral tire forces and lateral acceleration respectively. Figure 3.15 shows experimental results of the random steering test at $v_x = 40$ km/h on wet asphalt. Similarly, the proposed KF in this case provides accurate estimation with no phase lag.

To verify the robustness of the proposed KF, several field tests on different roads were performed and those results are shown in Figure 3.16.

The RMS values of estimation errors are shown in Figure 3.17. The experimental results shown in Figure 3.16(a), (b), and (c) correspond to (a), (c), and (d) in Figure 3.17, and are explained as follows: (a) shows the result of a sine steering test at $v_x = 50$ km/h on dry asphalt. As shown in Figure 3.17, the roll angle estimated by the KF using lateral tire forces shows relatively low RMS values (in this case, the maximum roll angle is $|\phi|_{\max} \approx 4$ degree). (c) shows the result of sine steering and pulse steering tests at $v_x = 40$ km/h on wet asphalt respectively. Roll angles estimated with the proposed KF track the measured values with small errors. It is noted that result (d), obtained from the field test on a slippery road, also shows the low RMS value. This implies that the proposed KF is robust to road conditions.

3.7 Chapter Summary

This chapter presents novel estimation methods to accurately estimate the vehicle sideslip angle and roll angle using lateral tire force sensors. The RLS algorithm and an KF were used in estimator design. Characteristics of the proposed estimation methods, such as estimation performance and robustness, were discussed and evaluated through field tests under different road conditions. In addition, a nonlinear state observer which is derived from EKF techniques

is designed and its estimation ability is verified through experiments on an IWM-EV. Comparison with sideslip angle, measured from the Correvit sensor, demonstrates the robustness and accuracy of a proposed observer. It was shown that the estimation methods utilizing lateral tire forces provide even more improved estimation of the vehicle sideslip angle and roll angle. Additionally, the experimental results demonstrated that KF design using lateral tire forces could provide reliable estimation without noticeable phase lag. By using lateral tire force measurements, important vehicle states for vehicle stability control could be estimated without using expensive sensors and we could confirm the possibilities of the practical applications of MSHub units to vehicle stability control systems for an IWM-EV. From experimental results of proposed estimators, it is anticipated that lateral tire forces, measured from MSHub units, will provide practical solutions to challenging issues in vehicle state estimation. Since the proposed estimator for sideslip angle estimation is designed based on linear tire models, some estimation errors may occur during severe driving on low friction roads. Therefore, in future works, we will improve the tire model by taking into account nonlinear tire characteristics, an effect of road-bank angle, and coupling effects between yaw and roll motions.

CHAPTER IV

Tire-Road Condition Estimation

4.1 Introduction

Vehicle motion control systems (e.g., active safety control systems) contribute to stabilizing the vehicle by properly controlling tire forces. These control systems work well only when the tire force command, which is generated by motion controller (e.g., yaw rate or sideslip angle controller etc.), is within the tire-road friction limit. Therefore, real-time information on tire-road condition (i.e., tire force limit) is significantly important to enhance control performances (*Hahn et al.*, 2002; *Lee et al.*, 2004; *Li et al.*, 2006; *Rajamani et al.*, 2010; *Villagra et al.*, 2011; *Rajamani et al.*, 2011a; *Erdogan et al.*, 2011; *Ahn et al.*, 2011). In *Li et al.* (2006), different types of longitudinal, lateral, and integrated tire-road friction model have been examined and a

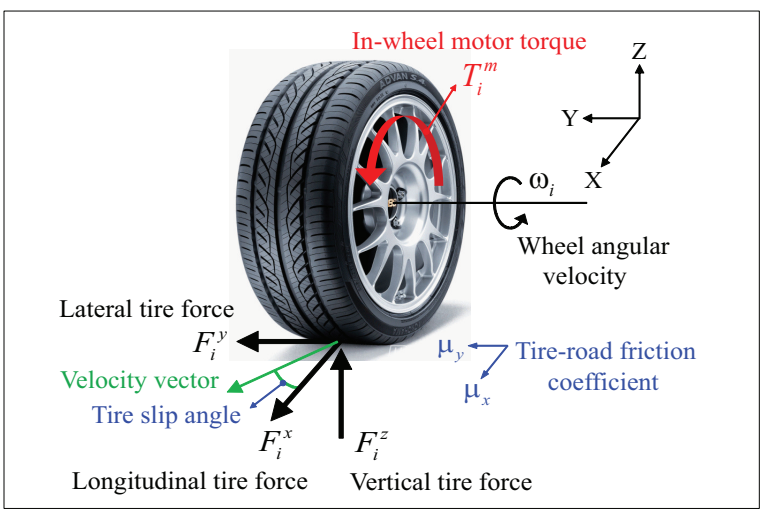

Figure 4.1: Tire forces and wheel dynamic variables.

general scheme of the tire-road friction monitor is presented. Individual wheel friction coefficient estimation algorithms have been proposed and experimental results demonstrated that friction coefficients at the individual wheels and road gradient can both be estimated quite reliably (*Rajamani et al.*, 2011a). In *Erdogan et al.* (2011), the estimation method of tire-road friction coefficient, based on the lateral carcass deflection measurements using a wireless piezoelectric tire sensor which is a special sensor designed to to remove the effects of the vertical and tangential tire deflections on the lateral tire deflection measurements, has been proposed. However, since this is not a cost-effective system and has a technical problems with sensor installation, it is not suitable for vehicle applications.

In this chapter, a real-time algorithm for estimating instantaneous lateral tire force limit is designed based on lateral vehicle dynamics and lateral tire force sensors. The performance of the estimation algorithm is verified using test data.

4.2 Tire Force Estimation and Measurement

In this section, the estimation methods and measurements of tire forces are presented. Tire forces caused by tire-road interaction are the most dominant factor in deciding the vehicle motions because they are only forces that a vehicle experiences from the road as sown in Figure 4.1. These tire forces significantly affect the longitudinal, lateral, yaw, and roll motions of the vehicle. Therefore, if we can estimate or measure the these forces, the vehicle motion can be predicted and thereby optimally controlled to improve the safety and stability.

4.2.1 Longitudinal Tire Force Estimation

The longitudinal tire force is estimated based on rotational wheel dynamics as shown in Figure 4.2(a). The rotational wheel dynamics is described by following equation:

$$I_{\omega,i}\dot{\omega}_i = T_i^m - T_i^b - r_\omega F_i^x \tag{4.1}$$

where $I_{\omega,i}$ is the spin inertia of the wheel, T^m, T^b, ω, r_ω, and F^x are the in-wheel motor's torque, brake torque, wheel angular velocity, and effective tire radius, respectively. It is noted

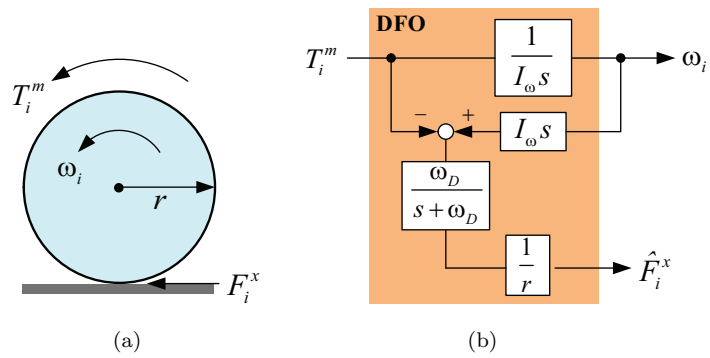

Figure 4.2: Driving force observer (DFO).

that torques of in-wheel motors and each wheel's angular velocity are directly obtained from motor currents and resolvers. On the other hand, the brake torque applying on each wheel is estimated from the measured brake pressure.

Several methods for longitudinal tire force estimation were presented in literatures (*Sado et al.*, 1999; *Cho et al.*, 2010; *Rajamani et al.*, 2011a). In *Cho et al.* (2010); *Rajamani et al.* (2011a), the wheel angular velocity observer is designed based on rotational wheel dynamics and includes the estimated longitudinal tire force. This longitudinal tire force is estimated in order to make the error dynamics of wheel angular velocity be asymptotically stable. In this thesis, based on dynamic tire model and accurate measurements of in-wheel motor's torque and wheel angular velocity, a simple estimator is design as follows:

$$\hat{F}_i^x = \frac{\omega_D}{s+\omega_D}\left(\frac{T_i^m - I_\omega \omega_i s}{r}\right) \tag{4.2}$$

where the angular velocity of the wheel ω_i is measured, the in-wheel motor torque T_i^m is measured from the motor current, ω_D is a cutoff frequency of the applied low-pass filter which rejects high frequency noises caused by time derivative of ω_i, and $\hat{F}_i^x$ is the estimated longitudinal tire force, moreover, tire parameters such as r and I_ω are assumed to be known. Note that the driving force observer shown in Figure 4.2(b) is quite similar to the well-known disturbance observer structure. Estimation results for longitudinal tire force estimation are shown in Figure 4.3(a). This simple structure makes it easy to be applicable to vehicle motion control systems.

4.2.2 Measurement of Lateral Tire Force

In authors' previous literature (*Nam et al.*, 2011, 2012b,a), cost-effective lateral tire force sensors, called MSHub units shown in Figure 2.19, are introduced and used for vehicle state estimation. In many conventional vehicles, wheel hub units with built-in active ABS sensors (i.e., wheel velocity sensor) were equipped. Comparing MSHub units with wheel hub units which are currently used in vehicles, MSHub units have almost the same mechanical structure except for rolling elements in a pair of rows and is capable of being constructed at a low cost. The measurement principle is as follows: the revolution speeds of rolling elements in a pair of rows are sensed by a pair of revolution speed sensors and difference of sensed revolution speeds is used to calculate the radial or axial loads (*Koichiro Ono*, 2009). As shown in Figure 2.19, a MSHub unit is installed on rotational axis of the wheel. Through novel load measuring techniques invented by NSK. Ltd., the accurate lateral tire force measurements using MSHub units can be realized without much additional cost and, due to cost-effective aspects, MSHub units are recently considered practically-applicable to vehicle control systems by several automotive manufacturers.

In literatures *Dakhlallah et al.* (2008); *Doumiati et al.* (2009, 2010), lateral tire force estimation methods, using nonlinear tire models, lateral vehicle dynamics, and available sensors used in conventional vehicle systems, were presented and evaluated from field tests. Even though they can provide relatively accurate estimates without additional expensive sensors, there still exist limitations in actual application to vehicle control systems. Because these methods can not cope with the variation of parameters in nonlinear tire model and vehicle models and calculation complexity caused by large dimension of observer models is very challenging issue in practical application. Although, by using lateral tire force sensors, a slight increase in sensor price is expected, this kind of cost-effective sensors can provide novel solutions in problems with vehicle state estimation and motion control.

4.2.3 Vertical Tire Force Estimation

The vertical tire force F_i^z is obtained from following equations in which the effects of weight transfer due to longitudinal and lateral accelerations are considered:

$$F_{fl}^{z} = mg\left[\frac{l_r}{2l} - \frac{a_x}{g}\frac{h_{\mathrm{CG}}}{2l} - \frac{a_y}{g}\frac{l_r h_{\mathrm{CG}}}{dl}\right] \quad \text{Front left} \tag{4.3a}$$

$$F_{fr}^{z} = mg\left[\frac{l_r}{2l} - \frac{a_x}{g}\frac{h_{\mathrm{CG}}}{2l} + \frac{a_y}{g}\frac{l_r h_{\mathrm{CG}}}{dl}\right] \quad \text{Front right} \tag{4.3b}$$

$$F_{rl}^{z} = mg\left[\frac{l_f}{2l} + \frac{a_x}{g}\frac{h_{\mathrm{CG}}}{2l} - \frac{a_y}{g}\frac{l_f h_{\mathrm{CG}}}{dl}\right] \quad \text{Rear left} \tag{4.3c}$$

$$F_{rr}^{z} = mg\left[\frac{l_f}{2l} + \frac{a_x}{g}\frac{h_{\mathrm{CG}}}{2l} + \frac{a_y}{g}\frac{l_f h_{\mathrm{CG}}}{dl}\right] \quad \text{Rear right} \tag{4.3d}$$

where g is the gravity acceleration, l denotes the wheelbase, h_{CG} is the height of the center of gravity from ground, and d is the track width.

In order to avoid the complexity of the suspension dynamics and difficulty in considering the disturbances from road, in this study, the influences of suspension dynamics and road disturbances are ignored and the weight transfer by acceleration is considered. This estimation method is reasonable when the road surface is not too bumpy which generates undesirable force disturbances.

Figure 4.3 shows the sensor measurement for lateral tire forces, and estimated longitudinal, vertical tire forces from (4.3a)–(4.3d), respectively. To validate the measured and estimated tire forces in various driving situations, several types of steering command (e.g., sine-steer, pulse-steer, and high frequency steer etc.) is applied to an experimental electric vehicle. Figure 4.3(a) illustrates the estimated longitudinal tire force by DFO. Lateral tire forces measured by MSHub units are presented in Figure 4.3(b). To remove high frequency noises, a signal processing technique (e.g., rate limiter and low-pass filter) is used. Figure 4.3(c) and (d) shows the results of vertical tire force estimation. To evaluate the estimated tire forces, vertical potentiometers are used to measure the real vertical tire forces. We can confirm that estimated vertical forces of front left and right tires (i.e., dotted blue line and dotted red line in Figure 4.3(c) and (d), respectively) are well matched to the sensor measurements.

4.3 Estimation of Instantaneous Lateral Tire Force Limit

In this section, a real-time algorithm for calculating the lateral tire force limit is presented. This estimated lateral tire force limit is used to constrain the desired front lateral tire force $F_f^{y\star}$ for avoiding uncontrollable situation (i.e., lateral tire force saturation). Since the proposed

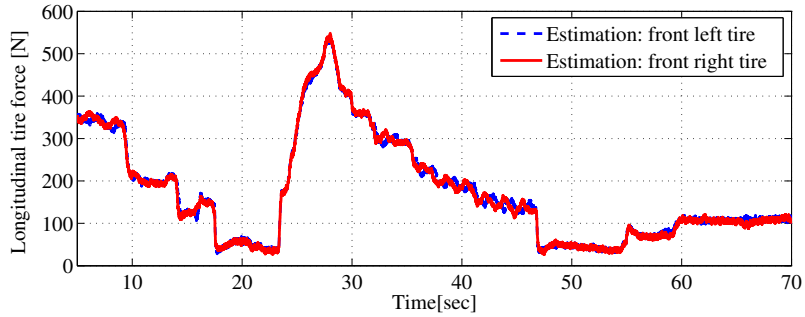

(a) Estimated longitudinal tire forces of the the front tires.

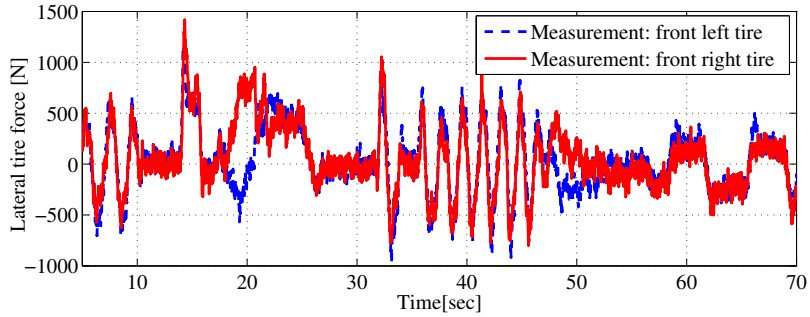

(b) Measured lateral tire forces of the front tires.

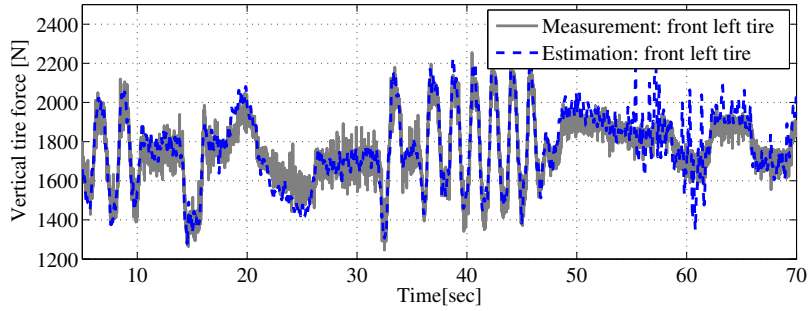

(c) Estimated and measured vertical tire forces of the front left tire.

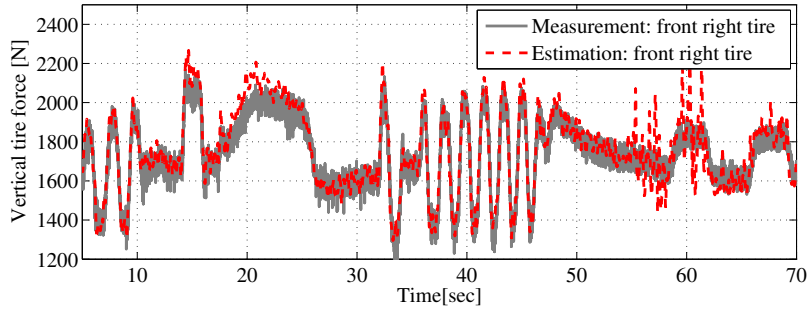

(d) Estimated and measured vertical tire forces of the front right tire.

Figure 4.3: Results of tire force estimation and measurement.

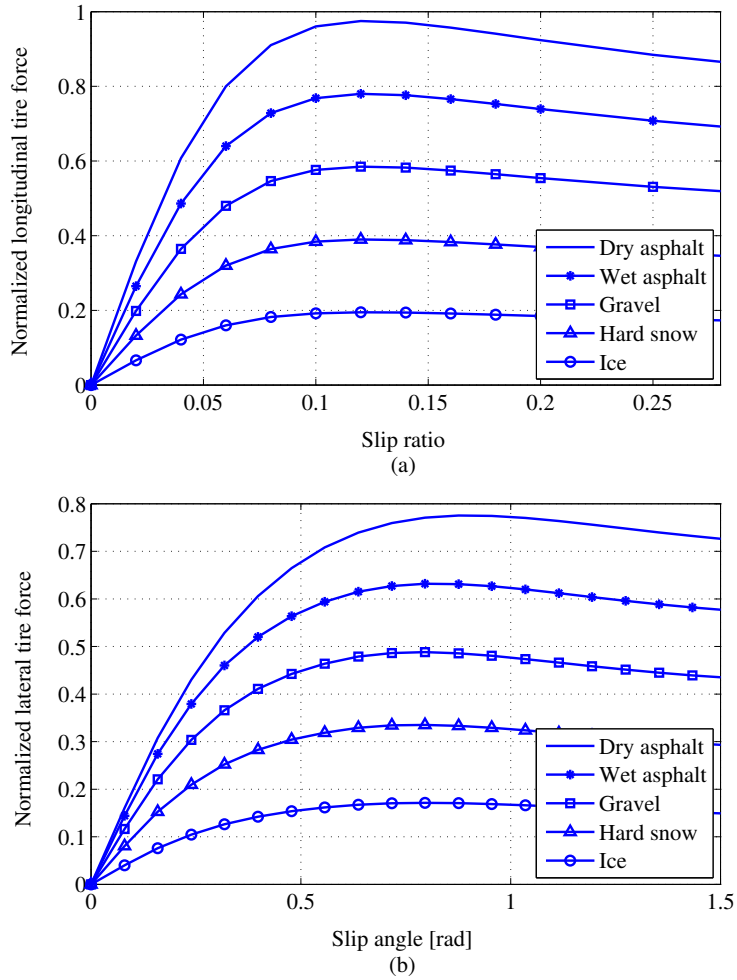

Figure 4.4: Normalized tire force curves with respect to various roads. (a) Normalized longitudinal tire force versus slip relation ship when the slip angle is equal to zero. (b) Normalized lateral tire force versus slip angle when the slip ratio is equal to zero.

control system is proposed for stabilizing the lateral motion, i.e., control in cornering situation, an estimation algorithm is developed based on lateral vehicle motion. Figure 4.4 illustrated the characteristics of lateral tire forces on various road surfaces. In the linear region of the tire force (i.e., small tire slip angle region), the lateral tire force generated at tires is proportional to its slip angle for any given road surface and vertical tire force. To estimate the peak point of normalized lateral tire force as shown in Figure 4.4, the nonlinear curve can be simplified.

4.3.1 Estimation Algorithm: Real-Time Estimation of Lateral Tire Force Limit

The relationship curve between normalized lateral tire force and tire slip angle is approximated as follows:

$$\rho_f = \frac{F_f^y}{F_f^z} = f(\alpha_f) \;\approx\; C_1\alpha_f + C_2{\alpha_f}^2 \tag{4.4}$$

where ρ_f is the normalized front lateral tire force, C_1, C_2 are the characteristic coefficients which decide the normalized lateral tire force–tire slip angle curve, and α_f is the tire slip angle which is calculated based on geometric derivation using wheel velocity vectors. If the velocities at wheel ground contact points are known, the tire slip angles can be easily derived geometrically and are given by *Rajamani* (2011):

$$\alpha_f = \beta + \frac{\gamma l_f}{v_x} - \delta_f \tag{4.5}$$

Here, the yaw rate γ and front steering angle δ_f are directly measured by gyro and angle sensors, respectively, the longitudinal vehicle velocity at CG, v_x, is obtained from the velocities of non-driven wheels, and the vehicle sideslip angle β is estimated by the nonlinear observer (*Nam et al.*, 2012a), which has been proposed by an author. In our previous literature *Nam et al.* (2012a), an EKF, which has been developed using sensor measurements of lateral tire forces, was proposed to estimate the vehicle sideslip angle and experimentally verified.

In order to identify the characteristic coefficients C_1 and C_2 in (4.4), (4.4) is rewritten in a parameter identification form as

$$y(t) = \varphi^T(t)\theta(t) \tag{4.6}$$

where $\theta(t)$=$[C_1, C_2]^T$, $\varphi^T(t)$=$[\alpha_f, {\alpha_f}^2]$, and $y(t)$=F_f^y/F_f^z and F_f^y, F_f^z are the sensor measurement and estimated forces as described in Section 4.2

A RLS algorithm is used to estimate $\theta(t)$ in (4.6),

$$\hat{\theta}(t) = \hat{\theta}(t-1) + K(t)[y(t) - \varphi^T(t) \cdot \hat{\theta}(t-1)] \tag{4.7}$$

$$K(t) = P(t-1)\varphi(t)[\lambda I + \varphi^T(t)P(t-1)\varphi(t)]^{-1} \tag{4.8}$$

$$P(t) = \frac{1}{\lambda}[I - K(t)\varphi^T(t)]P(t-1)/\lambda \tag{4.9}$$

where I is the identity matrix, $K(t)$, $P(t)$ are the Kalman gain and covariance matrices, and a forgetting factor λ is chosen as 0.995. The smaller λ is, the less weight is assigned to the older data; that is, the past data are forgotten faster. It should be noted that the reliability of the parameter estimation significantly depends on the qualities of the input data and output measurements, i.e., measured lateral tire forces and front tire slip angle. Thus, so as to provide the reliable estimation, the parameters are not updated when the absolute values of lateral tire forces and tire slip angle are less than certain small values.

As aforementioned, the normalized lateral tire forces–tire slip angle curve is approximated as second-order polynomial functions through real-time identification of characteristic coefficients using a RLS algorithm. To find the peak point of normalized lateral tire force as shown in Figure 4.4, an optimal tire slip angle, i.e., $\alpha_{f,\text{opt}}$, is easily calculated by differentiating the polynomial equation (4.4) with respect to the front tire slip angle as follows:

$$\frac{\partial \rho_f}{\partial \alpha_f} = C_1 + 2C_2\alpha_f \tag{4.10}$$

$$\alpha_{f,\text{opt}} = -\frac{C_1}{2C_2}. \tag{4.11}$$

Note that an aforementioned equation is used for real-time calculation of the instantaneous maximum normalized force $\rho_{y,\max}$ as

$$\rho_{y,\max} = C_1(\alpha_{f,\text{opt}}) + C_2(\alpha_{f,\text{opt}})^2 = -\frac{C_1^2}{4C_2}. \tag{4.12}$$

An instantaneous maximum normalized force $\rho_{y,\max}$ which is calculated by using (4.12) is used for estimating the instantaneous lateral tire force limit and this value is used to place the limitation

to desired lateral tire force for avoiding uncontrollable steering situation. From (4.4), the lateral tire force limit at each time step can be calculated as

$$F^{y}_{f,\mathrm{lim}}(t) \;=\; \rho_{y,\max}(t)F^{z}_{f}(t). \tag{4.13}$$

Figure 4.5 shows the results of the proposed algorithm for calculating instantaneous lateral tire force limit. Figure 4.5(a)–(c) represents the estimated characteristic coefficients C_1 and C_2,

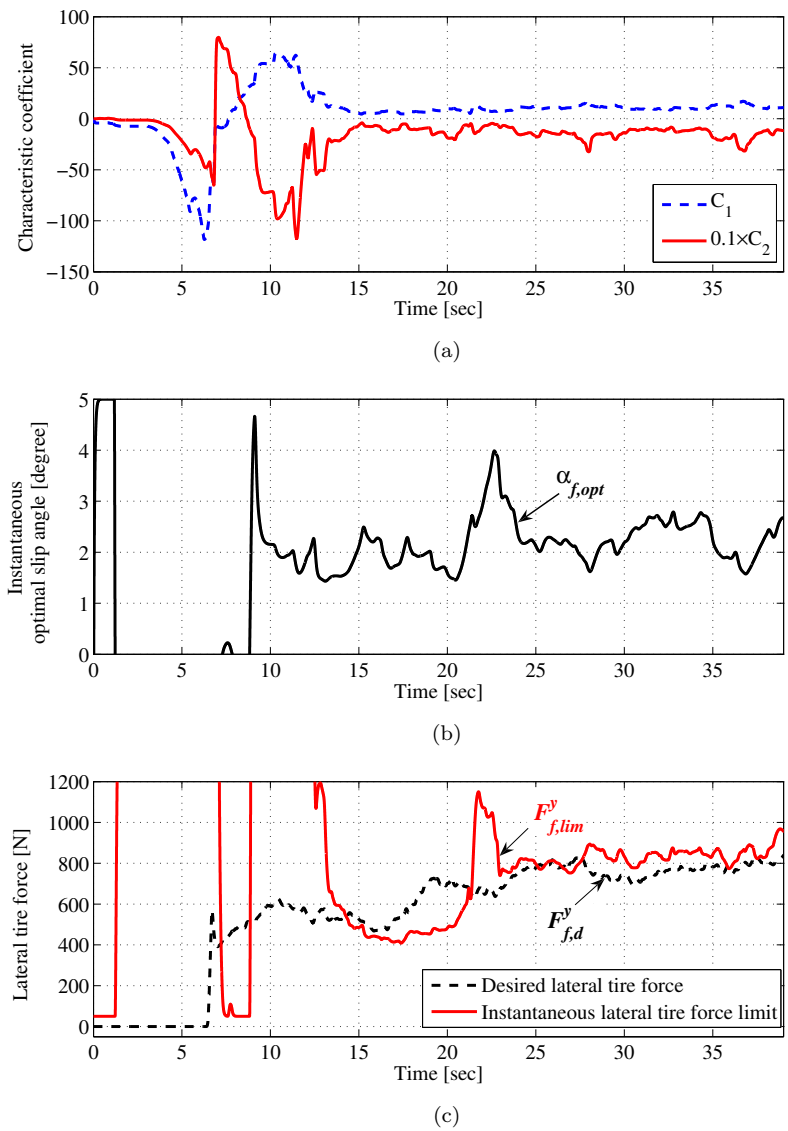

Figure 4.5: Estimation results of instantaneous lateral tire force limit. (a) Characteristic coefficients. (b) Instantaneous optimal slip angle. (c) Instantaneous lateral tire force limit.

calculated optimal tire slip angle $\alpha_{f,\mathrm{opt}}$, and the instantaneous lateral tire force limit $F^{y}_{f,\mathrm{lim}}$, respectively. We can confirm that if the tire slip angle and normalized lateral tire force are both available, then the instantaneous lateral tire force limit can be calculated. The proposed concept of instantaneous lateral tire force limit estimation is capable of predicting the cornering conditions on each road and thereby more reliable LTFC can be applicable to vehicles with MSHub units and SbW system. This is one of advantages with using cost-effective MSHub units.

4.4 Chapter Summary

In this chapter, a real-time algorithm for calculating the lateral tire force limit is presented. This estimated lateral tire force limit is used to constrain the desired front lateral tire force $F^{y\star}_{f}$ for avoiding uncontrollable situation (i.e., lateral tire force saturation). Since the proposed control system is proposed for stabilizing the lateral motion, i.e., control in cornering situation, an estimation algorithm is developed based on lateral vehicle motion.

CHAPTER V

Advanced Motion Control Based on Robust Sideslip Angle Estimation (without Tire Force Control)

5.1 Introduction

In this chapter, a new control scheme, utilizing active front steering through a SbW system and independent in-wheel motor control, is presented as a practical solution to the vehicle stability issues in an IWM-EV. A 2-DOF control method, which is widely applied in many motion control systems, is used to generate front steering angle and direct yaw moment to be controlled for stabilizing vehicle motion.

5.2 Control System Configuration

In this section, a lateral stability control system for the IWM-EV is presented and its effectiveness is evaluated through simulation and experiments. The overall control scheme in Figure 5.1 is as follows.

1. First, the desired vehicle responses are obtained from a linear vehicle model and driver's commands such as a steering angle and vehicle speed.

2. Second, the lateral stability controller is designed to make the vehicle follow the desired vehicle motion trajectory. The proposed control system has been designed in two stage, namely, the upper and low level control stages as shown in Figure 5.1. The upper level controller is composed of sideslip angle and yaw rate tracking controllers. At lower level

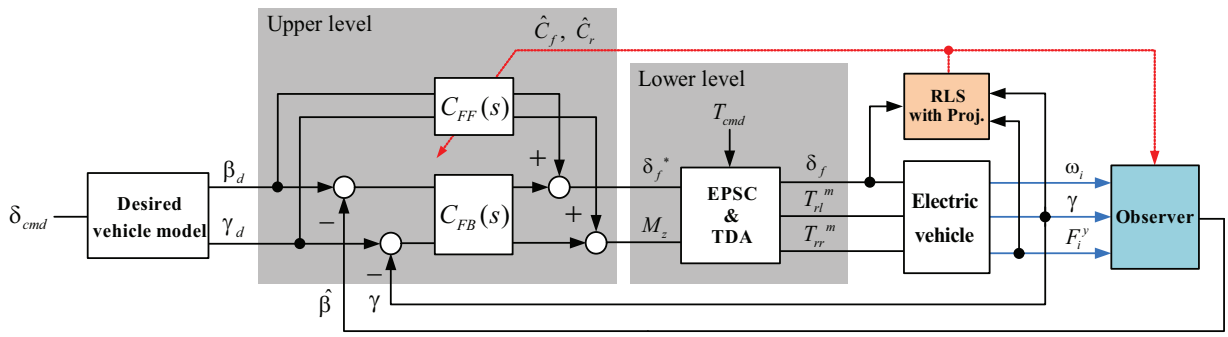

Figure 5.1: Control structure of the proposed stability control system (EPSC: EPS controller, TDA: Torque distribution algorithm).

controller, it is composed of control torque distribution algorithm and an EPS motor controller.

3. Third, the sideslip angle observer based on EKF approach is designed for providing accurate sideslip angle information to the stability controller. As explained in Chapter III, a proposed EKF utilizes the estimated tire cornering stiffness and measured lateral tire forces. The RLS algorithm with a projection function is used to iteratively update the unknown parameters, i.e., tire cornering stiffness, and the estimated parameters are used: (1) to update the feedforward controller; (2) as measurable state variables in EKF.

In this section, we present the new control scheme, utilizing active front steering through a SbW system and independent in-wheel motor control, as a practical solution to the vehicle stability issues in an IWM-EV. A 2-DOF control method, which is widely applied in many motion control systems, is used to generate front steering angle and direct yaw moment to be controlled for stabilizing vehicle motion.

5.3 Reference Model Generation

The objective of the stability control is to improve the vehicle steadiness and transient response properties, enhancing vehicle handling performance and maintaining stability in those cornering maneuvers, i.e., the yaw rate γ or sideslip angle β of the vehicle should be close to desired vehicle responses (γ_d and β_d). Desired vehicle responses are defined based on driver's cornering intention (e.g., drivers' steering command and vehicle speed). In usual, vehicle responses

during steady state cornering (i.e., $\dot{\beta} = \dot{\gamma} = 0$ in (2.31)) are used as desired vehicle responses. Desired vehicle sideslip angle and yaw rate for given steering angle and vehicle speed are defined as follows:

$$\beta_d = \left(\frac{\omega_\beta}{s+\omega_\beta}\right) \cdot \frac{1 - \left(\frac{m l_f v_x^2}{2 l l_r C_r}\right)}{1 + K_s v_x^2} \frac{l_r}{l} \cdot \delta_{\text{cmd}} \tag{5.1}$$

$$\gamma_d = \left(\frac{\omega_\lambda}{s+\omega_\lambda}\right) \cdot \frac{1}{1 + K_s v_x^2} \frac{v_x}{l} \cdot \delta_{\text{cmd}} \tag{5.2}$$

$$K_s = \frac{m(l_r C_r - l_f C_f)}{2 l^2 C_f C_r} \tag{5.3}$$

where ω_β and ω_λ are cutoff frequencies (e.g., in this case, 20 rad/s was chosen) of desired model filters, respectively, and K_s represents vehicle motion behavior by steering action (see section 2.2).

5.4 Upper-Level Controller Design

The upper-level controller generates desired yaw moment $M_z^\star$ and front steering angle $\delta_f^\star$ to stabilize the lateral vehicle motion. To improve the tracking performances, 2-DOF control methodology is used. In 2-DOF control system, both the closed-loop characteristics and the feedback characteristics can be adjusted independently to improve the system response performance.

5.4.1 Adaptive Feedforward Control

In proposed stability control system, the front steering angle δ_f and direct yaw moment M_z are used as controllable inputs. The front steering control is realized by a SbW system including active EPS motor control. While, the direct yaw moment control is realized by independent rear in-wheel motor control. Integrated control, which utilizes steering and driving torque control at the same time, was designed to satisfy the tracking performances of sideslip angle and yaw rate. Considering that a vehicle dynamics model, used in controller design, shows the time-varying characteristics due to varying parameters (e.g., tire cornering stiffness or vehicle speed), an adaptive feed-forward controller is designed to handle those parameters.

In conventional one degree-of-freedom controllers (e.g., PID controller, etc.), the only problem of the fixed robust controller is that the control performance of closed-loop system becomes too conservative when the parameter variation in the vehicle model is too large (*Ackermann*, 2002). For this reason, adaptive feed-forward controller with parameter estimation is proposed to improve the tracking performance.

An adaptive feed-forward controller is proposed based on real-time parameter adaptation, described in Chapter III. The adaptive feed-forward controller is designed based on inverse vehicle dynamics (i.e., it is assumed that $G(s)$ is invertible.) and given by

$$C_{\mathrm{FF}}(s) = \hat{B}^{-1}(sI - \hat{A}) = \begin{bmatrix} \hat{G}_{11} & \hat{G}_{12} \\ \hat{G}_{21} & \hat{G}_{22} \end{bmatrix}^{-1} \tag{5.4}$$

where elements of the feed-forward controller $C_{\mathrm{FF}}(s)$ are described in Section 2.2. The each element is updated based on estimated tire cornering stiffness and calculated vehicle speed. The average value of the nondriven wheel velocities is used for vehicle speed. Considering that an electric vehicle used in field tests was a rear-wheel drive vehicle, it is reasonable to use nondriven wheel's velocity as vehicle speed. In case that the wheel slip occurs in nondriven wheels due to sudden braking, we can not use nondriven wheel's velocity for calculating vehicle speed. In *Suzuki and Fujimoto* (2010), the robust slip ratio estimation method was proposed and evaluated through experiments. If we know the wheel slip ratio, vehicle speed can be easily calculated from measured wheel velocity regardless of acceleration and deceleration.

5.4.2 Feedback Control

It is assumed that the open-loop plant can be stabilized by an appropriate feedback controller $C_{\mathrm{FB}}(s)$, taking account of closed-loop stability and disturbance rejection. In case of vehicle plant, plant variation due to tire-road condition change (i.e., tire cornering stiffness) is large and it makes control performances of closed-loop system conservative. In feedback control design, a decoupling control method was applied to stabilize the vehicle lateral motion. Transfer functions between control inputs and outputs, shown in Appendix A, are interconnected each other and thereby we have to compensate interconnection effects. The feedback controller $C_{\mathrm{FB}}(s)$ is designed as

follows:

$$C_{\mathrm{FB}}(s) = \begin{bmatrix} C_\beta(s) & \rho_1(s)C_\gamma(s) \\ \rho_2(s)C_\beta(s) & C_\gamma(s) \end{bmatrix} \tag{5.5}$$

where $C_\beta(s)$ and $C_\gamma(s)$ are the PI compensator and are independently designed based on pole-placement, interaction controllers $\rho_1(s)$ and $\rho_2(s)$ are selected based on a decoupling control method (*Skogestad and Postlethwaite*, 1996) and are given by

$$\rho_1(s) = -G_{11}(s)^{-1}G_{12}(s) \approx -G_{11}(0)^{-1}G_{12}(0) \tag{5.6}$$

$$\rho_2(s) = -G_{22}(s)^{-1}G_{21}(s) \approx -G_{22}(0)^{-1}G_{21}(0). \tag{5.7}$$

Here, the steady state interconnection is only considered for avoiding complicated decoupling structures. This implies that a proposed interaction controller contributes to minimize the strong interconnection effects of the vehicle states to be controlled.

5.5 Low-Level Controller Design

5.5.1 Control Allocation

The control yaw moment M_z, which is generated from an upper controller, is distributed to two rear in-wheel motors based on following equations (*Fujimoto et al.*, 2005).

$$M_z = \frac{d}{2}(F_{rr}^x - F_{rl}^x) \tag{5.8}$$

$$T_{\mathrm{cmd}} = T_{rr}^m + T_{rl}^m \tag{5.9}$$

where torque control commands to two rear in-wheel motors are calculated as $T_{rr}^m = rF_{rr}^x$ and $T_{rl}^m = rF_{rl}^x$, respectively. Note that, in this study, we have only utilized the rear in-wheel motors for controlling the yaw moment and thereby a simple torque distribution algorithm is applied. In future study, front in-wheel motors and novel control allocation algorithms (*Jonasson et al.*, 2011; *Wang et al.*, 2011) can be applicable to motion control systems of IWM-EV for improving the control flexibility and energy efficiency.

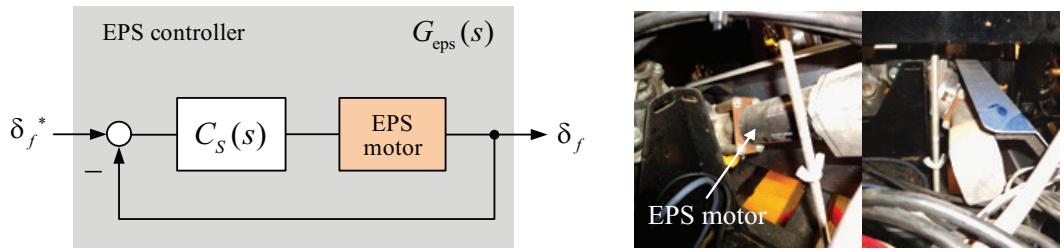

(a) (b)

Figure 5.2: EPS control system. (a) Block diagram of a EPS controller. (b) Real view of EPS motor.

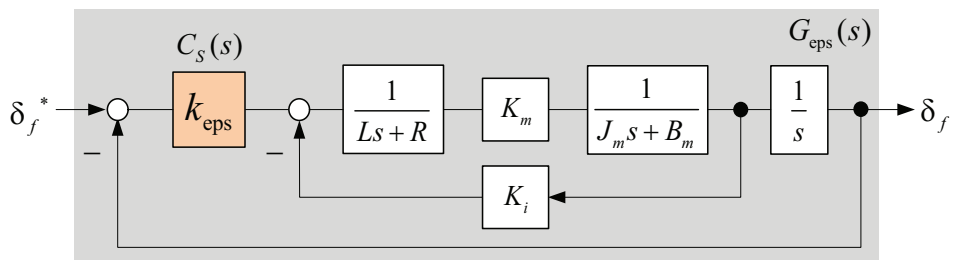

Figure 5.3: Block diagram for the EPS control system.

5.5.2 EPS Controller

EPS motor control (under position control) is employed for realizing a SbW system. As shown in Figure 5.2(a), the feedback controller $C_{\text{EPS}}(s)$ is designed for actual steering angle to track the reference front steering angle $\delta_f^\star$ which is generated from the upper controller. A constant feedback gain (i.e., proportional gain) was chosen to guarantee system bandwidth up to 15 Hz. An EPS motor, shown in Figure 5.2(b), is a high speed DC motor with 250W power output.

The servo system for an EPS motor is shown in Figure 5.3, which is designed and analyzed from the viewpoint of conventional motion control of dc motor (*Ogata*, 2010). The transfer function between reference steering angle and measured steering angle is obtained as

$$G_{\text{eps}}(s) = \frac{\delta_f}{\delta_f^*} = \frac{k_{\text{eps}}K_m}{J_m L s^3 + (LB_m + J_m R)s^2 + (B_m R + K_m K_i)s + k_{\text{eps}}K_m} \tag{5.10}$$

where J_m is the moment of inertia referred to the steering shaft, B_m is the viscous-friction coefficient, K_m is a motor torque constant, K_i is the back emf constant, L is the motor inductance, R is the electrical resistance, and k_{eps} is an adjustable feedback gain of the EPS motor position

controller. For the sake of control design simplicity, the transfer function (5.10) is simplified to

$$G_{\text{eps}}(s) \;=\; \frac{\omega_{\text{eps}}}{s+\omega_{\text{eps}}} \tag{5.11}$$

where ω_{eps} is the cutoff frequency of EPS servo system, which is chosen as $2\pi \cdot 15$ rad/sec. This simplified transfer function of an EPS control system is used in LTFC design.

5.6 Simulation and Experiment

5.6.1 Computer Simulation

Computer simulation was performed to evaluate the proposed stability control system. Based on specifications of an experimental IWM-EV (see Table I), the simulation vehicle model was obtained using CarSim. Simulation environment using CarSim model and Matlab/simulink was constructed for implementation of proposed control algorithms. The proposed stability control system was evaluated through cosimulation for single lane change tests. Single lane change tests were carried out at $v_x = 70$ km/h on a low-μ road (i.e., $\mu \simeq 0.4$).

Figure 5.4 shows the simulation results. Figure 5.4(a) and (b) represent a control front steering angle and yaw moment. As shown in Figure 5.4(d), if the control is set off, the vehicle sideslip angle increases, which causes the vehicles to lose stability and unable to accomplish the desired vehicle motion. By applying the proposed control algorithm, yaw rate and sideslip angle are successfully controlled to follow desired values with small errors.

5.6.2 Experiment

A proposed stability control algorithm is implemented on an experimental IWM-EV shown in Figure 2.16. The single lane change maneuver has been done on dry asphalt (i.e., $\mu \simeq 0.9$). Figure 5.5 represents the experimental results of an uncontrolled vehicle. The beginning of the first 6 s is the period of the acceleration to achieve the constant vehicle speed. A wheel steering command is given in the control algorithm and a EPS motor controller has been activated by a driver to track the wheel steering command. On the other hand, yaw rate and sideslip angle controllers are not activated. From the results of Figure 5.5(a) and (b), we can confirm that

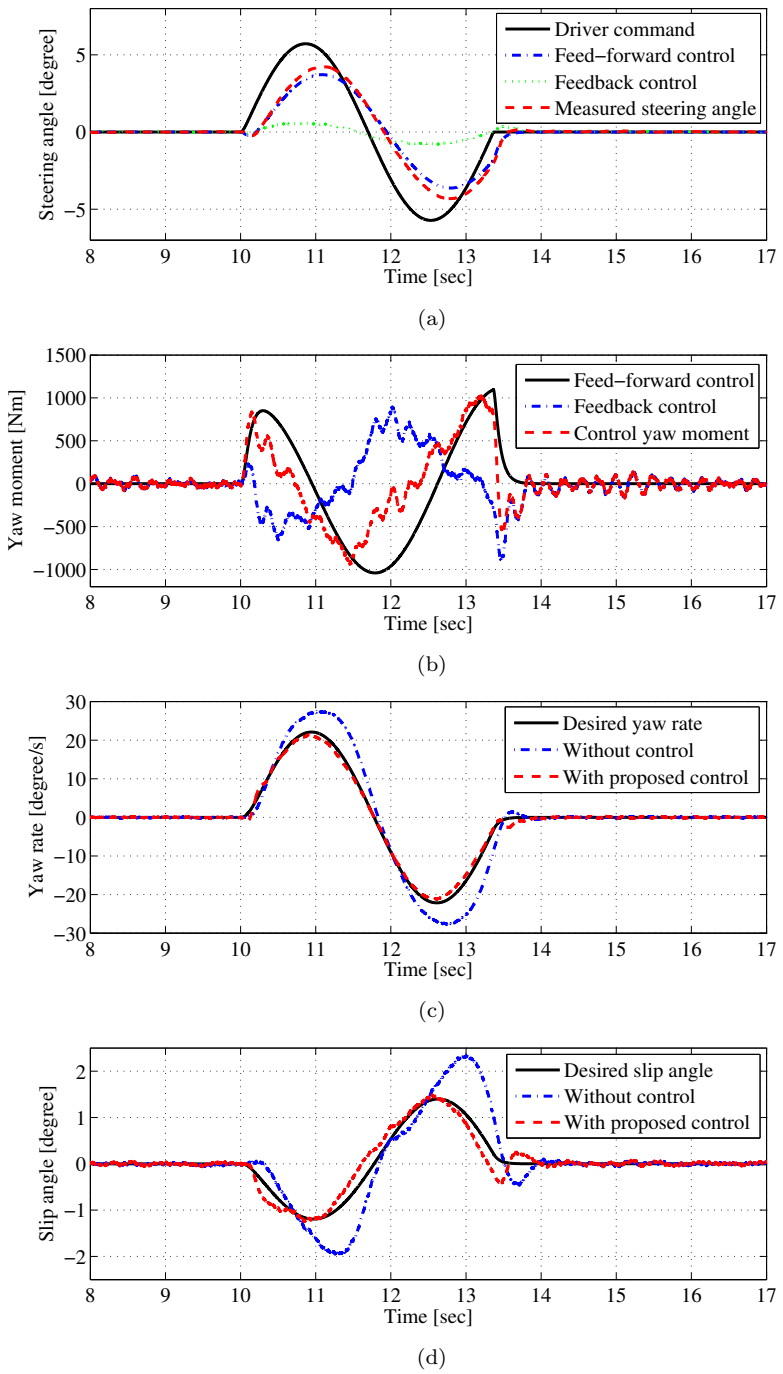

Figure 5.4: Simulation results for single lane change at 70 km/h. (a) Steering angle. (b) Yaw moment. (c) Yaw rate. (d) Side slip angle.

an uncontrolled vehicle do not follow the desired vehicle trajectory (e.g., maximum value of yaw rate and sideslip angle errors are about 7 °/s and 0.75 °).

With the same maneuver, experiments have been performed to evaluate the proposed stability

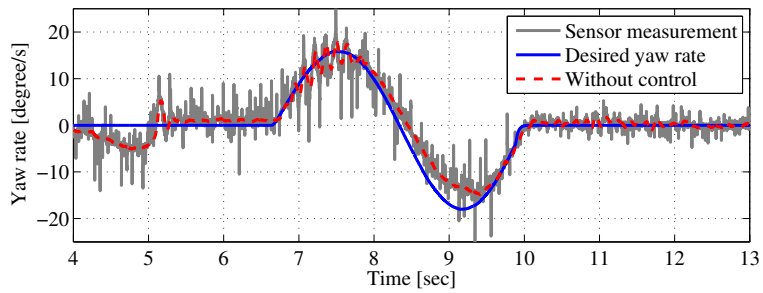

(a)

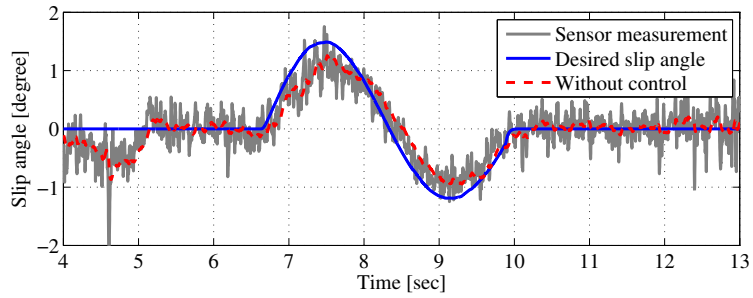

(b)

Figure 5.5: Experimental results for an uncontrolled vehicle. (a) Yaw rate: without control. (b) Side slip angle: without control.

control system. Figure 5.6 shows the results of a controlled vehicle. Figure 5.6(a) represents control flags which imply the on/off states of sub-controllers (i.e., yaw rate and sideslip angle control). At $t = 3.7$ s, control switches for yaw rate and sideslip angle control are turned on. Figure 5.6(a) and (b) illustrate control commands of front steering angle and yaw moment to be controlled. The front steering angle is controlled to compensate a sideslip angle error and the yaw moment is generated to compensate a yaw rate error, respectively. Figure 5.6(c) and (d) show the yaw rate and side slip angle of a controlled vehicle with a proposed controller. Vehicle yaw rate with proposed control, i.e., thick red line in Figure 5.6(c), is the filtered value of sensor measurement (i.e., thick gray line in Figure 5.6(c)). As shown in Figure 5.6(c), the vehicle yaw rate with proposed control follows the desired yaw rate (i.e., dotted blue line). Similarly, the vehicle sideslip angle with proposed control well track the desired trajectory with small error. If we compare results of the control-case (Figure 5.6) and no-control-case (Figure 5.5), we can confirm that the proposed stability control system is effective for guaranteeing desired motion of the IWM-EV with a SbW system.

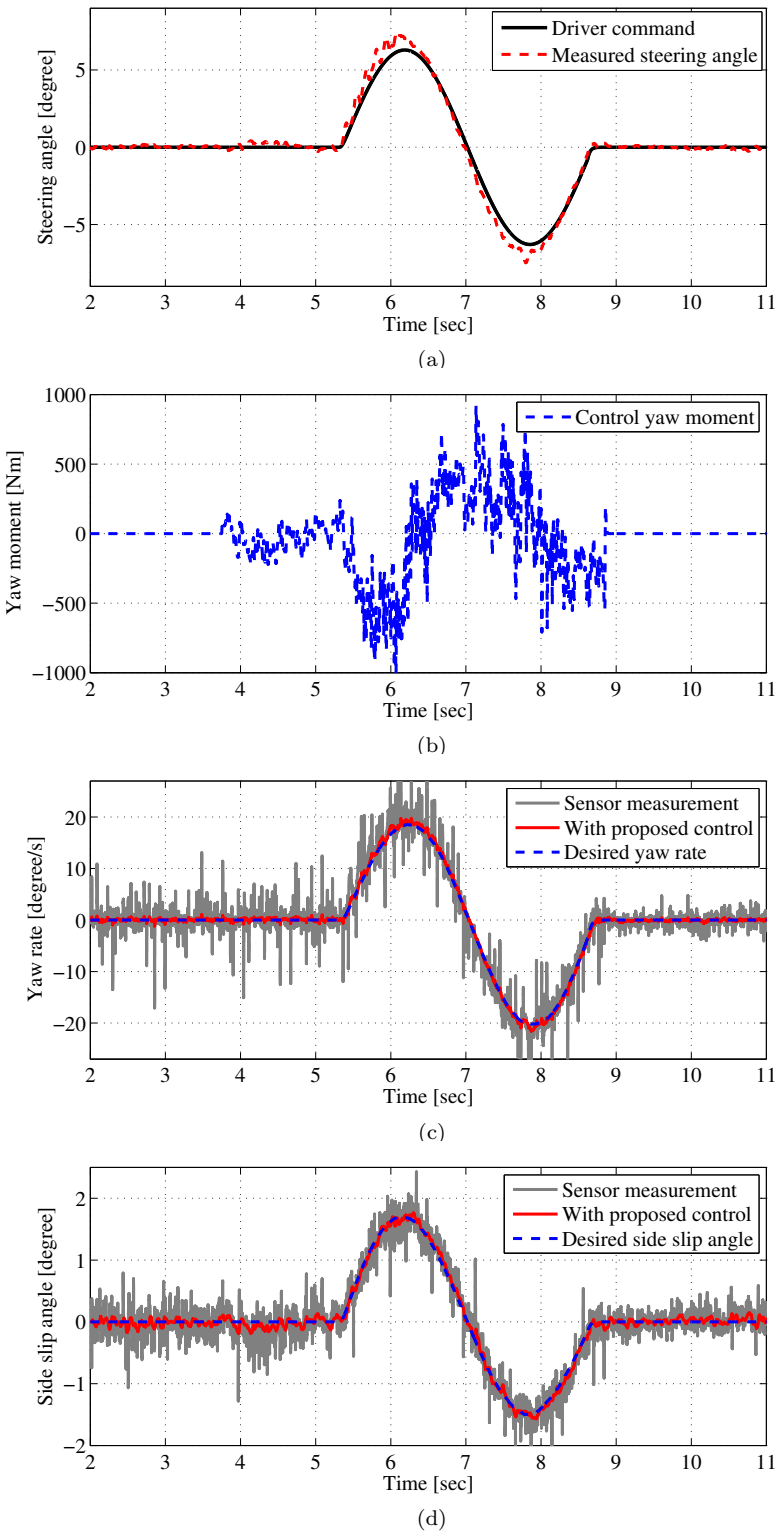

Figure 5.6: Experimental results for single lane change. (a) Steering angle. (b) Yaw moment. (c) Yaw rate. (d) Side slip angle.

5.7 Chapter Summary

In this chapter, an adaptive feedforward control-based motion control scheme utilizing active front steering through a SbW system and independent in-wheel motor control, is presented as a practical solution to the vehicle stability control issues in an IWM-EV. A 2-DOF control method, which is widely applied in many motion control systems, is used to generate front steering angle and direct yaw moment to be controlled for stabilizing vehicle motion. To verify the effectiveness of the proposed control system, computer simulation and field tests are carried out and control performance, i.e., reference tracking, is confirmed through test results.

CHAPTER VI

Advanced Motion Control Based on Lateral Tire Force Control

6.1 Introduction

Motion control algorithms for electric vehicles with in-wheel motors have been intensively developed based on independent in-wheel motor control and active steering control (*Hori et al.*, 1998; *Sakai et al.*, 1999; *Nagai et al.*, 2002; *Hori*, 2004; *Mutoh et al.*, 2007; *Ando and Fujimoto*, 2010). In order to stabilize the vehicle motion, independent in-wheel motor control and active steering control are treated in previous literatures (*Ando and Fujimoto*, 2010). In *Guvenc and Guvenc* (2002); *Guvenc et al.* (2009), the yaw stability controllers, which are realized by active front steering via SbW system, are designed and effectiveness of those controllers is verified by hardware-in-the-loop simulation and experiments, respectively. The potential benefits of the active front steering, to improve handling behavior during normal driving, have received considerable attention from the automobile industry (*Mammar and Koenig*, 2002; *Mokhiamar and Abe*, 2006). Most of the active front steering systems is mainly based on the vehicle state feedback, e.g., yaw rate, lateral acceleration, and vehicle sideslip angle feedback. The active steering control method based on the lateral acceleration and yaw rate feedback was presented and those methods demonstrate that active steering control can achieve greater driving stability than differential brake control (*Segawa et al.*, 2001). In *Yih and Gerdes* (2005), an intuitive method for altering a vehicle's handling characteristics by active steering control via SbW has been proposed and its effectiveness is verified through experiments.

As the vehicle motion is dominantly governed by the forces generated between tires and road, real-time knowledge of the tire forces is very important when predicting vehicle motion and

thereby real-time methods for tire-road forces estimation have been studied (*Doumiati et al.*, 2011; *Cho et al.*, 2010). Fortunately, cost-effective lateral tire force sensors, called MSHub units (*Koichiro Ono*, 2009), are recently invented by NSK Ltd. and are now under development for practical applications to commercial vehicles in the near future. In our previous work (*Nam et al.*, 2012b,a), new methods for vehicle sideslip angle estimation, which are based on lateral tire force sensors, have been proposed and experimentally validated. The use of lateral tire force sensors in motion control systems is able to provide following advantages (*Nam et al.*, 2012a);

- tire-road conditions can be easily predicted, e.g., during cornering, we can predict the tire-road conditions based on estimated tire cornering stiffness
- optimal tire force distribution is realizable using lateral tire force measurements and estimated driving forces
- vehicle motion can be controlled at tire force control level.

Aforementioned first and second advantages are validated through previous work of Hori/Fujimoto research team (*Ando and Fujimoto*, 2010; *Nam et al.*, 2012a). It is anticipated that future motion control systems will be able to increase the effectiveness of active safety interventions beyond what is currently available (*Falcone et al.*, 2007). This will be facilitated by using cost-effective sensors such as MSHub units used in this study.

6.2 Robust Lateral Tire Force Control

The main objective of the motion control system is to provide safety and stability in all driving regions and in the presence of undesirable external conditions such as strong wind or changing tire-road conditions. In this chapter, a novel motion controller based on direct lateral tire force control is proposed and it is realized via active front steering system. Since the vehicle motion is dominantly governed by forces acting on tires, the motion control based on tire force controls can contribute to improvement of handling and safety performances.

The overall control scheme in Figure 6.1 is given as follows.

1. First, the desired front lateral tire force $F_f^{y\star}$ is obtained from a linear vehicle model and driver's commands including a steering angle and vehicle speed. Note that the desired

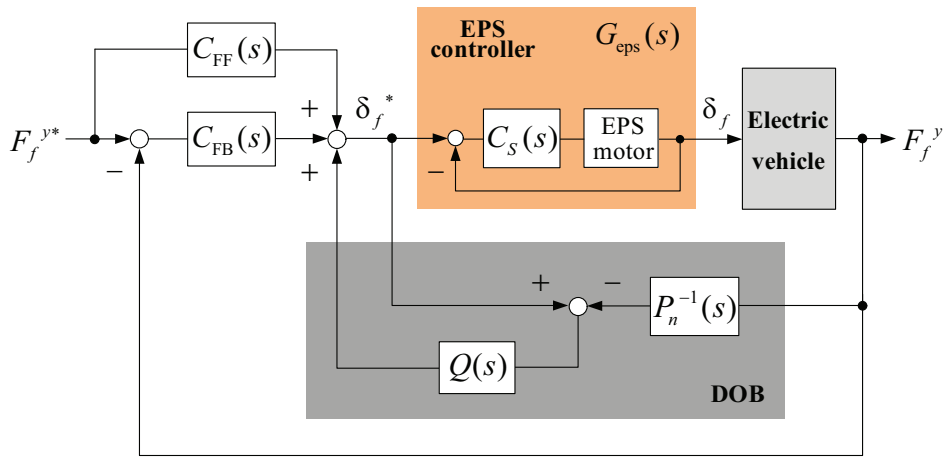

Figure 6.1: Block diagram of lateral tire force controller.

lateral tire force is constrained by the maximum lateral tire force limit which is presented in Section 4.3.

2. Second, the 2-DOF controller is designed based on the defined nominal model for improving the tracking performances.

3. Third, the DOB is designed to compensate for model variations caused by variation of vehicle speed and tire parameters, and to reject undesired disturbances. DOB makes the complicated tire force dynamics behave as a defined nominal tire model (*Sabanovic and Ohnishi*, 2011).

The proposed motion controller is composed of following subsystems.

6.2.1 Design of Nominal Model

The dynamic lateral force model for front tires, which is based on linearized tire models, is used for control design. It should be note that the lateral tire forces developed at the tire-road contact patch is expressed as a function of the tire slip angles which are calculated from the vehicle sideslip angle, yaw rate, longitudinal vehicle velocity, and steering angle. In this study, the active steering control is available for achieving the control objective and it is considered as an only controllable input. Thus, we can obtain a dynamic lateral tire force model which is

single-input and single-output system as follows:

$$\dot{F}_f^y = -\frac{1}{\tau_{\text{lag},f}} F_f^y - \frac{2C_f}{\tau_{\text{lag},f}}\beta - \frac{2l_f C_f}{\tau_{\text{lag},f} v_x}\gamma + \frac{2C_f}{\tau_{\text{lag},f}}\delta_f \tag{6.1}$$

Here, the tire forces generated by the influences of β and γ are considered as disturbances. Because, the vehicle sideslip angle β is not measurable due to sensor cost and the force generated by yaw rate γ term is significantly affected by varying parameter C_f and vehicle speed v_x. Thus, (6.1) can be rewritten as

$$\dot{F}_f^y = -\frac{1}{\tau_{\text{lag},f}} F_f^y + \frac{2C_{fn}}{\tau_{\text{lag},f}}\delta_f + F_d^y \tag{6.2}$$

where F_d^y indicates lumped lateral force disturbances, including the influences of β, γ, and ΔF^y which includes nonlinear tire forces and external disturbance like side wind forces, and it is represented as

$$F_d^y = -\frac{2C_f}{\tau_{\text{lag},f}}\left(\beta + \frac{l_f\gamma}{v_x}\right) + \Delta F^y. \tag{6.3}$$

Based on (6.2) and defined nominal parameters, a transfer function for the nominal lateral tire force model is obtained as

$$P_n(s) = \frac{F_f^y(s)}{\delta_f(s)} = \frac{2C_{f,n}}{1 + \tau_{\text{lag},fn} s} \tag{6.4}$$

where $C_{f,n}$ is a nominal front tire cornering stiffness for a value (i.e., = 12500 N/rad) on a high–μ road (i.e., $\mu \simeq 0.9$), $\tau_{\text{lag},fn}$ is a nominal relaxation time constant which is defined as a constant for the certain vehicle speed.

6.2.2 Generation of Desired Lateral Tire Force

The objective of the vehicle motion control is to improve the vehicle steadiness and transient response properties, enhancing vehicle handling performance and maintaining stability in those

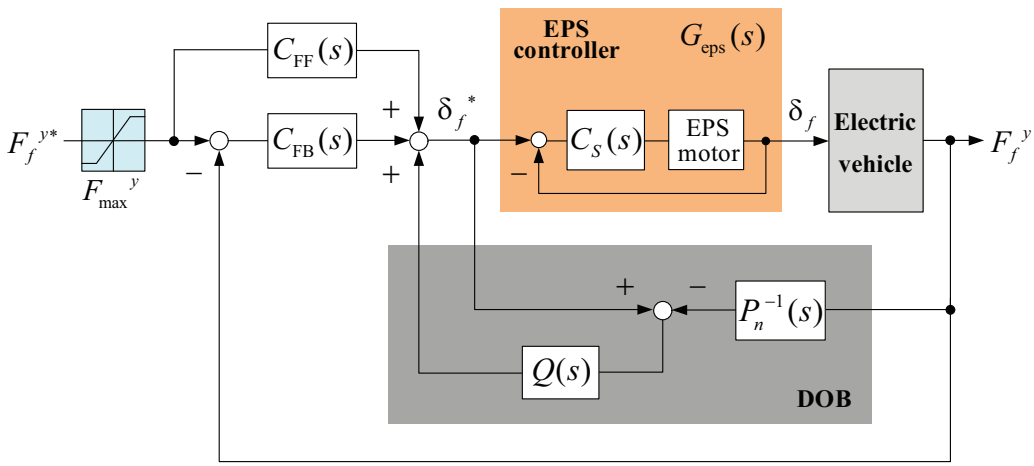

Figure 6.2: Block diagram of lateral tire force controller based on DOB.

cornering maneuvers, e.g., the yaw rate γ or sideslip angle β of the vehicle should be close to desired vehicle responses (γ_d and β_d). In this study, the advanced motion control method based on direct lateral tire force control has been proposed. This means that lateral tire forces, which the tires generate, should be controlled to follow the desired lateral tire forces $F_f^{y\star}$. Desired vehicle and tire force responses are defined based on driver's cornering intention (e.g., drivers' steering command and vehicle speed). In usual, vehicle responses during steady state cornering, i.e., $\dot{\beta} = \dot{\gamma} = 0$ in (2.13) and (2.14), are used as desired vehicle responses. Desired vehicle sideslip angle, yaw rate, and front lateral tire force for given steering angle and vehicle speed are defined as

$$F_f^{y\star} = \frac{\omega_f}{s + \omega_f}\left[\frac{I_z}{l_f + l_r}\dot{\gamma}_d + \frac{mv_x}{l_f + l_r}(\dot{\beta}_d + \gamma_d)\right] \tag{6.5}$$

where β_d and γ_d are presented in Section 5.3, the desired front lateral tire force $F_f^{y\star}$, described in (6.5), is obtained from lateral vehicle dynamics (2.13) and (2.14), ω_f is the cutoff frequency (e.g., in this case, 15 rad/s is chosen) of a tire force model filter. In reality, desired front lateral tire force $F_f^{y\star}$ is constrained by tire-road conditions (i.e., tire-road friction coefficient μ). For example, in case that a vehicle is in cornering situation on a slippery road, a desired lateral tire force calculated by (6.5) cannot be generated by tire-road interaction due to nonlinear tire force characteristic called tire force saturation. Therefore, a saturation function with adjustable

thresholds, shown in Figure 6.2, is used. $F^y_{\max}$ in Figure 6.2 is the same as $F^y_{f,\lim}$ illustrated in (4.13).

6.2.3 Design of 2-DOF Controller

To achieve the robust tracking control of front lateral tire forces, 2-DOF control methodology is used in control system design (*Umeno and Hori*, 1991; *Lee and Tomizuka*, 1996). The 2-DOF controller consists of two compensators, i.e., feed-forward compensator $C_{\mathrm{FF}}(s)$ and feedback compensator $C_{\mathrm{FB}}(s)$.

The feed-forward compensator $C_{\mathrm{FF}}(s)$ is designed as an inverse nominal model, i.e.,

$$C_{\mathrm{FF}}(s) = P_n^{-1}(s) = \frac{1 + \tau_{\mathrm{lag},fn} s}{2C_{f,n}} \tag{6.6}$$

where $\tau_{\mathrm{lag},fn} = 0.08$ s and $C_{f,n} = 12500$ N/rad are used in experiments. In real-time implementation on experimental IWM-EV, a low-pass filter was added to reduce the amplification of high frequency noises due to the effects of time derivative.

The feedback compensator $C_{\mathrm{FB}}(s)$ is designed as a conventional proportional-integration controller as follows:

$$C_{\mathrm{FB}}(s) = \frac{K_P s + K_I}{s} \tag{6.7}$$

where K_P, K_I are the proportional and integration gains, and these are chosen by pole placement based on the given performance specifications, e.g., tracking error at low frequency: $< 10\%$, control bandwidth of closed-loop system: 10 rad/s.

6.2.4 Design of DOB

The control of vehicle motion is challenged by the nonlinearities in tire models, model uncertainty, and difficulties in state estimation (e.g., vehicle sideslip angle β). To compensate for such undesired factors and unmeasurable terms, a DOB has been used in this study. In general, the DOB is used for rejecting disturbance and compensating for variation of plant dynamics by treating the variations as an equivalent disturbances. In the design of DOB, the selection of the

low pass filter called a Q-filter $Q(s)$ is very important. It is required to select $Q(s)$ such that $Q(s)P_n^{-1}(s)$ is realizable. In general, the $Q(s)$ is designed as a low-pass filter, which has the dc gain of one, such that the closed-loop system has a good disturbance rejection performance at low frequencies.

$$Q(s) = \frac{\omega_Q}{s + \omega_Q} \tag{6.8}$$

where ω_Q is a cutoff frequency of the $Q(s)$ which is designed by considering control performance requirements, in this application, we want to have a good control performance up to 10 rad/s.

6.3 Stability Analysis of the Control System

In this section, the stability of the proposed control system has been discussed. In particular, we have made stability analysis in the presence of multiplicative model uncertainty $\Delta(s)$ in the plant. Note that the vehicle system is subjected to large model variations due to varying parameters such as vehicle speed and tire-road parameters. In order to account for these model variations, a multiplicative model uncertainty $\Delta(s)$ is imposed on the defined nominal model as shown in Figure 6.3, i.e.,

$$P(s) = P_n(s)\left[1 + \Delta(s)\right] \tag{6.9}$$

where $P(s)$ is the actual plant which is assumed to be actual relationship between front steering angle δ_f to front lateral tire force F_f^y and it can be expressed in the Laplace domain from (6.1),

$$P(s) = \frac{F_f^y(s)}{\delta_f(s)} = \frac{-2C_f}{1 + \tau_{\text{lag},f}\, s}\left[G_{\beta\delta_f}(s) + \frac{l_f}{v_x}G_{\gamma\delta_f}(s) - 1\right] \tag{6.10}$$

where $G_{\beta\delta_f}(s)$ is the transfer function between a front steering angle and a vehicle sideslip angle, $G_{\gamma\delta_f}(s)$ is the transfer function between a front steering angle and a yaw rate. Both transfer functions are obtained from (2.13), (2.14), and lateral tire force model (2.46) [derivation of $G_{\beta\delta_f}(s)$ and $G_{\gamma\delta_f}(s)$ is represented in Chapter II].

Frequency responses of the actual plant can be obtained from (6.10) and it is assumed that time-varying parameters are physically bounded with certain values. A parameter set including the bounds of several parameters is defined as

$$\text{Parameter set:} \begin{cases} C_f \in (5000, 13000), C_r \in (10000, 32500) \\ v_x \in (5,\ 25) \\ \tau_{\text{lag},f} \in (0.05,\ 0.25) \end{cases} \tag{6.11}$$

where the bounds for each parameter are defined by considering real vehicle driving and tire-road conditions.

From (6.1), (6.10), and aforementioned parameter set, the multiplicative model uncertainty $\Delta(s)$ is calculated as follows:

$$\Delta(s) = \frac{P(s) - P_n(s)}{P_n(s)}. \tag{6.12}$$

To prove the closed-loop stability against model uncertainty $\Delta(s)$, the small gain theorem is employed. In usual, the small gain theorem is used as a conservative stability check in cases where there is time-varying model uncertainty. According to the small gain theorem, a sufficient condition for closed-loop stability is given by

$$\|\Delta(j\omega)T(j\omega)\|_\infty < 1 \quad \forall\omega \in \Re \tag{6.13}$$

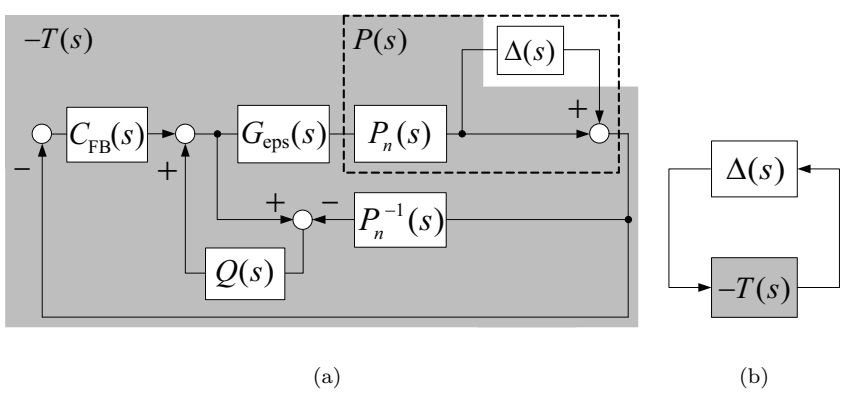

(a) (b)

Figure 6.3: Block diagram of closed loop control system. (a) Block diagram of closed loop control system with multiplicative model uncertainty. (b) Equivalent block diagram.

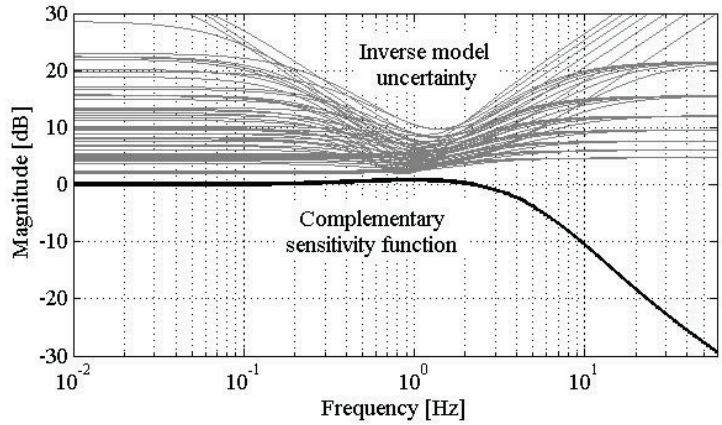

Figure 6.4: Frequency magnitude response for small gain theorem check.

where $T(j\omega)$ is the complementary sensitivity function and described as

$$T(j\omega) = \frac{P_n(j\omega)G_{\text{eps}}(j\omega)C_{\text{FB}}(j\omega) + Q(j\omega)}{1 + P_n(j\omega)G_{\text{eps}}(j\omega)C_{\text{FB}}(j\omega)}. \tag{6.14}$$

Note that as long as multiplicative model uncertainty $\Delta(j\omega)$ in the plant satisfies the inequality (6.13), the stability of closed-loop system is guaranteed. This is graphically illustrated in the magnitude Bode plot of Figure 6.4. We can confirm that the stability is guaranteed because the inequality (6.13) is satisfied, that is, magnitude of the complementary sensitivity function is below the magnitude of inverse model uncertainty all over the frequencies.

6.4 Experimental Verification

6.4.1 Experiment Setup

An in-wheel-motor-driven electric vehicle, as shown in Figure 2.16, was used to verify the performance and effectiveness of the proposed control system. Lateral tire force sensors, i.e., MSHub units, are installed in each wheel and an EPS system for realizing active front steering is available. In addition, the dSPACE AutoBox (DS1103), which consists of a power PC 750GX controller board running at 933 MHz, 16-channel A/D converter, and 8-channel D/A converter, are used for real-time data acquisition and control.

6.4.2 Experimental Results

To demonstrate the performance and effectiveness of the proposed motion controller, field tests were carried out with following driving conditions: 1) constant vehicle speed; 2) step steering command; 3) a proposed controller begins to work by enabling the manual control switch; 4) front-wheel driving mode.

Figure 6.5 shows the experimental results for the proposed motion controller. A controller begins to work when the control switch is turned on by a driver. That is, at $t = 20.7$ s, a proposed LTFC begins to work and this is confirmed from the result of control flag of LTFC (i.e., thick black line) shown in Figure 6.5(b). In addition, an EPS motor also begun to be controlled to realize robust lateral tire force control and its results are shown in Figure 6.5(a). A step steering input has been commanded by a driver at $t = 6.5$ s and an inner-loop EPS motor controller has worked for tracking the driver's steering command. The measured front steering angle, which is a control law, is equal to the sum of the each compensator including feed-forward, feedback compensator, and DOB, i.e., $\delta_f^\star = u_{\text{law}} = u_{\text{FF}} + u_{\text{FB}} + u_{\text{DOB}}$. Figure 6.5(b) and (c) represent the results of direct lateral tire force control using lateral tire force sensors. The measured front lateral tire force (i.e., thick red line) is relatively well matched the desired force trajectory (i.e., dotted blue line) while the control flag of LTFC (i.e., thick black line) is control-on-state. Figure 6.5(c) shows the tracking error defined as a difference between desired value and actual measured value (i.e., $F_f^{y\star} - F_f^y$). We can confirm that the tracking error at low frequency is within the specified tracking error limit (i.e., $< 10\%$). Although there exists a chattering-like error in experimental results due to: 1) noises in lateral tire force sensors; 2) non-homogenous road surface (i.e., dry asphalt with gravel), performances and effectiveness of the proposed LTFC can be confirmed by the results of Figure 6.5.

In addition, the effectiveness of the proposed LTFC in terms of the motion control viewpoint can also be verified from the results of vehicle motion sensors including yaw rate and lateral acceleration sensors. Figure 6.6(a), (b) and Figure 6.6(c), (d) represent the yaw rate and lateral acceleration which are directly measured by gyro sensor and accelerometer, respectively. Even though the yaw rate and lateral acceleration of the vehicle are not directly controlled (i.e., yaw rate and lateral acceleration are not controlled by sensor feedback), the measured values are

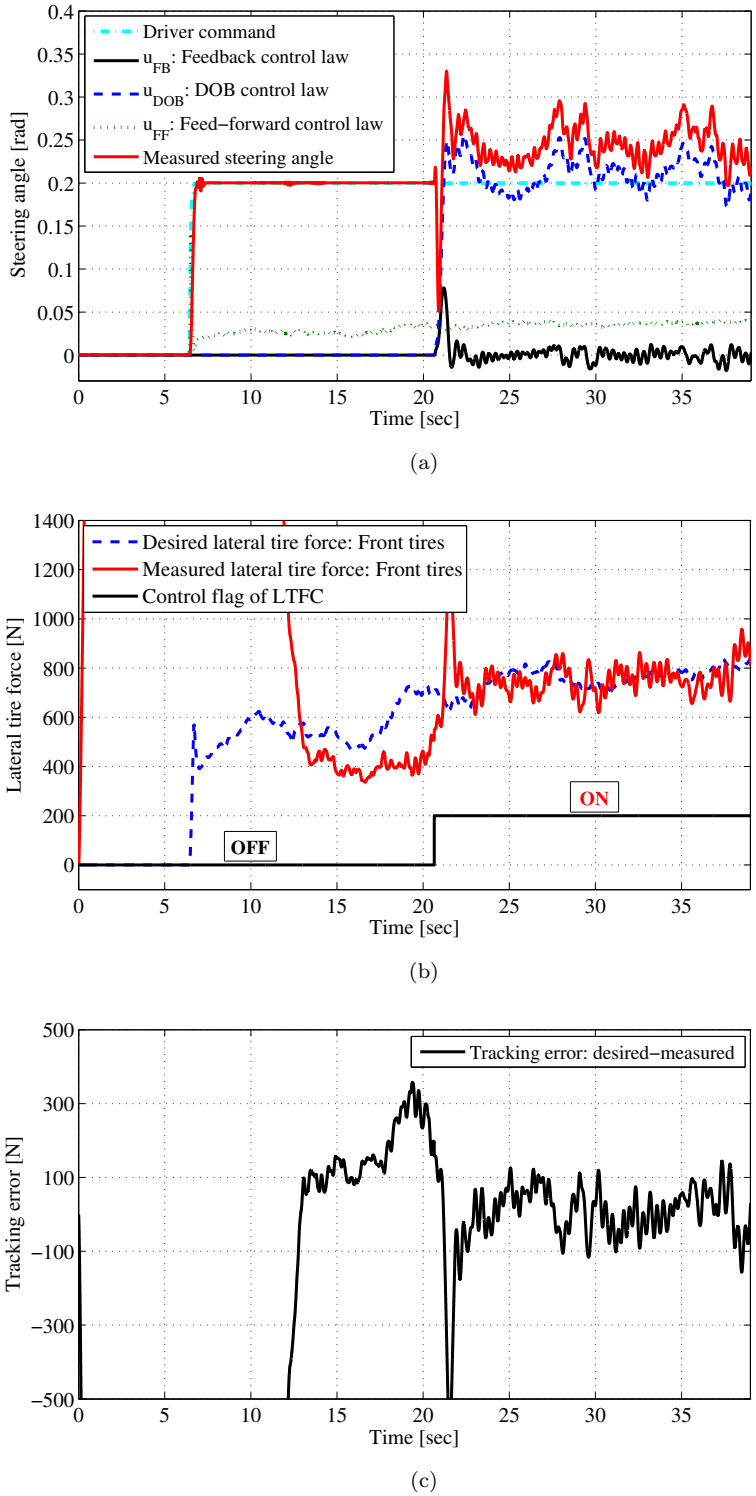

Figure 6.5: Experimental results for constant steering test on dry asphalt. (a) Control law: front steering angle, (b) Lateral tire force, (c) Tracking error.

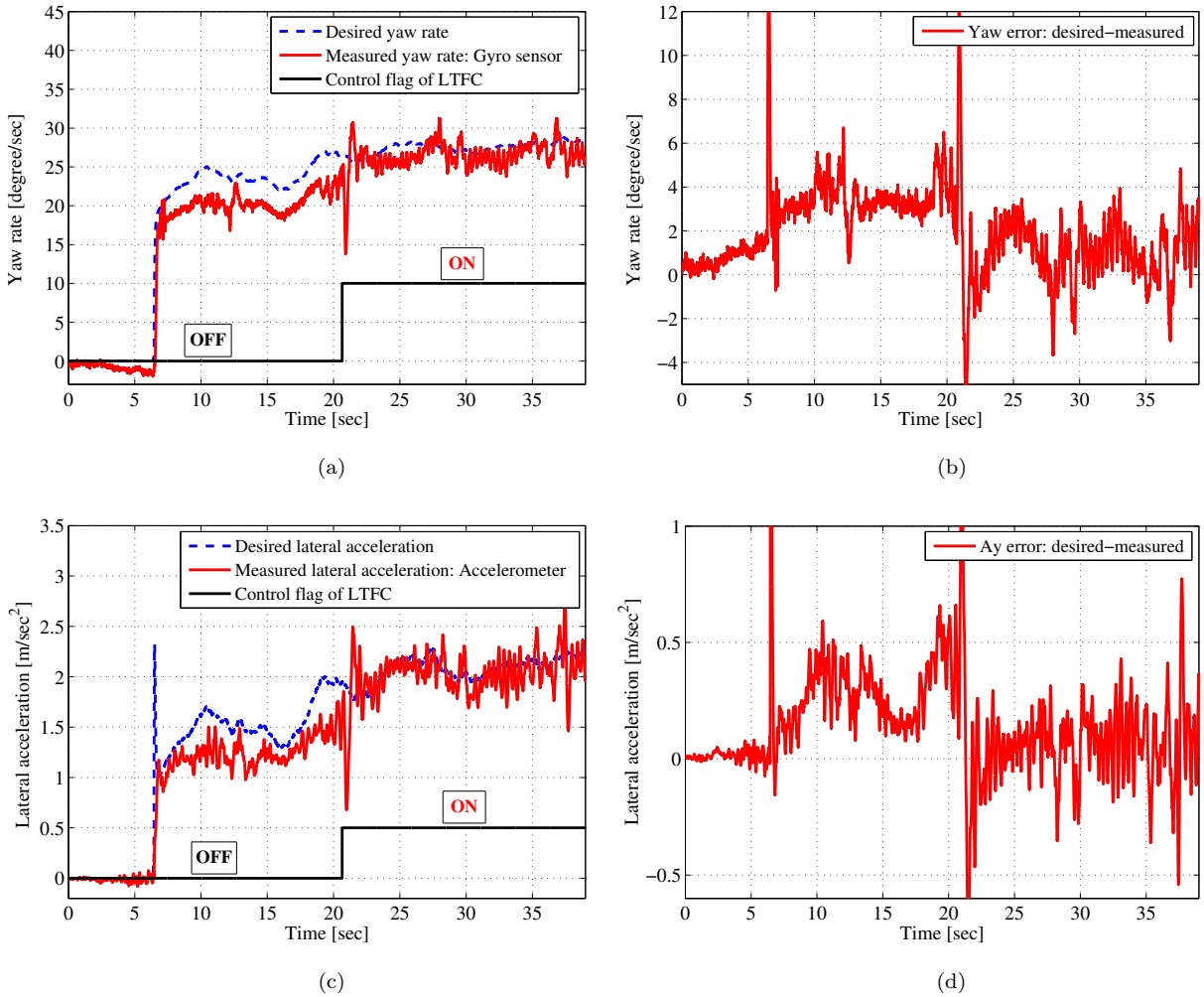

Figure 6.6: Experimental results. (a) Yaw rate. (b) Yaw rate error. (c) Lateral acceleration. (d) Lateral acceleration error.

well matched the desired values. Results of yaw rate and lateral acceleration errors shown in Figure 6.6(b) and (c) well illustrated the effect of a proposed LTFC to the lateral vehicle motion. Therefore, a proposed LTFC contributes to stabilization of the lateral vehicle motion by realizing the reference tire force tracking control. This new motion control scheme based on LTFC is an important contribution of this study.

Additional field tests were performed with the same driving conditions as what used in a test of Figure 6.5 so as to verify the effectiveness of a proposed LTFC in the critical driving situation (e.g., severe lateral motion, i.e., $|a_y| > 6$ m/s^2). Figure 6.7(a) and (b) show the front lateral tire forces controlled by the proposed LTFC at $v_x = 27$ km/h and $v_x = 35$ km/h, respectively.

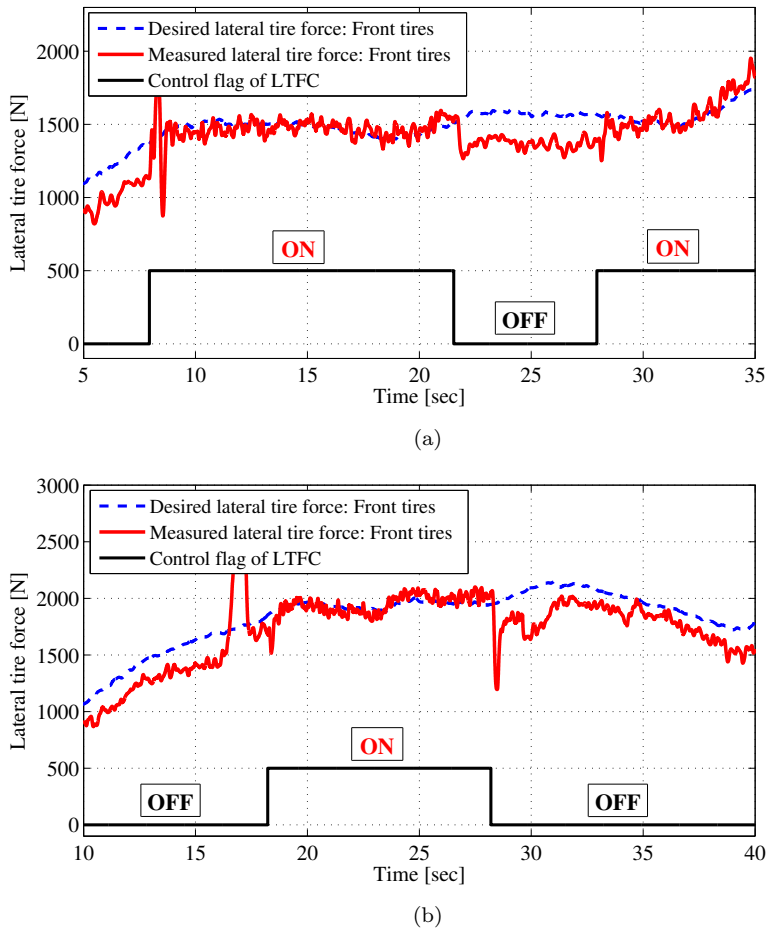

Figure 6.7: Experimental results for critical driving, e.g., driving with large lateral acceleration. (a) Result of a field test with $v_x = 27$ km/h, $\delta_{\text{cmd}} = 0.15$ rad, $|a_y|_{\max} = 5$ m/s^2. (b) Result of a field test with $v_x = 35$ km/h, $\delta_{\text{cmd}} = 0.15$ rad, $|a_y|_{\max} = 7$ m/s^2.

As shown in Figure 6.7(a), the lateral tire force that the vehicle generated followed the desired lateral tire force while the control flag of LTFC was activated. Figure 6.7(b) shows the similar results to Figure 6.7(a). However, from $t = 24$ s to $t = 28$ s, we can see the slightly increased tracking error, which is partly due to the nonlinear tire force characteristics called a lateral tire force saturation. Note that, as the tire slip angle continue to grow, the tire begins to saturate and reach a peak value; this area is commonly called nonlinear region of the tire curve. Even though the vehicle is in the critical situation, the proposed LTFC has successfully worked without a noticeable tracking error as shown in Figure 6.7.

Experimental results demonstrate that the proposed LTFC via active front steering is par-

ticularly useful if the front lateral tire forces are completely controllable by active front steering, i.e., up to the peak value of lateral tire force. For this reason, we have proposed the real-time algorithm for calculating the lateral tire force limit as shown in Section 4.3 and this contributes to avoiding the control action in the nonlinear tire region. Since the vehicle cornering state such as a tire slip angle is accurately estimated using cost-effective MSHub units (*Nam et al.*, 2012b,a), a proposed LTFC can be conditionally applied to vehicle motion control systems for improving the handling and cornering stability based on the estimated tire slip angle.

6.5 Overview on Disturbance Observer

Several techniques exists to incorporate disturbance rejection requirements in a linear controller design. Contrary to, for example the H-infinity controller design technique where only one degree of freedom is available to obtain both disturbance rejection and performance, a DOB adds a degree of freedom, thereby enabling a separate design of the disturbance rejection and the performance (*Lee and Tomizuka*, 1996; *Kim and Chung*, 2003; *Sabanovic and Ohnishi*, 2011). In general, the DOB is an effective method widely used to reject external disturbances or model uncertainties. DOB-controlled systems behave as defined nominal models, and therefore the DOB is often used as an inner-loop model following controller.

The performance of DOB dominantly depends on a frequency filter, called the Q-filter shown in Figure 6.8, as well as the nominal model of the plant. Figure 6.8 illustrates the general structure of a DOB for the SISO system, where u, u^*, d, y, and n denote the command input, control input, an external disturbance, the measurable output, and sensor noise, respectively. $P(s)$ represents the physical plant to be controlled. $P_n(s)^{-1}$ is the inverse of a nominal plant model, the purpose of which is to estimate the control input from the output y. It is assumed that the external disturbances d is simply added to the control input and the output of $P_n(s)^{-1}$ is the estimation of $u^* + d$ plus the effects of sensor noises as shown in Figure 6.8.

The estimated disturbance is fedback back into the system for rejection of the actual disturbance. However, the estimated disturbance cannot be directly used due to following reasons:

1. The inverse of the nominal plant model $P_n(s)^{-1}$ is not realizable, and

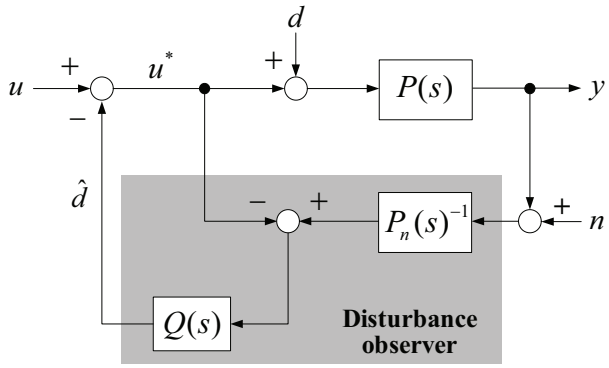

(a) Conventional disturbance observer.

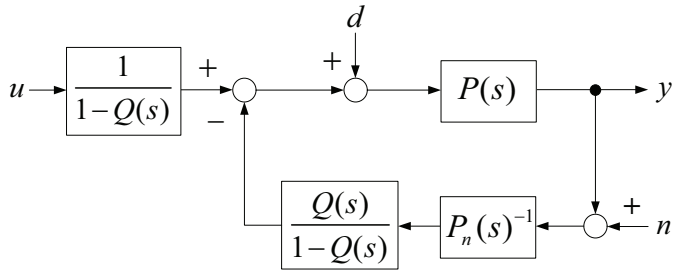

(b) Equivalent disturbance observer I.

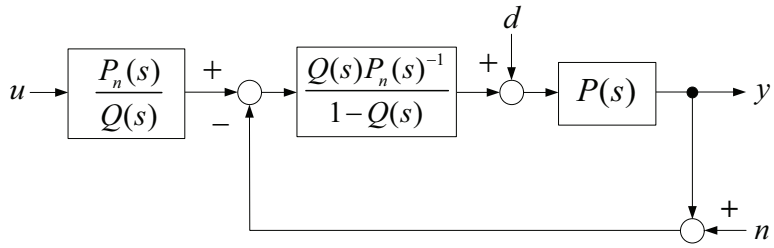

(c) Equivalent disturbance observer II.

Figure 6.8: Structure of disturbance observer.

2. The amplification of high frequency sensor noises degrades the performance.

These problems are remedied by adding a low-pass filter after the disturbance estimate, which is called Q-filter. The Q-filter, $Q(s)$ is selected such that $Q(s)P_n(s)^{-1}$ is realizable. That is, $P_n(s)^{-1}$ is not realizable by itself but that $Q(s)P_n(s)^{-1}$ can be made realizable by letting the relative degree of $Q(s)$ be equal to or greater that that of $P_n(s)^{-1}$. In addition, $Q(s)$ plays

the role of attenuating the effect of sensor noises. From the block diagram in Figure 6.8(a), the transfer functions from u, d, and n to the output y are expressed as

$$y = G_{yu}(s)u + G_{yd}(s)d + G_{yn}(s)n \tag{6.15}$$

where

$$G_{yu} = \frac{P(s)P_n(s)}{P_n(s) + Q(s)P(s) - Q(s)P_n(s)} \tag{6.16}$$

$$G_{yd} = \frac{P(s)P_n(s)(1 - Q(s))}{P_n(s) + Q(s)P(s) - Q(s)P_n(s)} \tag{6.17}$$

$$G_{yn} = \frac{P(s)Q(s)}{P_n(s) + Q(s)P(s) - Q(s)P_n(s)} \tag{6.18}$$

From (6.18)–(6.18), we can see that the design of a disturbance observer is dependent on $Q(s)$ which is the most significant parameter to determine disturbance rejection performance and robustness. Also, it is found that as $Q(s)$ approaches 1 at low frequencies, G_{yu} approaches $P_n(s)$ and G_{yd} approaches 0. As $Q(s)$ approaches 0 at hight frequencies, G_{yn} approaches 0. Figure 6.8(c) shows that DOB plays the role as a high gain inner-loop controller around the plant at frequencies where $Q(s) \approx 1$. Assuming that $P(s)$=$P_n(s)$, the sensitivity function $S(s)$ and complementary sensitivity function $T(s)$ are expressed with respect to the nominal plant model, i.e.,

$$S(s) = 1 - Q(s) \tag{6.19}$$

$$T(s) = Q(s) \tag{6.20}$$

A multiplicative uncertainty model is considered to discuss the robust stability of DOB. Suppose that the nominal plant model $P_n(s)$ is subjected to multiplicative model uncertainty, i.e.,

$$P(s) = P_n(s)\left[1 + \Delta(s)W(s)\right] \tag{6.21}$$

where $W(s)$ is a stable and proper transfer function of the model uncertainties, and $\Delta(s)$ is any arbitrary stable transfer function with bounded magnitude in the frequency domain, i.e., $\| \Delta(j\omega) \|_\infty \leq 1$. The main purpose of $\Delta(s)$ is to account for phase uncertainty and to act as a scaling factor on the magnitude of model uncertainty. Therefore, nonlinearities and time-varying factors can be covered by $\Delta(s)W(s)$, while $P_n(s)$ is a linear time-invariant system. Since the magnitude of $\Delta(j\omega)$ is bounded to one, i.e., $\| \Delta(j\omega) \|_\infty \leq 1$, the following inequality condition is easily verified.

$$\left| \frac{P(j\omega)}{P_n(j\omega)} - 1 \right| \leq |W(j\omega)| \quad \forall \omega \in \Re \tag{6.22}$$

Here, we can see that $|W(j\omega)|$ provides the model uncertainty bound. From this fact, the well-known robust stability theorem is applied such that the stability of the DOB loop is guaranteed for all possible model uncertainties. The DOB provides robust stability if and only if

$$\| W(j\omega)T(j\omega)) \|_\infty = \| W(j\omega)Q(j\omega)) \|_\infty < 1 \tag{6.23}$$

Therefore, $Q(s)$ should be designed such that (6.23) is satisfied.

6.6 Chapter Summary

This chapter has presented a new motion control scheme based on robust LTFC via active front steering. Since the vehicle cornering motion is dominantly governed by lateral forces acting on tires, the motion control based on direct tire force control can improve the cornering stability and maneuverability of the vehicle and the accurate prediction of the vehicle state can be achieved. Recently, cost-effective lateral tire force sensors, called MSHub units, were invented by NSK Ltd. and are now under development for practical applications to vehicle control systems. In this paper, a robust method for direct lateral tire force control is presented for practical applications to vehicle motion control systems using lateral tire force sensors. In order to achieve the robust control design, a DOB-based 2-DOF control method was employed and active front steering control via SbW was utilized for achieving the control law. The stability of the closed-loop control system is proved by using the small gain theorem. Finally, performance and effectiveness

of the proposed LTFC are verified by field tests. Through experimental results, it is confirmed that the vehicle motion control based on tire force-level control using cost effective lateral tire force sensors can improve the cornering stability and maneuverability. In addition, field tests in the critical cornering situation are performed and control performances of the proposed LTFC are demonstrated by experimental results.

CHAPTER VII

Conclusions and Open Issues

7.1 Conclusions

This thesis has presented novel vehicle state estimation and motion control methods using lateral tire force sensors, and has discussed the practical application of lateral tire force sensors to motion control systems for future electric vehicles. Moreover, this thesis investigates important technologies for improving the motion control systems of electric vehicles not only based on theoretical approaches to vehicle, tire dynamics and estimation, and control design, but also implementation on experimental electric vehicles in real-time. In this thesis, several advanced methods for robustly estimating the vehicle states and controlling the vehicle motion are proposed based on lateral tire force sensors. Major contributions of this thesis are as follows:

1. The development of novel algorithms for vehicle sideslip angle and roll angle estimation using lateral tire force sensors [Chapter III],

2. The development of real-time algorithms to estimate tire-road condition [Chapter IV],

3. The design of motion control algorithms based on a sideslip angle observer and adaptive feedforward control methodology [Chapter V],

4. The design of an advanced motion control system based on robust lateral tire force controller [Chapter VI],

5. The design of robust yaw stabilization control algorithm based on adaptive sliding mode control [Chapter VII], and

6. Experimental verification of the proposed estimation and control algorithms using an experimental electric vehicle.

In the remaining part of this section, details of the main contributions are described.

7.1.1 Advanced State Estimation Using Lateral Tire Force Sensors

Robust estimation of vehicle states such as vehicle sideslip angle and roll angle is a challenging issue in vehicle motion control applications like yaw stability control and roll stability control. In this thesis, novel methods for estimating vehicle sideslip angle and roll angle are proposed using lateral tire force sensors. For vehicle sideslip angle estimation, two estimation algorithms based on a RLS approach and an EKF technique are designed, respectively. For roll angle estimation, KF is designed using available sensor measurements and physical roll dynamics model. The effectiveness of proposed estimation methods is verified through field tests on an experimental electric vehicle. Experimental results demonstrate that the proposed estimation methods can accurately estimate the vehicle sideslip angle and roll angle. In short,

- Vehicle sideslip angle estimation based on RLS and KF/EKF approaches,
- Vehicle roll angle estimation based on RLS approach, and
- Performance verification and evaluation through field tests.

In addition, a real-time algorithm for calculating the lateral tire force limit was proposed and its effectiveness is verified through field tests.

7.1.2 Advanced Motion Control Using Lateral Tire Force Sensors

The robust design of motion controllers for vehicle stability enhancement is challenging due to nonlinear characteristics in vehicle and tire models, e.g., varying tire cornering stiffness with respect to road condition and tire force saturation. In this thesis, the two motion control algorithms are designed based on lateral tire force sensor application; 1) a motion control algorithm, based on vehicle sideslip angle estimation, is designed using 2-DOF control methodology for yaw rate and vehicle sideslip tracking control and an adaptive feed-forward control technique is applied for improving control performances, 2) a novel motion control algorithm based on direct tire

force control is designed. In this control algorithm, the real-time estimation of a critical vehicle state, i.e., a vehicle sideslip angle, is not required anymore. A robust control approach is applied in the design of the controllers for improved robustness to uncertainties in the vehicle and tire models. Moreover, a DOB is utilized to compensate for changes in the dynamic tire model as well as for mechanical disturbances in the actuators. Both control algorithms are implemented on an experimental electric vehicle with in-wheel motors and those control performances, e.g., yaw rate, vehicle sideslip angle tracking, and lateral tire force tracking ability, are verified through field tests. It is confirmed that proposed control algorithms based on lateral tire force sensors can contribute to improvement of the vehicle stability.

7.2 Open Issues

In this thesis, key technologies of vehicle motion control systems have been discussed. A variety of estimation and control algorithms using lateral tire force sensors, which is called MSHub units, have been developed and those effectiveness was verified. However, there remains the high possibility for future improvements. Remaining open issues include the following.

7.2.1 Robust Estimation of Tire-Road Conditions

Even though knowledge of the tire-road conditions is significantly important for vehicle active safety systems, estimating or direct measuring the tire-road condition, e.g., friction coefficient μ, is challenging because it is property of extreme phenomenon such as the tire skidding. To overcome these challenging problems, a variety of approaches to estimating tire-road conditions have been proposed in the literature. In this thesis, a real-time estimation algorithm, which is for estimating the tire-road condition in lateral direction, was developed and this algorithm has been used to constrain the desired vehicle responses. Considering that vehicle motion is governed by longitudinal tire force including driving/braking forces and lateral tire force acting on individual tires, estimation of tire-road condition in only lateral direction is not enough for applications to all driving situations. From this point, real-time estimation of longitudinal, vertical tire forces and lateral tire force measurement make it possible to estimate the tire-road conditions in both directions, i.e., longitudinal and lateral direction. Moreover, more reliable estimation of

individual tire-road condition (especially tire-road friction coefficient) can be realized by using all tire force information.

7.2.2 Practical Applications of Lateral Tire Force Sensors to Vehicle Control Systems: Sensor Noise Issue

In this thesis, lateral tire force sensors that can directly measure the lateral forces acting on each wheel were used to estimate vehicle states and to directly control the lateral tire force by feedback of the sensor measurements. As shown in Chapter VI, measured lateral tire forces contain relatively high-frequency noises which are caused due to effects of the sensor location. Since lateral tire force sensors, i.e., MSHub units, are installed into the wheels and the wheels are perturbed by road surface roughness effects, and consequently induces pulsations in the tire force measurements. These degrade the tracking performances of robust lateral tire force controllers. Therefore, more practical and sophisticated noise suppression techniques need to be studied.

7.2.3 Energy-Efficient Motion Control Based on Optimal Control Allocation

Over-actuated systems such as IWM-EV, in which the number of controllable actuators is greater than the degree of freedom, have challenging issues. Among them, the main challenge is how to handle the actuator redundancy and physical constraints at the same time. For example, in case of IWM-EVs used in this study, it has six controllable actuators including four in-wheel motors and front/rear EPS motors. To improve actuator efficiencies and vehicle safety, optimal control allocation scheme, which should be a feasible and practical method, can overcome the challenges and will become more and more widely applied to vehicle motion control systems.

APPENDIX

APPENDIX A

Robust Yaw Stability Control Based on Longitudinal Tire Force Control

A.1 Introduction of Yaw Stability Control

The purpose of yaw stability control is to prevent unintended vehicle behavior through active vehicle control and assist drivers in maintaining controllability and stability of vehicles. The main goal of most motion control systems is to control the yaw rate of the vehicles. In *Geng et al.* (2009), direct yaw moment control based on side slip angle estimation was proposed for improving the stability of IWM-EV. A fuzzy-rule-based control and sliding mode control algorithms for vehicle stability enhancement were proposed and evaluated through experiments (*Kim et al.*, 2008). A novel yaw stability control method based on robust yaw moment observer (YMO) design is presented and its practical effectiveness was verified through various field tests (*Fujimoto et al.*, 2005). Parameter uncertainties shown in a vehicle model and external disturbances acting on vehicles are compensated by the disturbance observer (*Umeno and Hori*, 1991; *Kim and Chung*, 2003) and yaw stabilization is realized through yaw rate feedback control. In this chapter, a sliding model control method with parameter adaptation is employed for robust yaw stabilization of electric vehicles. The proposed control structure employs a reference generator, which is designed from driver's commands, a sliding mode controller, and parameter adaptation laws. The sliding mode control technique is well-known robust control methodology particularly suitable

for dealing with nonlinear systems with model uncertainties and disturbances like the considered vehicle systems (*Chung and Yi*, 2006; *Song and Che*, 2009). Since the vehicles operate under wide range of road conditions and speed, the controller should provide robustness against varying parameters and undesired disturbances all over the driving regions. In *Zhou and Liu* (2010), a cascade vehicle yaw stability control system was designed with the sliding mode and backstepping control approaches. In *Canale et al.* (2008), a vehicle yaw controller via second-order sliding mode technique was designed to guarantee robust stability in front of disturbances and model uncertainties.

To compensate the disturbances and model uncertainties existing in control law, the adaptive sliding mode control method is applied. By combining with the defined sliding surface, a sliding mode controller is re-designed such that the state (i.e., yaw rate) is moved from the outside to inside of the region, and finally, it remains inside the region even though there are model uncertainties and disturbances, which can be estimated and then rejected by adaptation law.

In order to verify the control performances, experiments are performed using IWM-EV.

A.2 Yaw Dynamics for Control Design

In this section, a yaw dynamic equation is derived for the purpose of yaw stabilization controller design.

From (2.14), (2.27), (2.28), and small angle approximation (i.e., $\sin\delta_f \approx 0$ and $\cos\delta_f \approx 1$), the yaw dynamic equation is obtained as

$$\begin{aligned} I_z\dot{\gamma} &= l_f F_f^x \sin\delta_f + l_f F_f^y \cos\delta_f - l_r F_r^y + M_z + M_d \\ &\approx l_f F_f^y - l_r F_r^y + M_z + M_d \\ &= -\frac{2(l_f^2 C_f + l_r^2 C_r)}{v_x}\gamma + 2 l_f C_f \delta_f + M_z - 2\beta(l_f C_f - l_r C_r) + M_d \end{aligned} \tag{A.1}$$

where M_d is the yaw moment disturbance which may be caused by unstable road condition or side wind effects etc., a yaw moment term generated by vehicle sideslip angle, i.e., $-2\beta(l_f C_f - l_r C_r)$, is also considered as a disturbance.

Vehicle yaw dynamics model is perturbed by tire-road conditions, especially road friction

coefficient μ. For example, tire cornering stiffness C_f and C_r in (A.1) varies with respect to a road friction coefficient and these can be expressed as

$$C_f = C_{fn} + \Delta C_f, \tag{A.2}$$

$$C_r = C_{rn} + \Delta C_r \tag{A.3}$$

where C_{fn}, C_{rn} are nominal values which are commonly chosen as values for dry asphalt, and ΔC_f, ΔC_r are parameter variations which have a physical bound, respectively.

From (A.1), (A.2), and (A.3), a yaw dynamics equation is represented as

$$\begin{aligned} I_z\dot{\gamma} = &-\frac{2(l_f^2 C_{fn} + l_r^2 C_{rn})}{v_x}\gamma + 2l_f C_{fn}\delta_f + M_z \\ &- \frac{2(l_f^2 \Delta C_f + l_r^2 \Delta C_r)}{v_x}\gamma + 2l_f \Delta C_f \delta_f - 2\beta(l_f C_f - l_r C_r) + M_d \end{aligned} \tag{A.4}$$

Here, $\bar{M}_d$ is newly defined as a lumped yaw moment disturbance including external disturbances and unmeasurable moment terms, and parameter perturbation terms,

$$\bar{M}_d = -\frac{2(l_f^2 \Delta C_f + l_r^2 \Delta C_r)}{v_x}\gamma + 2l_f \Delta C_f \delta_f - 2\beta(l_f C_f - l_r C_r) + M_d \tag{A.5}$$

Assumption: The lumped disturbance $\bar{M}_d(t)$, which varies with tire-road condition and vehicle parameters, is bounded and satisfy the following inequality condition.

$$\|\bar{M}_d(t)\| \leq \Upsilon \tag{A.6}$$

where Υ is the upper bound of the lumped disturbance.

Consequentially, yaw dynamics equation (A.4) is expressed as a following equation that has two inputs and one output,

$$I_z\dot{\gamma} \ = -\frac{2B_n}{v_x(t)}\gamma + 2l_f C_{fn}\delta_f + M_z + \bar{M}_d \tag{A.7}$$

where B_n is defined as a yaw damping coefficient which varies with vehicle speed and tire-road condition.

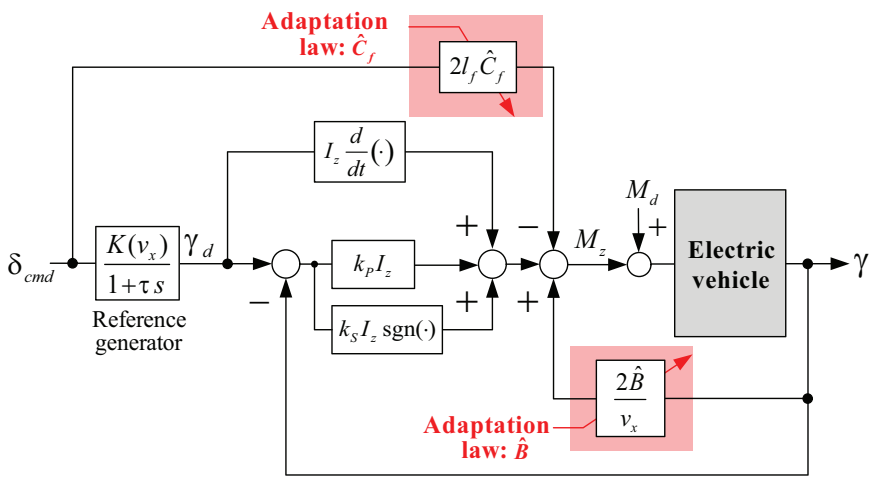

Figure A.1: Block diagram of an adaptive sliding mode controller.

A.3 Design of Adaptive Sliding Mode Controller

A.3.1 Overall Control Structure

The proposed control system is depicted in Figure A.1. A reference generator makes a desired yaw rate γ_d from driver's steering command δ_{cmd} and vehicle speed v_x which are explained in Section 5.3. The feedback controller is designed to make yaw moment to compensate yaw rate tracking error (i.e., $\gamma_d - \gamma$) based on the standard sliding mode control methodology. For treating model uncertainties and disturbances existing in a feedback control law, parameters in a designed sliding mode control law are updated according to adaptation laws. The external input M_d accounts for yaw moment disturbance caused by lateral wind, unbalanced road conditions, and unbalanced tire pressure,etc. With well-tuned control parameters, a proposed controller contributes to keeping the vehicle yaw rate following its target commanded by the driver.

A.3.2 Sliding Mode Control

It is well known that sliding mode control is a robust control method to stabilize nonlinear and uncertain systems which have attractive features to keep the systems insensitive to the uncertainties on the sliding surface (*Slotine and Li*, 1991). The conventional sliding mode control design approach consists of two steps. First, a sliding surface is designed such that the system trajectory along the surface acquires certain desired properties. Then, a discontinuous control

is designed such that the system trajectories reach the sliding surface in finite time. A sliding mode control as a general design technique for control systems has been well established, the advantages of a sliding model control method are:

1. fast response and good transient performance,
2. its robustness against a large class of perturbations or model uncertainties, and
3. the possibility of stabilizing some complex nonlinear systems which are difficult to stabilize by continuous state feedback laws.

Based on aforementioned advantages, sliding mode control has been employed to vehicle control systems (*Canale et al.*, 2008; *Zhou and Liu*, 2010; *Amodeo et al.*, 2010). As usual in the sliding mode control technique, the control forces the system evolution on a certain surface which guarantees the achievement of the control requirements. In order to achieve control objective, i.e., $\lim_{t\to\infty}\mathrm{S}(t) = 0$, sliding surface $\mathrm{S}(t)$ is defined as

$$\mathrm{S} \;=\; \gamma - \gamma_d \tag{A.8}$$

Here we can see that the sliding condition $\mathrm{S}(t) = 0$ means a zero tracking error.

By designing a satisfactory dynamics feedback control law, the trajectory of the closed-loop system can be driven on the sliding surface (A.8) and evolve along it, and yaw stabilization can be achieved. In order to achieve control requirements, a following reaching condition to be satisfied is designed as

$$\dot{\mathrm{S}} \;=\; -k_P\mathrm{S} - k_S \cdot \mathrm{sgn}(\mathrm{S}) \tag{A.9}$$

where the $k_P > 0$ is a control parameter which determines the convergence rate of a tracking error, the $k_S > 0$ is a control parameter which should be tunned according to bound of lumped disturbances $\bar{M}_d$.

From (A.1), (A.8), and (A.9), we can apply the standard sliding mode control method (*Slotine and Li*, 1991) and thereby the following control law can be obtained

$$M_z(t) \;=\; I_z\dot{\gamma_d}(t) + \frac{2B_n}{v_x(t)}\gamma(t) - 2l_fC_{fn}\delta_f(t) - k_PI_z\mathrm{S} - k_SI_z \cdot \mathrm{sgn}(\mathrm{S}). \tag{A.10}$$

We can prove that the sliding mode control law (A.10) makes the closed-loop control system asymptotically stable by introducing following positive definite Lyapunov function

$$V \;=\; \frac{1}{2}\mathrm{S}^2. \tag{A.11}$$

The time derivative of (A.11) is

$$\begin{aligned}\dot{V} = \mathrm{S}\dot{\mathrm{S}} \;&=\; \mathrm{S}(\dot{\gamma} - \dot{\gamma}_d) = \mathrm{S}\left[-\frac{2B_n}{I_zv_x}\gamma \;+\; \frac{2l_fC_{fn}\delta_f}{I_z} + \frac{M_z}{I_z} - \dot{\gamma_d}\right] \\ &=\; \mathrm{S}[-k_P\mathrm{S} - k_S \cdot \mathrm{sgn}(\mathrm{S})] \;= -k_P\mathrm{S}^2 - k_S|\mathrm{S}| \;< 0.\end{aligned} \tag{A.12}$$

Thus, the control objective, i.e., $\mathrm{S}(t) \to 0$ as $t \to \infty$, can be achieved by the control law (A.10).

Remark 1: In (A.10), the sliding mode switching gain k_S is selected considering uncertainty and disturbance bound. From assumption (A.6), k_S should be determined by considering the disturbance bound. Moreover, the maximum k_S which can be selected is limited by the maximum torque that an in-wheel motor generates. By properly tuning k_P and k_S, the chattering in control law is also reduced.

A.3.3 Sliding Mode Control with Parameter Adaptation Law

For treating the disturbance and inertia uncertainty existing in the control law (A.10), adaptive control method is a natural choice and has been widely applied. Combing with the defined sliding surface, a sliding mode controller can be designed such that the system state is moved from the outside to the inside of the region, and finally remains inside the region in spite of the uncertainty and disturbance which can be estimated and then rejected under the help of adaptive

law. Thus, based on above analysis, the control law (A.10) is modified as

$$M_z(t) \;=\; I_z\dot{\gamma_d}(t) + \frac{2\hat{B}}{v_x(t)}\gamma(t) - 2l_f\hat{C}_f\delta_f(t) - k_P I_z \mathrm{S} - k_S I_z \cdot \mathrm{sgn}(\mathrm{S}) \tag{A.13}$$

where the adaptation law for the estimated parameter $\hat{B}$ and $\hat{C}_f$ are chosen as

$$\dot{\hat{B}}(t) \;=\; -\frac{2k_1}{I_z v_x(t)}\gamma(t)\mathrm{S} - \eta_1 k_1 \tilde{B} \tag{A.14}$$

$$\dot{\hat{C}}_f(t) \;=\; -\frac{2l_f k_2}{I_z}\delta_f(t)\mathrm{S} - \eta_2 k_2 \tilde{C}_f. \tag{A.15}$$

Here $\tilde{B} = \hat{B}(t) - B$, $\tilde{C}_f = \hat{C}_f(t) - C_f$, k_1 and k_2 are adaptation gains which determine the update rate, η_1 and η_2 are positive constant values.

Remark 2: The main objective of parameter adaptation is to compensate parameter uncertainty and disturbance which varies with tire-road conditions. The adaptation law (A.14) and (A.15) consist of a tracking error (i.e., $\mathrm{S}(t)$) correction term.

Theorem. Considering vehicle yaw dynamics with designed sliding surface, the trajectory of the closed-loop control system can be driven on to the sliding surface $\mathrm{S}(t) = 0$ with the proposed adaptive control law and adaptation update law, and finally converge to the pre-defined reference trajectory.

Proof: Consider the following positive definite Lyapunov function:

$$V \;=\; \frac{1}{2}\mathrm{S}^2 + \frac{1}{2k_1}\tilde{B}^2 + \frac{1}{2k_2}\tilde{C_f}^2. \tag{A.16}$$

The time derivative of (A.16) is as follows:

$$\begin{aligned} \dot{V} \;&=\; \mathrm{S}\dot{\mathrm{S}} + \frac{1}{k_1}\tilde{B}\dot{\hat{B}} + \frac{1}{k_2}\tilde{C}_f\dot{\hat{C}}_f \\ &=\; \mathrm{S}\left[\frac{2\gamma}{I_z v_x}\tilde{B} - \frac{2l_f\delta_f}{I_z}\tilde{C}_f - k_P\mathrm{S} - k_S \cdot \mathrm{sgn}(\mathrm{S})\right] + \frac{1}{k_1}\tilde{B}\dot{\hat{B}} + \frac{1}{k_2}\tilde{C}_f\dot{\hat{C}}_f. \end{aligned} \tag{A.17}$$

With the adaptation law, this can be rewritten as follows:

$$\begin{aligned}
\dot{V} &= \mathrm{S}\dot{\mathrm{S}} + \frac{1}{k_1}\tilde{B}\dot{\hat{B}} + \frac{1}{k_2}\tilde{C}_f\dot{\hat{C}}_f \\
&= \mathrm{S}\left[\frac{2\gamma}{I_z v_x}\tilde{B} - \frac{2l_f\delta_f}{I_z}\tilde{C}_f - k_P\mathrm{S} - k_S\cdot\mathrm{sgn}(\mathrm{S})\right] + \frac{1}{k_1}\tilde{B}\left(-\frac{2k_1}{I_z v_x}\gamma\mathrm{S} - \eta_1 k_1\tilde{B}\right) \\
&\quad + \frac{1}{k_2}\tilde{C}_f\left(-\frac{2l_f k_2}{I_z}\delta_f(t)\mathrm{S} - \eta_2 k_2\tilde{C}_f\right) \\
&= -k_P\mathrm{S}^2 - k_S|\mathrm{S}| - \eta_1\tilde{B}^2 - \eta_2\tilde{C}_f^2 < 0.
\end{aligned} \tag{A.18}$$

This shows that the tacking error $\mathrm{S}(t)$ asymptotically converges to zero and the yaw stabilization is achieved.

Remark 3: The control parameters k_P and k_S in control law (A.10) play a important role in control system. These parameters determine the convergence rate of the sliding surface. It is noted that a larger k_P will force the yaw rate to converge to the desired yaw rate trajectory with a high speed. However, in practice, a compromise between the response speed and control input should be made. Since a too big k_P will require a very high control input, which is always bounded in reality. Therefore, the control parameter k_P can not be selected too large.

Remark 4: The control law (A.10) is discontinuous when crossing the sliding surface $\mathrm{S}(t) = 0$, which may lead to the undesirable chattering problem due to the measurement noise and some actuator delay. This problem can be eliminated by replacing a discontinuous switching function (i.e., sgn(S)) with a saturation function sat(S) with the boundary layer thickness Φ as the continuous approximation of a signum function

$$\mathrm{sgn}(\mathrm{S}) \approx \mathrm{sat}\left(\frac{\mathrm{S}}{\Phi}\right) = \begin{cases} \dfrac{\mathrm{S}}{\Phi}, & \text{if } \left|\dfrac{\mathrm{S}}{\Phi}\right| < 1 \\ \mathrm{sgn}\left(\dfrac{\mathrm{S}}{\Phi}\right), & \text{otherwise} \end{cases} \tag{A.19}$$

Thus, this offers a continuous approximation to the discontinuous sliding mode control law inside the boundary layer and guarantees the motion within the neighborhood of the sliding surface.

By applying the saturation function instead of the signum function, the chattering phe-

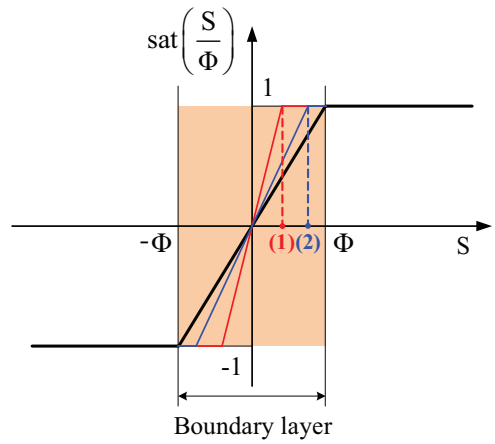

Figure A.2: Saturation function, sat $\left(\frac{S}{\Phi}\right)$. (1) Boundary layer $\Phi = 0.05$. (2) Boundary layer $\Phi = 0.067$.

nomenon can be decreased, but the tracking performance is deteriorated. By adjusting the thickness of the boundary layer, the chattering phenomenon and the tracking error can be traded off. That is, if the thickness of the boundary layer is close to zero, then the controller acts like the sliding mode controller with a signum function, which shows more chattering and less tracking error. On the contrary, if the thickness of the boundary layer is large, then the chattering phenomenon disappears but the tracking performance is much deteriorated.

A.4 Experimental Verification

The proposed adaptive sliding mode controller was implemented on the experimental IWM-EV shown in Figure 2.16.

To demonstrate the performance and effectiveness of the proposed adaptive sliding mode controller, field tests were carried out with following driving conditions:

1. constant vehicle speed, e.g., $v_x = 35$ km/h,
2. step steering command, e.g., $\delta_{\text{cmd}} = 0.15$ rad,
3. a proposed controller begins to work by enabling the manual control switch,
4. front-wheel driving mode, and
5. dry asphalt.

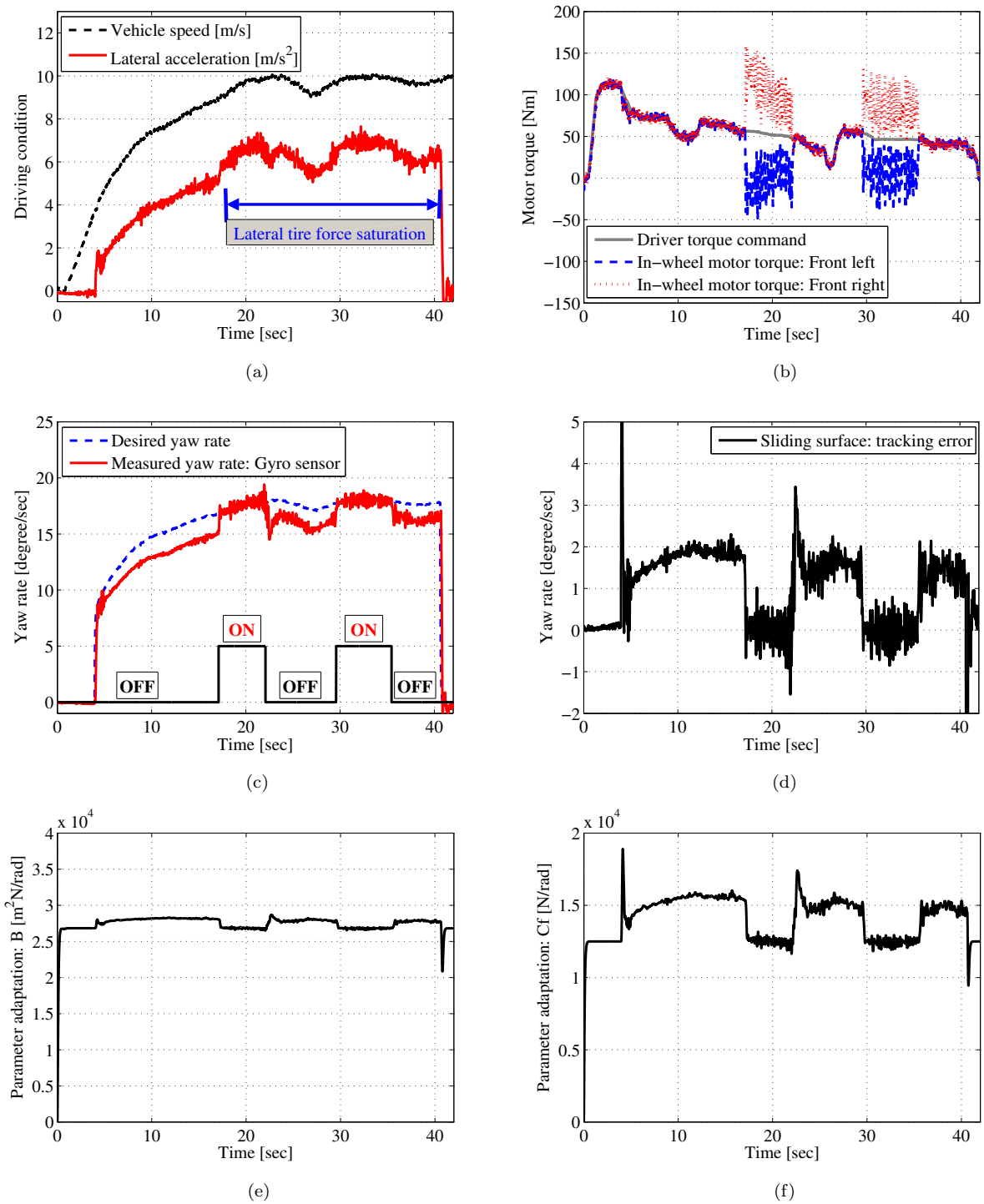

Figure A.3: Experimental results of a step steering (i.e., $\delta_{\text{cmd}} = 0.15$ rad) test at $v_x = 35$ km/h on dry asphalt: Boundary layer $\Phi = 0.067$. (a) Driving condition. (b) Control motor torque. (c) Yaw rate. (d) Sliding surface: tracking error. (e) Estimated parameter: $\hat{B}$. (f) Estimated parameter: $\hat{C}_f$.

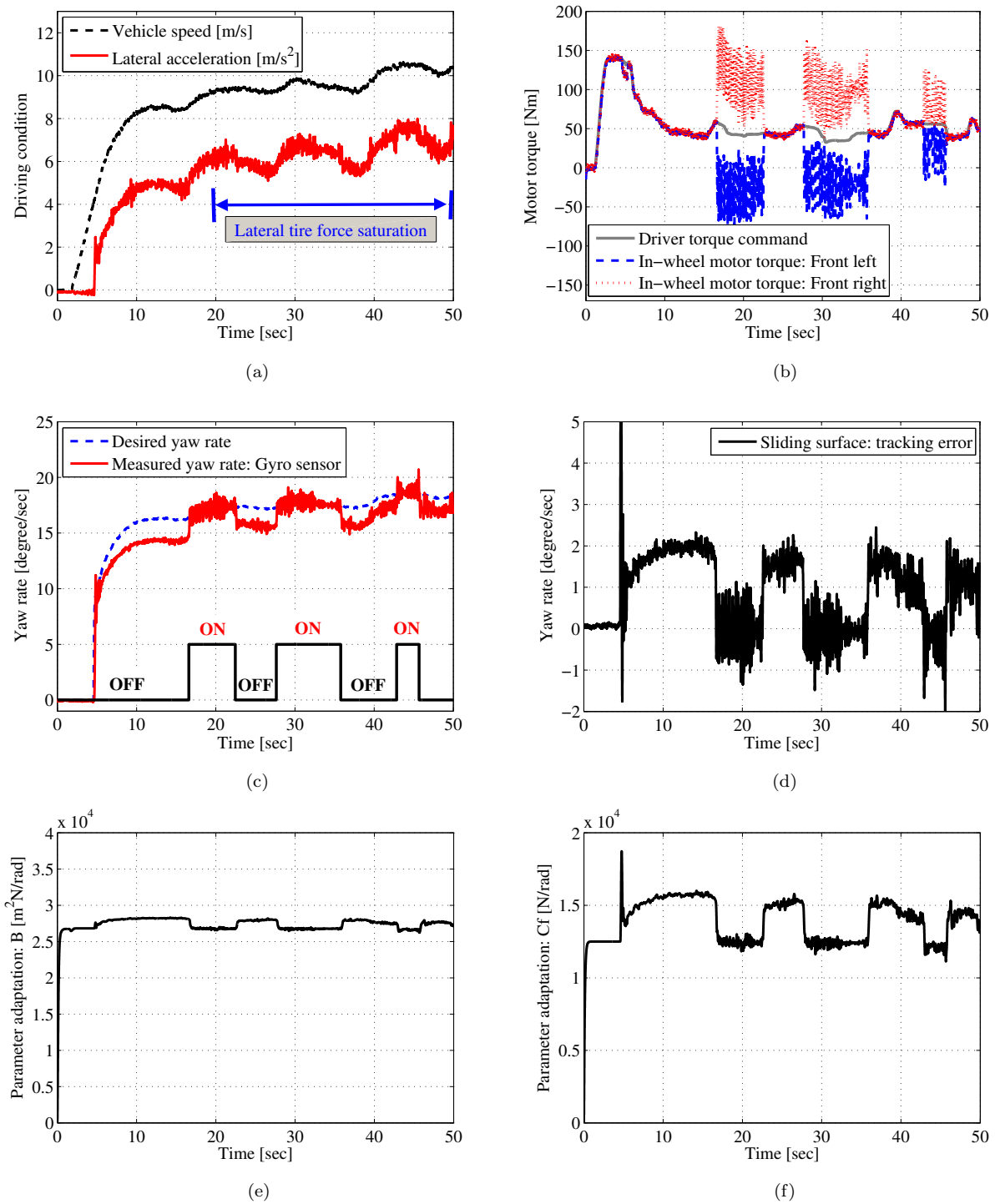

Figure A.4: Experimental results of a step steering (i.e., $\delta_{\text{cmd}} = 0.15$ rad) test at $v_x = 35$ km/h on dry asphalt: Boundary layer $\Phi = 0.05$. (a) Driving condition. (b) Control motor torque. (c) Yaw rate. (d) Sliding surface: tracking error. (e) Estimated parameter: $\hat{B}$. (f) Estimated parameter: $\hat{C}_f$.

Figure A.3 and Figure A.4 show the experimental results for the proposed adaptive sliding mode controller. A controller begins to work when the control switch [see the thick black line in Figure A.3(c)] is turned on by a driver. A step steering input has been commanded by a driver at t = 3.5 sec and an steering motor controller has worked for tracking the driver's steering command. Figure A.3(a) shows the driving conditions including vehicle speed and lateral acceleration. The control law, which is generated from the proposed controller, is allocated to front left and right motors. Measured torques of front left and right in-wheel motors are illustrated in Figure A.3(b). Figure A.3(c) represents the results for yaw rate control. We can confirm that the proposed adaptive sliding mode controller stabilizes the vehicle motion from the result of Figure A.3(a). At $t = 17$ sec, the controller begun to work and an actual vehicle yaw rate well tracks the desired yaw rate without a noticeable tracking error as shown in Figure A.3(d). Even though the vehicle is in critical driving situation [see the result of lateral acceleration in Figure A.3(a)], the proposed adaptive sliding mode controller shows the good tracking ability. Figure A.3(e) and (f) shows the results for parameter adaptation by (A.14) and (A.15). With the same driving conditions and somewhat narrowed boundary layer (i.e., $\Phi = 0.05$), experiments are performed for confirming the influences of the boundary layer. By comparing results of Figure A.3 ($\Phi = 0.069$) and Figure A.4 ($\Phi = 0.05$), we can confirm that the chattering phenomenon can be decreased by adjusting the boundary layer. In addition, chattering reduction by using adjustable boundary layer is confirmed through results of Figure A.5.

In short, effectiveness of the proposed adaptive sliding mode controller is verified through experimental results of Figure A.3 and A.4. The sliding surface $\mathrm{S}(t)$, which indicates a tracking error of the yaw rate, has converged to zero as shown in A.3(c), A.4(c). Through theoretical and experimental verification, it is confirmed that tracking performances and stability of the proposed adaptive sliding mode controller are achieved.

A.5 Summary

Appendix has presented an adaptive sliding mode control method for yaw stability enhancement of in-wheel-motor-driven electric vehicles. The proposed control structure is composed of a reference generator, a feedback controller (i.e., sliding mode controller), and parameter adapta-

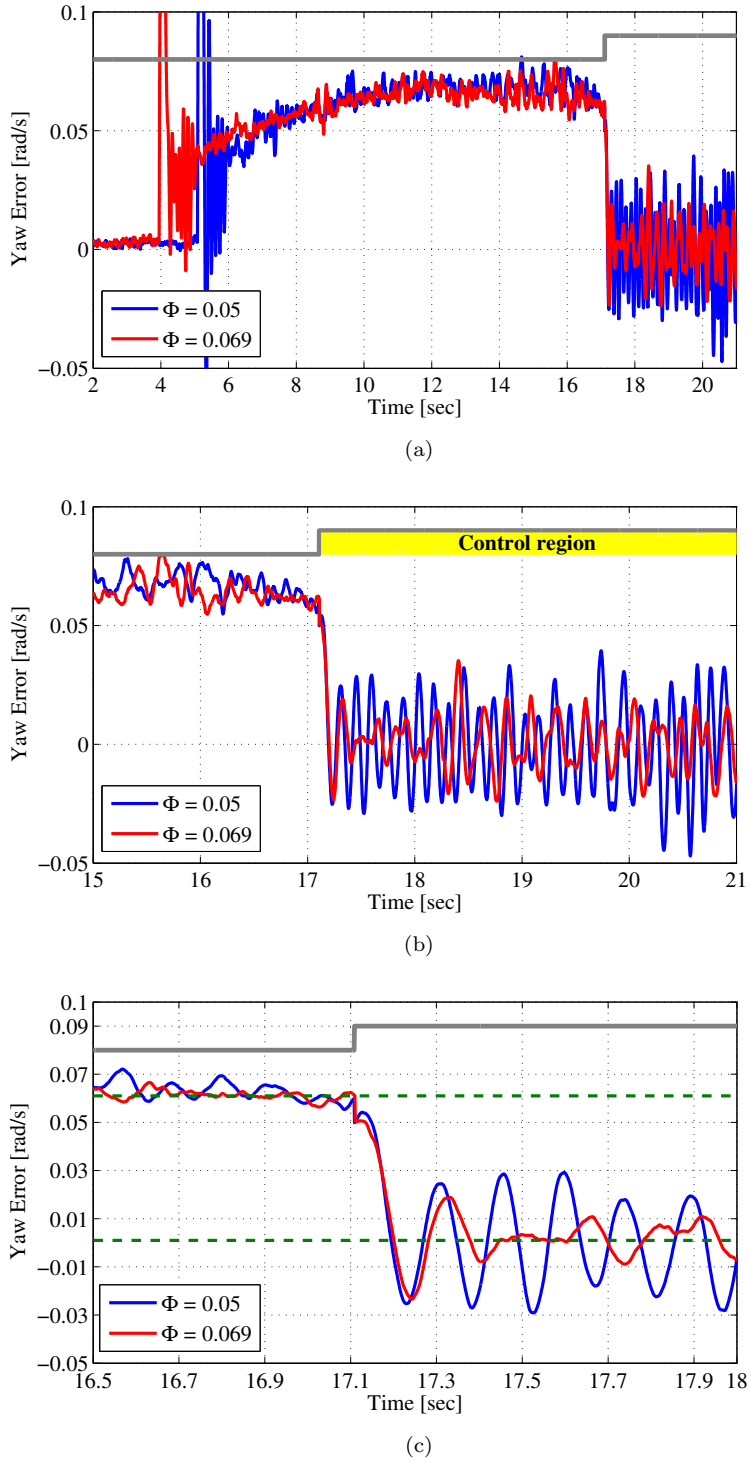

Figure A.5: Effect of boundary layer on chattering reduction. (a) Sliding surface: tracking error. (b) Sliding surface: tracking error (zoomed). (c) Sliding surface: tracking error (zoomed).

tion laws. The sliding mode control method, that is capable of guaranteeing robust stability in the presence of model uncertainties and disturbances, is used to stabilize the vehicle yaw motion. Field tests using an experimental electric vehicle are carried out and its effectiveness is verified. In future works, optimal motor torque distribution methods are presented and incorporated into the proposed adaptive sliding mode controller. Moreover, we will do comparison study on disturbance observer and sliding mode control for enhancement of robustness.

BIBLIOGRAPHY

BIBLIOGRAPHY

Abe, M., and W. Manning (2009), *Vehicle Handling Dynamics: Theory and Application*, Butterworth Heinemann, Butterworth-Heinemann/Elsevier.

Abe, M., Y. Kano, K. Suzuki, Y. Shibahata, and Y. Furukawa (2001), Side-slip control to stabilize vehicle lateral motion by direct yaw moment, *JSAE Review*, *22*(4), 413–419, doi: 10.1016/S0389-4304(01)00124-2.

Ackermann, J. (2002), *Robust Control: The Parameter Space Approach (Communications and Control Engineering)*, 2nd ed., Springer.

Ahn, C., H. Peng, and H. E. Tseng (2011), Robust estimation of road frictional coefficient, *IEEE Transactions on Control Systems Technology*, *PP*(99), 1, doi:10.1109/TCST.2011.2170838.

Amodeo, M., A. Ferrara, R. Terzaghi, and C. Vecchio (2010), Wheel slip control via second-order sliding-mode generation, *IEEE Transactions on Intelligent Transportation Systems*, *11*(1), 122–131, doi:10.1109/TITS.2009.2035438.

Ando, N., and H. Fujimoto (2010), Yaw-rate control for electric vehicle with active front/rear steering and driving/braking force distribution of rear wheels, in *Advanced Motion Control, 2010 11th IEEE International Workshop on*, pp. 726–731, doi:10.1109/AMC.2010.5464040.

Antonov, S., A. Fehn, and A. Kugi (2011), Unscented kalman filter for vehicle state estimation, *Vehicle System Dynamics*, *49*(9), 1497–1520, doi:10.1080/00423114.2010.527994.

Aoki, Y., T. Uchida, and Y. Hori (2005), Experimental demonstration of body slip angle control based on a novel linear observer for electric vehicle, in *Industrial Electronics Society, 2005. IECON 2005. 31st Annual Conference of IEEE*, p. 6 pp., doi:10.1109/IECON.2005.1569320.

Baffet, G., A. Charara, and G. Dherbomez (2007a), An observer of tire-road forces and friction for active security vehicle systems, *IEEE/ASME Transactions on Mechatronics*, *12*(6), 651–661, doi:10.1109/TMECH.2007.910099.

Baffet, G., A. Charara, and D. Lechner (2007b), Experimental evaluation of a sliding mode observer for tire-road forces and an extended kalman filter for vehicle sideslip angle, in *2007 46th IEEE Conference on Decision and Control*, pp. 3877–3882, doi:10.1109/CDC.2007.4434162.

Baffet, G., A. Charara, and D. Lechner (2009), Estimation of vehicle sideslip, tire force and wheel cornering stiffness, *Control Engineering Practice*, *17*(11), 1255–1264, doi: 10.1016/j.conengprac.2009.05.005.

Bakker, E., H. Pacejka, and L. Nyborg (1987), *Tyre Modelling for Use in Vehicle Dynamics Studies*, Society of Automotive Engineers.

Bakker, E., H. Pacejka, and L. Lidner (1989), A new tire model with an application in vehicle dynamics studies, *PROGRESS IN TECHNOLOGY*, *57*, 101–113.

Bevly, D., J. Ryu, and J. Gerdes (2006), Integrating ins sensors with gps measurements for continuous estimation of vehicle sideslip, roll, and tire cornering stiffness, *IEEE Transactions on Intelligent Transportation Systems*, *7*(4), 483–493, doi:10.1109/TITS.2006.883110.

Canale, M., L. Fagiano, A. Ferrara, and C. Vecchio (2008), Vehicle yaw control via second-order sliding-mode technique, *IEEE Transactions on Industrial Electronics*, *55*(11), 3908–3916, doi: 10.1109/TIE.2008.2003200.

Chan, C. (1993), An overview of electric vehicle technology, *Proceedings of the IEEE*, *81*(9), 1202–1213, doi:10.1109/5.237530.

Chan, C. (2002), The state of the art of electric and hybrid vehicles, *Proceedings of the IEEE*, *90*(2), 247–275, doi:10.1109/5.989873.

Cho, W., J. Yoon, S. Yim, B. Koo, and K. Yi (2010), Estimation of tire forces for application to vehicle stability control, *IEEE Transactions on Vehicular Technology*, *59*(2), 638–649, doi: 10.1109/TVT.2009.2034268.

Chung, T., and K. Yi (2006), Design and evaluation of side slip angle-based vehicle stability control scheme on a virtual test track, *IEEE Transactions on Control Systems Technology*, *14*(2), 224–234, doi:10.1109/TCST.2005.863649.

CNNMoney (2012), General Motors announces Chevy Spark fully electric car, `http://money.cnn.com/2011/10/12/autos/chevy_spark_electric_car/index.htm`.

Dakhlallah, J., S. Glaser, S. Mammar, and Y. Sebsadji (2008), Tire-road forces estimation using extended kalman filter and sideslip angle evaluation, in *American Control Conference, 2008*, pp. 4597–4602, doi:10.1109/ACC.2008.4587220.

Doumiati, M., A. Victorino, A. Charara, and D. Lechner (2009), Unscented kalman filter for real-time vehicle lateral tire forces and sideslip angle estimation, in *Intelligent Vehicles Symposium, 2009 IEEE*, pp. 901–906, doi:10.1109/IVS.2009.5164399.

Doumiati, M., A. Victorino, A. Charara, and D. Lechner (2010), A method to estimate the lateral tire force and the sideslip angle of a vehicle: Experimental validation, in *American Control Conference (ACC), 2010*, pp. 6936–6942.

Doumiati, M., A. Victorino, A. Charara, and D. Lechner (2011), Onboard real-time estimation of vehicle lateral tire-road forces and sideslip angle, *IEEE/ASME Transactions on Mechatronics*, *16*(4), 601–614, doi:10.1109/TMECH.2010.2048118.

Erdogan, G., L. Alexander, and R. Rajamani (2011), Estimation of tire-road friction coefficient using a novel wireless piezoelectric tire sensor, *IEEE Sensors Journal*, *11*(2), 267–279, doi: 10.1109/JSEN.2010.2053198.

Falcone, P., F. Borrelli, J. Asgari, H. Tseng, and D. Hrovat (2007), Predictive active steering control for autonomous vehicle systems, *IEEE Transactions on Control Systems Technology*, *15*(3), 566–580, doi:10.1109/TCST.2007.894653.

Forkenbrock, G., D. Elsasser, and B. O'Harra (2005), Nhtsafs light vehicle handling and esc effectiveness research program.

Fujimoto, H., and Y. Yamauchi (2010), Advanced motion control of electric vehicle based on lateral force observer with active steering, in *Industrial Electronics (ISIE), 2010 IEEE International Symposium on*, pp. 3627–3632, doi:10.1109/ISIE.2010.5637450.

Fujimoto, H., and B. Yao (2005), Multirate adaptive robust control for discrete-time non-minimum phase systems and application to linear motors, *IEEE/ASME Transactions on Mechatronics*, *10*(4), 371–377, doi:10.1109/TMECH.2005.852398.

Fujimoto, H., A. Tsumasaka, and T. Noguchi (2005), Direct yaw-moment control of electric vehicle based on cornering stiffness estimation, in *Industrial Electronics Society, 2005. IECON 2005. 31st Annual Conference of IEEE*, p. 6 pp., doi:10.1109/IECON.2005.1569321.

Gelb, A. (1974), *Applied optimal estimation*, MIT Press.

Geng, C., L. Mostefai, M. Denai, and Y. Hori (2009), Direct yaw-moment control of an in-wheel-motored electric vehicle based on body slip angle fuzzy observer, *IEEE Transactions on Industrial Electronics*, *56*(5), 1411–1419, doi:10.1109/TIE.2009.2013737.

Gillespie, T. D. (1992), *Fundamentals of Vehicle Dynamics*, vol. 400, 519 pp., Society of Automotive Engineers.

Guvenc, B., and L. Guvenc (2002), Robust two degree-of-freedom add-on controller design for automatic steering, *IEEE Transactions on Control Systems Technology*, *10*(1), 137–148, doi:10.1109/87.974347.

Guvenc, B., L. Guvenc, and S. Karaman (2009), Robust yaw stability controller design and hardware-in-the-loop testing for a road vehicle, *IEEE Transactions on Vehicular Technology*, *58*(2), 555–571, doi:10.1109/TVT.2008.925312.

Hac, A., T. Brown, and J. Martens (2004), Detection of vehicle rollover, *SAE Technical Paper*, *2004*(724).

Hahn, J.-O., R. Rajamani, and L. Alexander (2002), Gps-based real-time identification of tire-road friction coefficient, *IEEE Transactions on Control Systems Technology*, *10*(3), 331–343, doi:10.1109/87.998016.

HONDA (2012), Honda Begins Deliveries of 2013 Fit EV at Honda Worldwide site, `http://world.honda.com/news/2012/4120120Deliveries-2013-Fit-EV/index.html`.

Hori, Y. (2004), Future vehicle driven by electricity and control-research on four-wheel-motored "uot electric march ii", *IEEE Transactions on Industrial Electronics*, *51*(5), 954–962, doi:10.1109/TIE.2004.834944.

Hori, Y., Y. Toyoda, and Y. Tsuruoka (1998), Traction control of electric vehicle: basic experimental results using the test ev ldquo;uot electric march rdquo;, *IEEE Transactions on Industry Applications*, *34*(5), 1131–1138, doi:10.1109/28.720454.

Hsu, Y.-H., S. Laws, and J. Gerdes (2010), Estimation of tire slip angle and friction limits using steering torque, *IEEE Transactions on Control Systems Technology*, *18*(4), 896–907, doi:10.1109/TCST.2009.2031099.

Hu, J.-S., D. Yin, Y. Hori, and F.-R. Hu (2012), Electric vehicle traction control: A new mtte methodology, *IEEE Industry Applications Magazine*, *18*(2), 23–31, doi: 10.1109/MIAS.2011.2175519.

J.I Park, D. K., J.Y Yoon, and K. Yi (2008), Roll state estimator for rollover mitigation control, *Proceedings of the Institution of Mechanical Engineers, Part D: Journal of Automobile Engineering*, pp. 1289–1312, doi:10.1243/09544070JAUTO803.

Jonasson, M., J. Andreasson, S. Solyom, B. Jacobson, and A. S. Trigell (2011), Utilization of Actuators to Improve Vehicle Stability at the Limit: From Hydraulic Brakes Toward Electric Propulsion, *Journal of Dynamic Systems, Measurement, and Control*, *133*(5), 051,003+, doi: 10.1115/1.4003800.

Kawashima, K., Y. Hori, T. Uchida, and S. Oh (2010), Robust bank angle estimation for rolling stability control on electric vehicle, in *Advanced Motion Control, 2010 11th IEEE International Workshop on*, pp. 448–453, doi:10.1109/AMC.2010.5464087.

Kim, B. K., and W. K. Chung (2003), Advanced disturbance observer design for mechanical positioning systems, *IEEE Transactions on Industrial Electronics*, *50*(6), 1207–1216, doi: 10.1109/TIE.2003.819695.

Kim, D., S. Hwang, and H. Kim (2008), Vehicle stability enhancement of four-wheel-drive hybrid electric vehicle using rear motor control, *IEEE Transactions on Vehicular Technology*, *57*(2), 727–735, doi:10.1109/TVT.2007.907016.

Kim, J. (2009), Identification of lateral tyre force dynamics using an extended kalman filter from experimental road test data, *Control Engineering Practice*, *17*(3), 357–367, doi: 10.1016/j.conengprac.2008.08.002.

Koichiro Ono, M. A., Takeshi Takizawa (2009), Preload measuring device for double row rolling bearing unit.

Lee, C., K. Hedrick, and K. Yi (2004), Real-time slip-based estimation of maximum tire-road friction coefficient, *IEEE/ASME Transactions on Mechatronics*, *9*(2), 454–458, doi: 10.1109/TMECH.2004.828622.

Lee, H. S., and M. Tomizuka (1996), Robust motion controller design for high-accuracy positioning systems, *IEEE Transactions on Industrial Electronics*, *43*(1), 48–55, doi: 10.1109/41.481407.

Li, L., F.-Y. Wang, and Q. Zhou (2006), Integrated longitudinal and lateral tire/road friction modeling and monitoring for vehicle motion control, *IEEE Transactions on Intelligent Transportation Systems*, *7*(1), 1–19, doi:10.1109/TITS.2005.858624.

Ljung, L. (1999), *System Identification: Theory for the User*, Prentice Hall Information And System Sciences Series, Prentice Hall PTR.

Mammar, S., and D. Koenig (2002), Vehicle handling improvement by active steering, *Vehicle System Dynamics*, *38*(3), 211–242, doi:10.1076/vesd.38.3.211.8288.

Mokhiamar, O., and M. Abe (2006), How the four wheels should share forces in an optimum cooperative chassis control, *Control Engineering Practice*, *14*(3), 295–304, doi: 10.1016/j.conengprac.2005.03.023, ¡ce:title¿Advances in Automotive Control (AC'04)¡/ce:title¿ ¡xocs:full-name¿Advances in Automotive Control (AC'04)¡/xocs:full-name¿.

Mutoh, N., Y. Hayano, H. Yahagi, and K. Takita (2007), Electric braking control methods for electric vehicles with independently driven front and rear wheels, *IEEE Transactions on Industrial Electronics*, *54*(2), 1168–1176, doi:10.1109/TIE.2007.892731.

Nagai, M., M. Shino, and F. Gao (2002), Study on integrated control of active front steer angle and direct yaw moment, *JSAE Review*, *23*(3), 309–315, doi:10.1016/S0389-4304(02)00189-3.

Nam, K., S. Oh, H. Fujimoto, and Y. Hori (2011), Vehicle state estimation for advanced vehicle motion control using novel lateral tire force sensors, *American Control Conference (ACC), 2011*, *3*, pp.4853 –4858.

Nam, K., H. Fujimoto, and Y. Hori (2012a), Lateral stability control of in-wheel-motor-driven electric vehicles based on sideslip angle estimation using lateral tire force sensors, *Vehicular Technology, IEEE Transactions on*, *61*(5), 1972–1985, doi:10.1109/TVT.2012.2191627.

Nam, K., S. Oh, H. Fujimoto, and Y. Hori (2012b), Estimation of sideslip and roll angles of electric vehicles using lateral tire force sensors through rls and kalman filter approaches, *IEEE Transactions on Industrial Electronics*, *PP*(99), 1, doi:10.1109/TIE.2012.2188874.

NEXTCAR (2011), Who's taking a Mitsubishi i-MiEV, `http://www.nextcar.com.au/n.mitsubishi.imiev.100723.html`.

Nguyen, B. M., K. Nam, H. Fujimoto, and Y. Hori. (2011), Proposal of cornering stiffness estimation without vehicle side slip angle using lateral force sensor, in *Proc. IEEJ Technical Meeting Record*, vol. IIC–11–140.

NHTSA (2012), Federal Motor Vehicle Safety Standards; Electronic Stability Control Systems.

Ogata, K. (2010), *Modern Control Engineering*, Prentice-Hall electrical engineering series. Instrumentation and controls series, Prentice Hall.

Pacejka, H. (2006), *Tire and vehicle dynamics*, SAE-R, SAE International.

Pacejka, H., and R. Sharp (1991), Shear force development by pneumatic tyres in steady state conditions: A review of modelling aspects, *Vehicle System Dynamics*, *20*(3-4), 121–175, doi: 10.1080/00423119108968983.

Pacejka, H. B., and E. Bakker (1992), The magic formula tyre model, *Vehicle System Dynamics*, *21*(sup001), 1–18, doi:10.1080/00423119208969994.

Pacejka, H. B., and I. J. M. Besselink (1997), Magic formula tyre model with transient properties, *Vehicle System Dynamics*, *27*(sup001), 234–249, doi:10.1080/00423119708969658.

Phanomchoeng, G., R. Rajamani, and D. Piyabongkarn (2011), Nonlinear observer for bounded jacobian systems, with applications to automotive slip angle estimation, *IEEE Transactions on Automatic Control*, *56*(5), 1163–1170, doi:10.1109/TAC.2011.2108552.

Pike-research (2010), An overview of electric vehicles on the market and in development, `http://ec.europa.eu/clima/policies/transport/vehicles/docs/d1_en.pdf`.

Piyabongkarn, D., R. Rajamani, J. Grogg, and J. Lew (2009), Development and experimental evaluation of a slip angle estimator for vehicle stability control, *IEEE Transactions on Control Systems Technology*, *17*(1), 78–88, doi:10.1109/TCST.2008.922503.

Rajamani, R. (2011), *Vehicle Dynamics and Control*, Mechanical Engineering Series, Springer.

Rajamani, R., N. Piyabongkarn, J. Lew, K. Yi, and G. Phanomchoeng (2010), Tire-road friction-coefficient estimation, *IEEE Control Systems*, *30*(4), 54–69, doi:10.1109/MCS.2010.937006.

Rajamani, R., G. Phanomchoeng, D. Piyabongkarn, and J. Y. Lew (2011a), Algorithms for real-time estimation of individual wheel tire-road friction coefficients, *IEEE/ASME Transactions on Mechatronics*, *PP*(99), 1–13, doi:10.1109/TMECH.2011.2159240.

Rajamani, R., D. Piyabongkarn, V. Tsourapas, and J. Lew (2011b), Parameter and state estimation in vehicle roll dynamics, *IEEE Transactions on Intelligent Transportation Systems*, *12*(4), 1558–1567, doi:10.1109/TITS.2011.2164246.

Ray, L. (1995), Nonlinear state and tire force estimation for advanced vehicle control, *IEEE Transactions on Control Systems Technology*, *3*(1), 117–124, doi:10.1109/87.370717.

Ryu, J., and J. C. Gerdes (2004), Integrating inertial sensors with gps for vehicle dynamics control, *Journal of Dynamic Systems Measurement and Control*, *126*(June), 1–26.

Sabanovic, A., and K. Ohnishi (2011), *Motion Control Systems*, John Wiley & Sons.

Sado, H., S. Sakai, and Y. Hori (1999), Road condition estimation for traction control in electric vehicle, in *Industrial Electronics, 1999. ISIE '99. Proceedings of the IEEE International Symposium on*, vol. 2, pp. 973–978 vol.2, doi:10.1109/ISIE.1999.798747.

Sakai, S., H. Sado, and Y. Hori (1999), Motion control in an electric vehicle with four independently driven in-wheel motors, *IEEE/ASME Transactions on Mechatronics*, *4*(1), 9–16, doi:10.1109/3516.752079.

Segawa, M., S. Nakano, O. Nishihara, and H. Kumamoto (2001), Vehicle stability control strategy for steer by wire system, *JSAE Review*, *22*(4), 383–388, doi:10.1016/S0389-4304(01)00144-8.

Sierra, C., E. Tseng, A. Jain, and H. Peng (2006), Cornering stiffness estimation based on vehicle lateral dynamics, *Vehicle System Dynamics*, *44*(1), 24–38.

Skogestad, S., and I. Postlethwaite (1996), *Multivariable Feedback Control: Analysis and Design*, John Wiley & Sons.

Slotine, J., and W. Li (1991), *Applied nonlinear control*, Prentice Hall.

Song, J., and W. S. Che (2009), Comparison between braking and steering yaw moment controllers considering abs control aspects, *Mechatronics*, *19*(7), 1126–1133, doi:10.1016/j.mechatronics.2008.11.011, ¡ce:title¿Special Issue on Hardware-in-the-loop simulation¡/ce:title¿.

Suzuki, T., and H. Fujimoto (2010), Slip ratio estimation and regenerative brake control without detection of vehicle velocity and acceleration for electric vehicle at urgent brake-turning, in *Advanced Motion Control, 2010 11th IEEE International Workshop on*, pp. 273–278, doi: 10.1109/AMC.2010.5464122.

Svendenius, J., M. Gafvert, F. Bruzelius, and J. Hulten (2009), Experimental validation of the brush tire model, *Tire Science and Technology*, *37*(2), 122–137.

Tahami, F., R. Kazemi, and S. Farhanghi (2003), A novel driver assist stability system for all-wheel-drive electric vehicles, *IEEE Transactions on Vehicular Technology*, *52*(3), 683–692, doi:10.1109/TVT.2003.811087.

Tseng, H., B. Ashrafi, D. Madau, T. Allen Brown, and D. Recker (1999), The development of vehicle stability control at ford, *IEEE/ASME Transactions on Mechatronics*, *4*(3), 223–234, doi:10.1109/3516.789681.

Umeno, T., and Y. Hori (1991), Robust speed control of dc servomotors using modern two degrees-of-freedom controller design, *IEEE Transactions on Industrial Electronics*, *38*(5), 363–368, doi:10.1109/41.97556.

Villagra, J., B. dAndrea Novel, M. Fliess, and H. Mounier (2011), A diagnosis-based approach for tire?road forces and maximum friction estimation, *Control Engineering Practice*, *19*(2), 174–184, doi:10.1016/j.conengprac.2010.11.005.

Wang, J., Q. Wang, L. Jin, and C. Song (2011), Independent wheel torque control of 4wd electric vehicle for differential drive assisted steering, *Mechatronics*, *21*(1), 63–76, doi: 10.1016/j.mechatronics.2010.08.005.

Wang, R., and J. Wang (2012), Fault-tolerant control for electric ground vehicles with independently-actuated in-wheel motors, *Journal of Dynamic Systems, Measurement, and Control*, *134*(2), 021014, doi:10.1115/1.4005050.

Wenzel, T. A., K. J. Burnham, M. V. Blundell, and R. A. Williams (2006), Dual extended kalman filter for vehicle state and parameter estimation, *Vehicle System Dynamics*, *44*(2), 153–171, doi:10.1080/00423110500385949.

Yi, K., J. Yoon, and D. Kim (2007), Model-based estimation of vehicle roll state for detection of impending vehicle rollover, in *American Control Conference, 2007. ACC '07*, pp. 1624–1629, doi:10.1109/ACC.2007.4282507.

Yih, P., and J. Gerdes (2005), Modification of vehicle handling characteristics via steer-by-wire, *IEEE Transactions on Control Systems Technology*, *13*(6), 965–976, doi: 10.1109/TCST.2005.854320.

Yin, D., S. Oh, and Y. Hori (2009), A novel traction control for ev based on maximum transmissible torque estimation, *IEEE Transactions on Industrial Electronics*, *56*(6), 2086–2094, doi:10.1109/TIE.2009.2016507.

You, S. H., J. O. Hahn, and H. Lee (2009), New adaptive approaches to real-time estimation of vehicle sideslip angle, *Control Engineering Practice*, *17*(12), 1367–1379, doi: 10.1016/j.conengprac.2009.07.002.

Zhao, L.-H., Z.-Y. Liu, and H. Chen (2011), Design of a nonlinear observer for vehicle velocity estimation and experiments, *IEEE Transactions on Control Systems Technology*, *19*(3), 664–672, doi:10.1109/TCST.2010.2043104.

Zhou, H., and Z. Liu (2010), Vehicle yaw stability-control system design based on sliding mode and backstepping control approach, *IEEE Transactions on Vehicular Technology*, *59*(7), 3674–3678, doi:10.1109/TVT.2010.2050790.

PUBLICATIONS

[Journal papers]

1. **Kanghyun Nam**, H. Fujimoto, and Y. Hori, "Lateral Stability Control of In-Wheel-Motor-Driven Electric Vehicles Based on Sideslip Angle Estimation Using Lateral Tire Force Sensors", *IEEE Transaction on Vehicular Technology*, vol.61, no.5, pp.1972–1985, Jun. 2012. (Published)

2. **Kanghyun Nam**, S. Oh, H. Fujimoto, and Y. Hori, "Estimation of Sideslip and Roll Angles of Electric Vehicles Using Lateral Tire Force Sensors Through RLS and Kalman Filter Approaches", *IEEE Transaction on Industrial Electronics*, vol.PP, no.99, pp.1, 0 doi: 10.1109/TIE.2012.2188874, 2012. (In press)

3. **Kanghyun Nam** and S. B. Choi, "Design of Camless-engine Valve Actuation System for Robust Valve Timing Control", *International Journal of Vehicle Systems Modelling and Testing*, 2012. (In press)

4. **Kanghyun Nam**, S. Oh, H. Fujimoto, and Y. Hori, "Robust Yaw Stability Control for Electric Vehicles Based on Active Front Steering Control Through Steer-by-Wire (SbW) System", *International Journal of Automotive Technology*, 2012. (Accepted)

5. **Kanghyun Nam**, H. Fujimoto, and Y. Hori, "Advanced Motion Control of Electric Vehicles Based on Robust Lateral Tire Force Control via Active Front Steering", *IEEE/ASME Transaction on Mechatronics*, 2012. (In revision)

6. **Kanghyun Nam**, H. Fujimoto, and Y. Hori, "Design of Adaptive Sliding Mode Controller for Robust Yaw Stabilization of In-Wheel-Motor-Driven Electric Vehicles", *International Journal of Vehicle Design*, 2012. (Under review)

[Conference papers]

1. **K. Nam** and S. B. Choi, "Dynamic Simulations and Adaptive Valve timing Control for a Cam-less Engine Valve Actuator", *Proc. of Korean Society of Automotive Engineers Annual Conference*, 2008, pp.189-194.

2. **K. Nam** and Y. Hori, "Sliding Mode Controller Design for Optimal Slip Control of Electric Vehicles Based on a Fuzzy Vehicle Velocity Estimation Logic", *FISITA 2010 Student Congress*, 2010.

3. **K. Nam**, S. Oh, and Y. Hori, "Robust Yaw Stability Control for Electric Vehicles Based on Active Steering Control", *Vehicle Power and Propulsion Conference (VPPC), 2010 IEEE*, pp. 1–5, Sept. 2010.

4. **K. Nam**, S. Oh, and Y. Hori, "Robust Yaw Stability Control for Electric Vehicles Based on Steering Angle-Disturbance Observer (SA-DOB) and Tracking Control Design", *IECON 2010 - 36th Annual Conference on IEEE Industrial Electronics Society*, pp. 1943–1948, Nov. 2010.

5. **K. Nam**, Y. Kim, S. Oh, and Y. Hori, "Steering Angle-Disturbance Observer (SA-DOB) Based Yaw Stability Control for Electric Vehicles with In-wheel Motors", *2010 International Conference on Control Automation and Systems (ICCAS)*, pp. 1303–1307, Oct. 2010.

6. **K. Nam**, S. Oh, H. Fujimoto, and Y. Hori, "Direct Roll Moment Control for Electric Vehicles Based on Roll Angle Observer and Lateral Tire Force Control", *2011 IEEE 8th International Conference on Power Electronics and ECCE Asia (ICPE & ECCE)*, pp. 2681–2686, 2011.

7. **K. Nam**, S. Oh, H. Fujimoto, and Y. Hori, "Vehicle State Estimation For Advanced Vehicle Motion Control Using Novel Lateral Tire Force Sensors", *2011 American Control Conference (ACC)* , pp. 4853–4858, 2011.

8. **K. Nam**, H. Fujimoto, and Y. Hori, "Design of Adaptive Sliding Mode Controller for Robust Yaw Stabilization of In-wheel-motor-driven Electric Vehicles", *26th International Electric Vehicle Symposium (EVS26)* , May 2012.

9. **K. Nam**, H. Fujimoto, and Y. Hori, "Motion Control of Electric Vehicles Based on Robust Lateral Tire Force Control Using Lateral Tire Force Sensors", *2011 IEEE/ASME International Conference on Advanced Intelligent Mechatronics (AIM)*, pp.526–531, Jul. 2012.

[Co-authored papers]

1. B. M. Nguyen, **K. Nam**, H. Fujimoto, Y. Hori, and C. M. Ta, "Modeling of Lateral Dynamics for Motion Control of Electric Vehicle", *Proceeding of 5th Symposium of South East Asian Technical University Consortium*, ISSN No. 1882-5796, Feb. 2011.

2. Y. Wang, **K. Nam**, H. Fujimoto, and Y. Hori, "Robust Roll and Yaw Integrated Control Using 4 wheel Steering Based on Yaw Moment and Lateral Force Observers", *IIC–11-138*, 2011.

3. B. M. Nguyen, **K. Nam**, H. Fujimoto, and Y. Hori, "Proposal of Cornering Stiffness Estimation without Vehicle Side Slip Angle Using Lateral Force Sensor", *IIC–11–140*, 2011.

4. K. Kim, **K. Nam**, S. Oh, H. Fujimoto, and Y. Hori, "Human Friendly Yaw Motion Control for Power Assist Wheelchair", *IEEJ Conference*, Vol. 2, pp. 603–606 2011.

5. K. Kim, **K. Nam**, S. Oh, H. Fujimoto, and Y. Hori, "Human Friendly Yaw Motion Control for Power-assisted Wheelchair", *IECON 2011 - 37th Annual Conference on IEEE Industrial Electronics Society*, pp. 4256–4261, Nov. 2011.

6. Y. Wang, **K. Nam**, H. Fujimoto, and Y. Hori, "Proposal of Multi-rate Controller for Vehicle Body Slip Angle Based on Real-time Lane Detection", *AVEC'12 Symposium*, Sep. 2012. (Accepted)

7. A. Viehweider, **K. Nam**, H. Fujimoto, and Y. Hori, "A Fault Detection and Isolation Scheme for Lateral Vehicle Dynamics of EVs using a Quantitative Parity Space Approach", *IEEE IECON 2012*, Oct. 2012. (Accepted)

8. K. Kim, **K. Nam**, S. Oh, H. Fujimoto, and Y. Hori, "Two-dimensional Assist Control of Power-assisted Wheelchair considering Straight and Rotation Motion Decomposition", *IEEE IECON 2012*, Oct. 2012. (Accepted)

[**Proceedings**]

1. **K. Nam**, S. Oh, and Y. Hori, "Robust Yaw Stability Control for Electric Vehicles Based on Active Steering Control", *Proc. of SNU-UT Joint Seminar*, Mar. 2010, pp.310-315.

2. Y. Kim, **K. Nam**, H. Fujimoto, and Y. Hori, "A Novel Chassis Structure for Advanced EV Motion Control Using Caster Wheels with Disturbance Observer and Independent Driving Motors", *Proc. of SNU-UT Joint Seminar*, Dec. 2011.